

Casimir effect in the plane-sphere geometry: Beyond the proximity force approximation

Dissertation

zur Erlangung des akademischen Grades

Dr. rer. nat.

eingereicht an der

Mathematisch-Naturwissenschaftlich-Technischen Fakultät

der Universität Augsburg

von

Michael Hartmann

Augsburg, 23. Juli 2018



Universität Augsburg
Institut für Physik

Erstgutachter:	Prof. Dr. Gert-Ludwig Ingold
Zweitgutachter:	Prof. Dr. Thilo Kopp
Drittgutachter:	Prof. Ricardo Decca, Ph.D.
Tag der mündlichen Prüfung:	11. Oktober 2018

Contents

1	Introduction	1
2	The Casimir effect for two parallel planes	7
2.1	Electromagnetic fields in vacuum	8
2.2	The plane-wave basis	13
2.3	The translation operator	15
2.4	Scattering at a plane	16
2.5	The plasma and Drude model	17
2.6	The dielectric function from optical data	19
2.7	The plane-plane geometry	22
2.8	The scattering formula	30
3	The proximity force approximation	33
3.1	Heuristic derivation of the proximity force approximation	35
3.2	Casimir free energy in the plane-wave basis	37
3.3	Scattering at a sphere	38
3.4	The WKB approximation	39
3.5	Saddle-point approximation	40
3.6	Casimir free energy and force	43
4	Symmetrized round-trip operator in the plane-sphere geometry	45
4.1	Scattering at a sphere	45
4.2	The round-trip operator	46
4.3	Matrix elements of the round-trip operator	49
4.4	Low-frequency limit	52
4.5	Properties of the round-trip matrices	55
4.6	Hierarchical matrices	58
5	Numerical issues	63
5.1	Dilogarithm	63
5.2	Modified Bessel functions	64
5.3	Legendre polynomials	66
5.4	Associated Legendre polynomials	68
5.5	Truncation of the vector space	70

5.6	Integration over k	72
5.7	Computation of the determinant	78
5.8	Differentiation	79
5.9	Numerical tests	80
6	Corrections beyond the proximity force approximation at $T = 0$	83
6.1	Perfect reflectors	83
6.2	Plasma model	87
6.3	Drude model	88
7	Comparison with experiments	91
7.1	Drude and plasma prescription	92
7.2	Corrections beyond the proximity force approximation	93
7.3	Comparison with experimental data	96
8	Conclusion and outlook	101
A	Special functions	103
A.1	Spherical harmonics	103
A.2	Associated Legendre polynomials	103
B	Proofs and derivations	107
B.1	Signs of Mie coefficients	107
B.2	Inequality for associated Legendre polynomials of the Turán type	109
B.3	Determinant of block matrices	110
B.4	Derivatives of addition theorems for spherical harmonics	110
C	Matrix elements of \mathcal{R}_S in the plane-wave basis	113
D	Change of basis matrix elements	117
	Bibliography	119
	List of symbols	133
	List of publications	135
	Acknowledgements	137

Chapter 1

Introduction

Vacuum fluctuations are a remarkable prediction of quantum electrodynamics. Ultimately as a consequence of the uncertainty principle, the electromagnetic field in vacuum undergoes fluctuations around zero. These quantum fluctuations can give rise to forces between macroscopic objects, as was first realized by Hendrik Casimir in 1948 [1]. Casimir considered two perfectly reflecting plates of area A separated by a distance L at zero temperature and found an attractive force

$$\frac{F}{A} = -\frac{\hbar c \pi^2}{240 L^4}. \quad (1.1)$$

The radiation pressure inside the plates pushes the plates apart, while the radiation pressure outside of the plates pushes them together. The net effect is the Casimir force (1.1). The force is universal in the sense that it only depends on the speed of light c and the reduced Planck constant \hbar , indicating that the Casimir force is a quantum effect mediated by the electromagnetic field.

The Casimir effect is closely related to the van der Waals forces [2]. The attractive van der Waals forces can be divided into three different types: The electrostatic force between two molecules with permanent multipole moments, the Debye force between a molecule with permanent multipole moment and a molecule with induced multipole moment, and the London dispersion forces between two non-polar molecules. The quantum theory of dispersion forces was developed by London in 1930 [3]. London derived an attractive force that decreases as $1/L^6$ with the separation L between the molecules. Studying the stability of colloids, Verwey and Overbeek observed that, at large separations, the London dispersion force decreases more rapidly than predicted [4]. Casimir and Polder resolved the discrepancy in 1948. Taking the influence of retardation on the interaction into account, they showed that the power law of the force changes from $1/L^6$ at small separations to $1/L^7$ at large separations [5]. As a preliminary step, they also considered the interaction between a perfectly conducting plate and an atom. Following a suggestion by Bohr [6], Casimir found a simple derivation for this setup in terms of zero-point energy. Applying the same method to two perfectly conducting plates, he obtained his famous formula.

The Casimir force is the dominant force between neutral non-magnetic materials in the nanometre to micrometre range. For this reason, a precise knowledge of the Casimir force is crucial in order to detect possible deviations from the gravitational interaction at sub-micrometre distances [7–11], and thus to either exclude or to possibly support proposed mechanisms for a fifth fundamental interaction [12, 13]. Moreover, the Casimir effect is an observable consequence of vacuum fluctuations in the macroscopic world. As such, it is linked to the problem of zero-point energy and the cosmological constant problem. While the observation of type Ia supernovae indicates that the energy density of vacuum is non-zero [14, 15], the measured and the theoretically estimated values differ by more than 50 orders of magnitude [16]. From a technological point of view, the Casimir effect has been shown to play an important role for micro- and nano-electromechanical systems (MEMS, NEMS) [17, 18]. In these systems, Casimir forces are a source of stiction, causing movable elements to stick to nearby surfaces [19].

While the Casimir effect has been observed in a number of historic experiments [20], accurate measurements started only in the late 1990s with the experiments of Lamoreaux [21] and Mohideen [22]. Instead of the plane-plane geometry considered by Casimir, most modern experiments employ the geometry of a plane and a sphere in order to avoid the problem of misalignment. The sphere-plane geometry, shown in Fig. 1.1, consists of a sphere of radius R separated by a distance L from a plane. Experimentally, a measurable force signal requires the radius R of the sphere to be much larger than the separation L . Hence, the aspect ratio R/L used in common experiments is rather large and typically in the range of 10^2 to 10^3 . In contrast, the aspect ratio shown in Fig. 1.1 is only $R/L = 4/3$, more than two orders of magnitude smaller than in experiments. One can get an intuitive picture imagining the sphere to be the earth. Then, the separation used in experiments corresponds to the typical cruising altitude of a commercial jet.

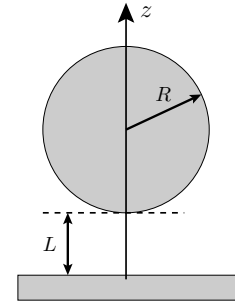


Figure 1.1: Sphere of radius R and plate separated by a distance L .

The plane-sphere geometry is in principle amenable to an exact description in terms of a multipole expansion [23–25]. The number of multipole moments required in a numerical calculation of the Casimir force increases linearly with the aspect ratio. Since typically the numerical effort grows with the third power of the number of the multipole moments, the numerical evaluation of the Casimir force has been limited to aspect ratios $R/L \lesssim 100$ [26]. For this reason, the analysis of all plane-sphere experiments to this date has relied exclusively on the heuristic proximity force approximation (PFA) [27]. The PFA assumes that the Casimir force between a sphere and a plane can be decomposed into contributions from many small plane-plane segments which are summed up. As the Casimir force is non-additive [28], this approach can only be approximate. In fact, the corrections to the

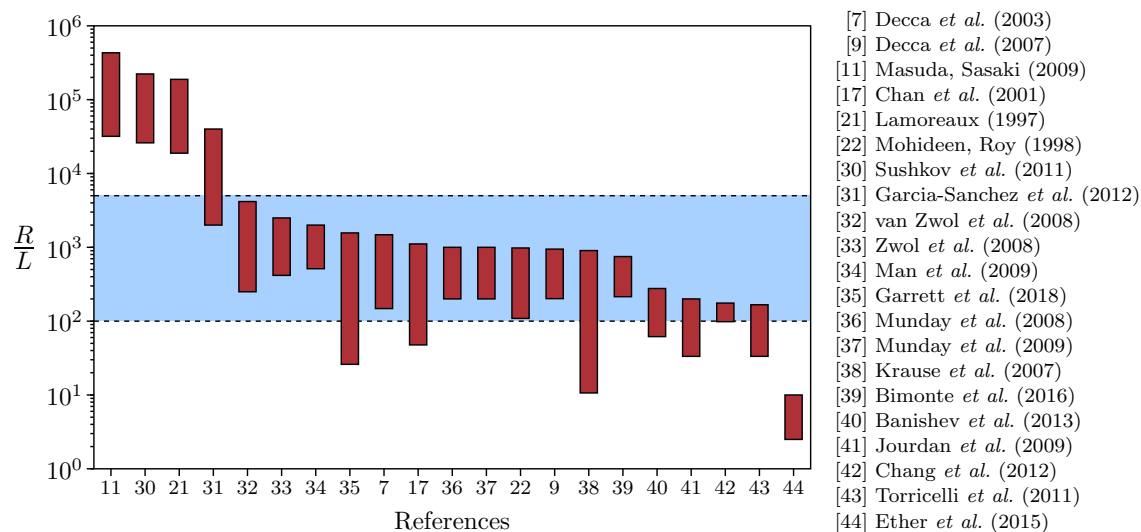


Figure 1.2: The aspect ratio R/L is shown for Casimir experiments involving a sphere or a spherical lens and a plane or another sphere. The range of aspect ratios, which became accessible through the numerical approach discussed in this thesis, is marked in light blue. (Adapted from Ref. [29])

PFA under real experimental conditions have not been known until now.

Fig. 1.2 depicts the aspect ratios R/L for recent experiments [7, 9, 11, 17, 21, 22, 30–44] measuring the Casimir force or the force gradient between a sphere and a plate. For the large aspect ratios used in the experiments of Refs. [11, 21, 30], the Casimir interaction has been measured between a plate and a sphere segment. In two of the experiments, measurements were not performed in the plane-sphere geometry but using two spheres [35, 44]. The smallest aspect ratio is reached by an experiment proposing extremely sensitive measurements of the Casimir force between two spheres by means of optical tweezers [44].

Until very recently, exact computations of the Casimir force have been limited to aspect ratios $R/L \lesssim 100$, thus most experiments have been out of reach of exact theoretical calculations. In order to cover the vast majority of experiments, it is necessary to numerically treat aspect ratios up to $R/L \lesssim 5000$. The area of light blue color in Fig. 1.2 marks the range of aspect ratios that became accessible through the numerical advances discussed in this thesis. The very large aspect ratios not yet covered are rather well described by the proximity force approximation up to corrections typically smaller than one percent.

Precise experiments have reached a level of accuracy that renders the measurements sensitive to the material properties of the sphere and the plate [45]. This has led to the so-called Drude-plasma controversy. While the materials used in experiments clearly have a finite dc conductivity, which can be accounted for within the Drude model, the plasma model with its infinite dc conductivity is in better agreement with most Casimir measurements [9, 10, 39, 40, 42]. Fig. 1.3 shows the Casimir pressure measured in Ref. [9] together with theoretical predictions using the Drude and the plasma model. The sub-figures show

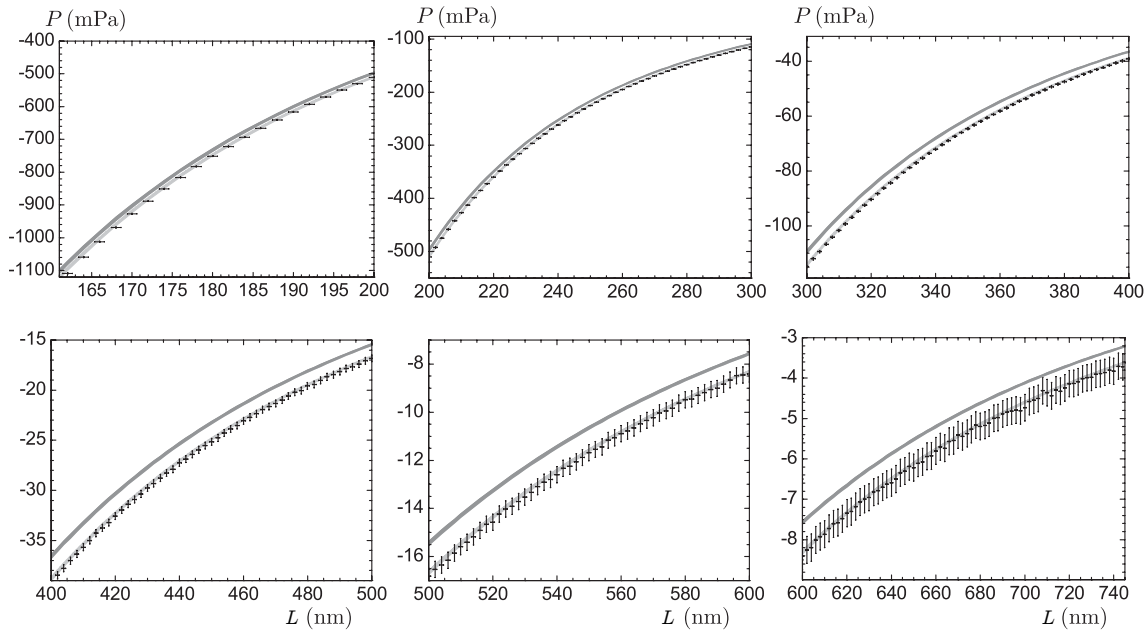


Figure 1.3: Experimental data for the Casimir pressure P as a function of the separation L are shown including error bars. The lines represent theoretical predictions within the proximity force approximation. The theoretical results based on the plasma model (lower, light-grey line) are within experimental error bounds, while the results based on the Drude model (upper, dark-grey line) clearly deviate from the experimental data. The figure has been taken from Ref. [9].

the experimental data for different ranges of separation. The Casimir pressure has been measured for a gold-coated plate and a gold-coated sphere with radius $R = 151.3 \mu\text{m}$. Clearly, the line corresponding to the Drude model shows a significant deviation from the experimental data. In fact, based on the experimental data shown in the figure, the Drude approach has been excluded at a 99.9% confidence level for separations between 210 and 620 nm [9]. A few experiments found agreement with the Drude model [30, 31], but the results have also been questioned [46, 47]. The controversy also led to a number of theoretical results. However, there is still no agreement yet, why experiments are in better agreement with the lossless plasma model.

In this thesis, we study the Casimir effect in the experimentally important geometry of a plane and a sphere. We focus on the proximity force approximation and corrections to it. We prove that the PFA provides the correct leading order term when the aspect ratio R/L becomes large, and establish a connection between the specular-reflection limit of Mie scattering and the PFA. Our derivation holds for arbitrary materials and temperatures, in contrast to earlier works that are limited to zero temperature [48–50] or high temperatures [51, 52], or only hold under the assumption that the far side of the sphere does not contribute [53].

Moreover, we extend the range of numerically accessible aspect ratios to values used in typical experiments. We compute the Casimir interaction using the scattering approach

taking the curvature of the sphere fully into account. In the scattering approach, the Casimir free energy is given as a sum over determinants of the round-trip operator. The standard definition of the round-trip operator results in ill-conditioned matrices with matrix elements differing by hundreds of orders of magnitude, rendering a numerical evaluation extremely difficult. We show that this problem can be eliminated by a symmetrization of the round-trip operator. In addition, the symmetrization allows one to evaluate the determinants using a state-of-the-art algorithm suited for hierarchical matrices. This improves the computational complexity and significantly reduces the computational time, thus enabling us to perform computations for aspect ratios up to $R/L \sim 5000$, an improvement of almost two orders of magnitude compared to the largest aspect ratios treated so far [26].

The numerical improvements allow us to assess the quality of the proximity force approximation and compute the corresponding corrections for aspect ratios used in typical experiments. At zero temperature, we confirm the leading-order correction to the PFA and numerically obtain the next-to-leading-order correction. It turns out that in contrast to what is commonly believed in the literature, the next-to-leading-order correction is proportional to $(L/R)^{3/2}$. Furthermore, we compare our numerical results with the PFA for gold at room temperature. We find that the experimental bound for corrections to the PFA obtained in Ref. [38] is violated for both the plasma and the Drude model. While our corrections to the PFA for the plasma model lie well outside the experimental bound, the corresponding corrections based on the Drude model are significantly smaller but still in violation of the experimental bound for small separations. Moreover, a direct comparison with experimental data from Ref. [38] reveals a discrepancy between the experimental results and our numerical data. Surprisingly, the experimental data agree well with the results obtained within the proximity force approximation, but deviate from the corresponding data obtained using the scattering formula.

The outline of the thesis is as follows: In chapter 2, we study the Casimir effect in the plane-plane geometry originally considered by Casimir. This allows us to introduce various theoretical concepts needed throughout the thesis. In particular, we introduce the scattering approach that allows an exact computation of the Casimir interaction in the plane-sphere geometry. In chapter 3, we present the derivation of the proximity force approximation in the limit of small separations. In chapter 4, we derive the matrix elements of the symmetrized round-trip operator and discuss the efficient evaluation of the determinants of the round-trip matrices using an algorithm suited for hierarchical matrices. After discussing technical details of the numerical implementation in chapter 5, we compare our numerical results with the PFA for zero temperature in chapter 6, and for parameters corresponding to typical experiments in chapter 7. Our results are summarized in chapter 8. Properties and definitions of the spherical harmonics and the associated Legendre polynomials, as well as some technical calculations can be found in the appendix.

Chapter 2

The Casimir effect for two parallel planes

Although Casimir originally considered the geometry of two parallel planes [1], most experiments measure the Casimir interaction between a sphere and a plate in order to avoid misalignments. This geometry is in principle amenable to an exact description by the scattering approach [23–25]. However, the numerical evaluation for parameters corresponding to typical experiments is challenging and became feasible only very recently [29, 54]. Experiments are usually analyzed using the proximity force approximation (PFA) [27]. The PFA assumes that the Casimir force can be decomposed into contributions from many small plane-plane segments that can be integrated over, thereby linking the plane-plane geometry to arbitrary geometries.

Since the PFA relies on the Casimir interaction in the plane-plane geometry, we study the Casimir effect in this geometry in this chapter. This also allows us to introduce various concepts necessary for the treatment of the Casimir effect in the plane-sphere geometry. We show that the Maxwell equations in vacuum are equivalent to a vector Helmholtz equation and derive the full solution of the electromagnetic field. After quantization of the electromagnetic field, it is found that the vacuum exerts a radiation pressure on objects placed inside the vacuum. We introduce the plane-wave basis which will play an important role in the following chapters, derive the translation operator in the plane-wave basis, and give the reflection coefficients for the scattering at a plane. The reflection coefficients depend on the dielectric properties of the plane. We present perfect reflectors, the plasma and the Drude model as simple theoretical models for the dielectric function of metals. Also, we describe how the dielectric function at imaginary frequencies can be computed from tabulated optical data. This is important because after a Wick rotation the dielectric function is evaluated at imaginary frequencies. Then, we derive the Casimir force and energy between two parallel mirrors by comparing the radiation pressure between the mirrors with the radiation pressure outside of the mirrors. As an illustration, we study perfect reflectors and metals described by the plasma and the Drude model at finite and

zero temperature. We conclude the chapter by introducing the scattering formula that generalizes the results of the plane-plane geometry to arbitrary geometries.

2.1 Electromagnetic fields in vacuum

In vacuum, without charges and currents, the Maxwell equations are given by [55]

$$\nabla \cdot \mathbf{E}(\mathbf{R}, t) = 0, \quad (2.1a)$$

$$\nabla \cdot \mathbf{B}(\mathbf{R}, t) = 0, \quad (2.1b)$$

$$\nabla \times \mathbf{E}(\mathbf{R}, t) = -\frac{\partial \mathbf{B}(\mathbf{R}, t)}{\partial t}, \quad (2.1c)$$

$$\nabla \times \mathbf{B}(\mathbf{R}, t) = \frac{1}{c^2} \frac{\partial \mathbf{E}(\mathbf{R}, t)}{\partial t}. \quad (2.1d)$$

Here, $\mathbf{R} = (x, y, z)$ denotes the position and t the time, \mathbf{E} and \mathbf{B} stand for the electric and the magnetic fields, respectively, and c is the speed of light in vacuum. Since the vacuum is free of charges, the electric and magnetic fields are source-free. The third Maxwell equation relates a temporal change of the magnetic field to an eddy electric field, and vice versa for the fourth Maxwell equation.

Throughout this thesis, we use bold upper case letters to denote three dimensional vectors, and bold lower case letters to denote two dimensional vectors in the x - y plane, e.g., $\mathbf{R} = (x, y, z)$ and $\mathbf{r} = (x, y, 0)$.

2.1.1 Potentials and gauge invariance

The electric and the magnetic field in total consist of six vector components. However, not all components are independent, and it is convenient to rewrite the Maxwell equations as second order differential equations expressing the electric and the magnetic fields in terms of a scalar and a vector potential.

Since the magnetic field \mathbf{B} is source-free, it can be expressed in terms of the magnetic vector potential \mathbf{A}

$$\mathbf{B}(\mathbf{R}, t) = \nabla \times \mathbf{A}(\mathbf{R}, t). \quad (2.2)$$

The electric field \mathbf{E} can be expressed in terms of the electric potential $\Phi(\mathbf{R}, t)$ and the vector potential $\mathbf{A}(\mathbf{R}, t)$

$$\mathbf{E}(\mathbf{R}, t) = -\nabla\Phi(\mathbf{R}, t) - \frac{\partial \mathbf{A}(\mathbf{R}, t)}{\partial t}. \quad (2.3)$$

By construction, the fields defined in terms of the vector potential \mathbf{A} and the electric potential Φ satisfy Gauss's law of magnetism (2.1b) and the Maxwell-Faraday equation

(2.1c). The dynamics of the potentials is then determined by substituting (2.3) into Gauss's law (2.1a)

$$\Delta\Phi(\mathbf{R}, t) = -\frac{\partial}{\partial t}\nabla\cdot\mathbf{A}(\mathbf{R}, t), \quad (2.4)$$

and (2.3), (2.2) into Ampère's law (2.1d)

$$\left(\Delta - \frac{1}{c^2}\frac{\partial^2}{\partial t^2}\right)\mathbf{A}(\mathbf{R}, t) = \nabla\left(\nabla\cdot\mathbf{A}(\mathbf{R}, t) + \frac{1}{c^2}\frac{\partial\Phi(\mathbf{R}, t)}{\partial t}\right). \quad (2.5)$$

The second-order partial differential equations (2.4) and (2.5) completely determine the dynamics of the potentials. Together with the definition of the potentials \mathbf{A} (2.2) and Φ (2.3), these equations are equivalent to the Maxwell equations (2.1a)–(2.1d).

The potentials \mathbf{A} and Φ are invariant under the gauge transformation [55, 56]

$$\mathbf{A}(\mathbf{R}, t) \rightarrow \mathbf{A}'(\mathbf{R}, t) = \mathbf{A}(\mathbf{R}, t) + \nabla\Lambda(\mathbf{R}, t), \quad (2.6a)$$

$$\Phi(\mathbf{R}, t) \rightarrow \Phi'(\mathbf{R}, t) = \Phi(\mathbf{R}, t) - \frac{\partial}{\partial t}\Lambda(\mathbf{R}, t), \quad (2.6b)$$

where Λ is an arbitrary function. In particular, it is always possible to find a function Λ such that the vector potential fulfills the Coulomb gauge condition

$$\nabla\cdot\mathbf{A}(\mathbf{R}, t) = 0. \quad (2.7)$$

In the Coulomb gauge, the equation for the electric potential becomes the Laplace equation

$$\Delta\Phi(\mathbf{R}, t) = 0. \quad (2.8)$$

The solution is given by $\Phi = 0$ assuming that the potential vanishes at infinity. The equation for the vector potential (2.5) hence reduces to the wave equation

$$\left(\Delta - \frac{1}{c^2}\frac{\partial^2}{\partial t^2}\right)\mathbf{A}(\mathbf{R}, t) = 0. \quad (2.9)$$

2.1.2 Fourier expansion of the vector potential

The wave equation is linear and solutions can be constructed by a superposition of exponentials

$$\mathbf{A}(\mathbf{R}, t) = \int_{-\infty}^{\infty} d\omega \mathbf{A}(\mathbf{R}, \omega)e^{-i\omega t}. \quad (2.10)$$

We use the same symbol \mathbf{A} to denote the vector potential in the time and frequency domain distinguishing the different spaces by the arguments of \mathbf{A} . Inserting this representation into the wave equation (2.9), we find that in the frequency domain the vector

potential satisfies the vector Helmholtz equation

$$\left(\Delta + \frac{\omega^2}{c^2}\right) \mathbf{A}(\mathbf{R}, \omega) = 0. \quad (2.11)$$

In Cartesian coordinates the vector Helmholtz equation reduces to a scalar Helmholtz equation in every component. The full solution is given by

$$\mathbf{A}(\mathbf{R}, \omega) = \int \frac{d^3\mathbf{K}}{(2\pi)^3} \mathbf{A}(\mathbf{K}, \omega) \delta(\omega^2 - c^2 K^2) e^{i\mathbf{K}\cdot\mathbf{R}}, \quad (2.12)$$

where \mathbf{K} denotes the wave vector and $K = |\mathbf{K}|$. The delta function has been introduced in order to fulfill the dispersion relation $\omega = cK$. Due to the choice of the Coulomb gauge, the divergence of the vector potential vanishes in real space implying that in reciprocal space the vector potential is perpendicular to the wave vector \mathbf{K}

$$\nabla \cdot \mathbf{A}(\mathbf{R}, \omega) = 0 \quad \Leftrightarrow \quad \mathbf{A}(\mathbf{K}, \omega) \cdot \mathbf{K} = 0. \quad (2.13)$$

Thus the vector potential $\mathbf{A}(\mathbf{K}, \omega)$ can be spanned by two orthonormal polarization vectors $\hat{\epsilon}_p$ that are perpendicular to \mathbf{K} .

The full solution in real space and in the time domain can be expanded as a sum over polarization, an integration over frequency, and an integration over all wave vectors

$$\mathbf{A}(\mathbf{R}, t) = \sum_p \int_{-\infty}^{\infty} d\omega \int \frac{d^3\mathbf{K}}{(2\pi)^3} \sqrt{\frac{2\hbar c K}{\epsilon_0}} \hat{\epsilon}_p a_p(\mathbf{K}, \omega) \delta(\omega^2 - c^2 K^2) e^{i(\mathbf{K}\cdot\mathbf{R} - \omega t)}, \quad (2.14)$$

where ϵ_0 denotes the vacuum permittivity and \hbar is the reduced Planck constant. Here, $a_p(\mathbf{K}, \omega)$ corresponds to an expansion coefficient and the square root has been introduced so that after quantization the expansion coefficients obey simple commutation rules. The integration over ω yields two contributions for $\omega = \pm cK$. From now on, we denote by ω the positive frequency satisfying the dispersion relation $\omega \equiv cK$. After integration over the frequency, the solution becomes

$$\mathbf{A}(\mathbf{R}, t) = \sum_m \sqrt{\frac{\hbar}{2\omega\epsilon_0}} \hat{\epsilon}_p \left(a_m e^{-i(\omega t - \mathbf{K}\cdot\mathbf{R})} + a_m^* e^{i(\omega t - \mathbf{K}\cdot\mathbf{R})} \right) \quad (2.15)$$

where $a_m \equiv a_p(\mathbf{K}, \omega)$ and

$$\sum_m \equiv \sum_p \int \frac{d^3\mathbf{K}}{(2\pi)^3} \quad (2.16)$$

denotes the summation over all field modes. The vector potential has been chosen real to ensure that the electric and magnetic fields are real. From the definitions of the potentials

(2.4) and (2.5) the electric and magnetic fields are found to read

$$\mathbf{E}(\mathbf{R}, t) = i \sum_m \sqrt{\frac{\hbar\omega}{2\epsilon_0}} \hat{\epsilon}_p \left(a_m e^{-i(\omega t - \mathbf{K} \cdot \mathbf{R})} - a_m^* e^{i(\omega t - \mathbf{K} \cdot \mathbf{R})} \right), \quad (2.17a)$$

$$\mathbf{B}(\mathbf{R}, t) = i \sum_m \sqrt{\frac{\hbar}{2\omega\epsilon_0}} (\mathbf{K} \times \hat{\epsilon}_p) \left(a_m e^{-i(\omega t - \mathbf{K} \cdot \mathbf{R})} - a_m^* e^{i(\omega t - \mathbf{K} \cdot \mathbf{R})} \right). \quad (2.17b)$$

We have expanded the vector potential (2.15), the electric field (2.17a), and the magnetic field (2.17b) in a Fourier series. Each mode is characterized by the wave vector \mathbf{K} and the polarization p , and arbitrary solutions can be constructed by a superposition of field modes. The electromagnetic field in vacuum has two independent degrees of freedom per mode [56], and the electric field \mathbf{E} , the magnetic field \mathbf{B} , and the wave vector \mathbf{K} are mutually orthogonal.

2.1.3 Zero-point fluctuations

In quantum field theory, the expansion coefficients a_m^* and a_m become creation and annihilation operators obeying, at zero temperature, the canonical commutation relations [56]

$$[a_{m'}, a_m^\dagger] = (2\pi)^3 \delta(\mathbf{K} - \mathbf{K}') \delta_{pp'}, \quad (2.18a)$$

$$[a_{m'}, a_m] = [a_{m'}^\dagger, a_m^\dagger] = 0. \quad (2.18b)$$

After promoting the Fourier coefficients to operators, the electromagnetic field is described as a set of infinite harmonic oscillators, one for each field mode. The vacuum state is the ground state $|0\rangle$ of the electromagnetic field with no photons. While the expectation values of the electric and magnetic fields in vacuum vanish

$$\langle 0 | \mathbf{E} | 0 \rangle = \langle 0 | \mathbf{B} | 0 \rangle = 0, \quad (2.19)$$

the fields undergo quantum fluctuations

$$\langle 0 | E^2 | 0 \rangle = \langle 0 | c^2 B^2 | 0 \rangle = \sum_m \frac{\hbar\omega}{2\epsilon_0}. \quad (2.20)$$

As a consequence, in contrast to classical electrodynamics, the energy density in vacuum does not vanish, but it diverges

$$\langle T_{00} \rangle_{\text{vac}} = \frac{\epsilon_0}{2} \langle 0 | E^2 + c^2 B^2 | 0 \rangle = \sum_m \frac{\hbar\omega}{2}. \quad (2.21)$$

The radiation pressure on plane mirrors perpendicular to the z -axis is given by the component T_{zz} of the electromagnetic stress-energy tensor

$$\langle T_{zz} \rangle_{\text{vac}} = \frac{\epsilon_0}{2} \langle 0 | E^2 + c^2 B^2 - 2E_z^2 - 2c^2 B_z^2 | 0 \rangle = \sum_m \frac{\hbar\omega}{2} \cos^2 \theta, \quad (2.22)$$

where θ denotes the angle of incidence. This expression almost coincides with the energy density (2.21). The factor $\cos^2 \theta$ well-known in studies of radiation pressure arises, because the normal component of the linear momentum imparted to the plate is proportional to $\cos \theta$, and the element of area is increased by $1/\cos \theta$ [57].

Historically, probably the first to come across zero-point energy was Max Planck in 1911 [58–61]. While working on the problem of black body radiation, he found the formula

$$E = \frac{\hbar\omega}{e^{\hbar\omega/k_B T} - 1} + \frac{\hbar\omega}{2} \quad (2.23)$$

for the average energy of an harmonic oscillator in thermal equilibrium at temperature T . Here, k_B denotes the Boltzmann constant. As pointed out by Einstein and Stern in 1913 [62], the zero-point energy exactly cancels a temperature-independent correction to the equipartition theorem in the classical limit $k_B T \gg \hbar\omega$

$$E = k_B T + \frac{\hbar^2 \omega^2}{12 k_B T} + \mathcal{O}\left(\frac{1}{T^3}\right). \quad (2.24)$$

In this way, the zero-point energy renders the high-temperature limit as classical as possible [60]. In their work [62], Einstein and Stern concluded that the existence of zero-point energy is probable. However, in the very same year, Einstein changed his mind writing in a letter to Ehrenfest that zero-point energy is “dead as a doornail” [59].

While Planck’s theory solved the problem of the ultraviolet catastrophe of the Rayleigh-Jeans law and was in perfect agreement with experiments on black body radiation, his formula (2.23) and the advent of quantum mechanics and quantum electrodynamics introduced the problem of a divergent zero-point energy. Commonly, divergent terms in quantum field theories are removed using techniques of renormalization. The success of these techniques led some physicists to doubt the reality of zero-point energy, most famously summed up by Wolfgang Pauli’s Nobel lecture [63]:

“It is clear that this zero-point energy has no physical reality, for instance it is not the source of a gravitational field.”

Already at that time, however, experiments on the behavior of helium at very low temperatures [64, 65] and molecular vibrations [66] supported zero-point energy. Moreover, the experimental discovery of the Lamb shift in 1947 [67] and the Casimir effect theoretically predicted in 1948 [1] are typically regarded as evidence of the reality of zero-point

energy. The interpretation of the Casimir effect caused by zero-point energy is, however, not undisputed [68].

Pauli's argument that zero-point energy should cause gravitational effects is indisputable. While the observation of type Ia supernovae indicates that the energy density of vacuum is non-zero [14, 15], the measured and the theoretically estimated value differ by many orders of magnitude. The energy density e due to zero-point energy is given by

$$e = \sum_m^{\omega_{\max}} \frac{\hbar\omega}{2} = \frac{(\hbar\omega_{\max})^4}{8\pi^2(\hbar c)^3} \quad (2.25)$$

where ω_{\max} is a cutoff frequency. If the cutoff is chosen at the Planck energy, the estimated value of the vacuum energy differs from the measured value by about 121 orders of magnitude. While a more elaborate estimate finds only a mismatch of about 54 orders of magnitude [16], the discrepancy between theory and experiment is still tremendous. Setting the cutoff to match the experimentally measured energy density suggests that gravity might be modified for distances smaller than $85 \mu\text{m}$ [69]. As the Casimir effect is the dominant force between neutral bodies at micron and sub-micron distances, it plays an important role in the search for modifications of the gravitational law at small separations [7–11, 13].

2.2 The plane-wave basis

The scattering formula that will be introduced at the end of this chapter, expresses the Casimir interaction energy between two arbitrary objects in terms of scattering operators. In this section, we introduce the plane-wave basis which is a suitable basis to express these operators. In particular, we derive the proximity force approximation using the scattering formula evaluated in the plane-wave basis in chapter 3. Moreover, we employ the plane-wave basis as an intermediate basis in chapter 4 to derive the matrix elements of the round-trip operator in the multipole basis for the plane-sphere geometry.

In subsection 2.1.2, we found that the electric field allows an expansion by means of the wave vector \mathbf{K} and the polarization p

$$\mathbf{E}(\mathbf{R}, t) = \sum_p \int \frac{d^3\mathbf{K}}{(2\pi)^3} \hat{\mathbf{e}}_p \left(\alpha_p(\mathbf{K}) e^{-i(\omega t - \mathbf{K} \cdot \mathbf{R})} + \alpha_p^*(\mathbf{K}) e^{i(\omega t - \mathbf{K} \cdot \mathbf{R})} \right) \quad (2.26)$$

where we set $\alpha_p(\mathbf{K}) \equiv i(\hbar\omega/2\epsilon_0)^{1/2} a_m$ for convenience. We will study the Casimir effect in the geometry of two parallel planes and the geometry of a sphere above a plane. Both geometries involve a reflection at a plane that is parallel to the x - y plane. The reflection at the plane is preferably described by plane waves with transverse electric (TE) and transverse magnetic (TM) polarization. Transverse electric modes have no electric field in

z -direction, transverse magnetic modes have no magnetic field in z -direction. Denoting unit vectors by a hat, we choose the basis vectors for transverse electric and transverse magnetic modes as

$$\hat{\mathbf{e}}_{\text{TE}} \equiv \hat{\mathbf{e}}_\varphi = \begin{pmatrix} -\sin \varphi \\ \cos \varphi \\ 0 \end{pmatrix}, \quad \hat{\mathbf{e}}_{\text{TM}} \equiv \hat{\mathbf{e}}_\theta = \begin{pmatrix} \cos \theta \cos \varphi \\ \cos \theta \sin \varphi \\ -\sin \theta \end{pmatrix}. \quad (2.27)$$

Moreover, both configurations are time-independent, implying that the frequency is conserved during scattering processes. For this reason, it is convenient to fix the frequency ω by means of the dispersion relation $\omega = cK$. It is then sufficient to give the projection $\mathbf{k} = (K_x, K_y, 0)$ of the wave vector \mathbf{K} onto the x - y plane. The z -component of the wave vector is uniquely determined by

$$K_z = \phi k_z, \quad k_z \equiv \left(\frac{\omega^2}{c^2} - \mathbf{k}^2 \right)^{1/2}, \quad (2.28)$$

where ϕ denotes the direction of propagation in the z -direction. The positive sign $\phi = +1$ denotes a wave propagating upwards, whereas $\phi = -1$ refers to a wave propagating in the opposite direction. Changing the integration from K_z to ω , the expansion (2.26) of the electric field becomes

$$\mathbf{E}(\mathbf{R}, t) = \sum_{p=\text{TE, TM}} \sum_{\phi=\pm 1} \int_{c|\mathbf{k}|}^{\infty} \frac{d\omega}{c} \int \frac{d^2\mathbf{k}}{(2\pi)^2} \frac{\hat{\mathbf{e}}_p}{2\pi} \frac{\omega}{c^2 k_z} \left(\alpha_{p,\phi}(\omega, \mathbf{k}) e^{-i(\omega t - \mathbf{k} \cdot \mathbf{r} - \phi k_z z)} \right. \\ \left. + \alpha_{p,\phi}^*(\omega, \mathbf{k}) e^{i(\omega t - \mathbf{k} \cdot \mathbf{r} - \phi k_z z)} \right) \quad (2.29)$$

where the factor $\omega/(c^2 k_z)$ corresponds to the Jacobian.

The expansion (2.29) contains only propagating modes described by real wave vectors. In vacuum, imaginary wave vectors cannot exist since they lead to diverging fields which are unphysical. However, the situation changes when scattering objects are placed inside the vacuum. Then, besides propagating waves, evanescent waves described by imaginary wave vectors can also exist and need to be taken into account [70]. Due to the rotational symmetry about the z -axis, the transverse components k_x, k_y of the wave vector remain real to avoid diverging fields. In contrast, the z -component of the wave vector may become imaginary. From (2.28) we find that frequencies $\omega \geq c|\mathbf{k}|$ correspond to propagative modes with k_z real, while frequencies $0 \leq \omega < c|\mathbf{k}|$ represent evanescent waves with k_z purely imaginary. In order to include evanescent modes, we change the lower integration limit in (2.29) to 0.

Hence, the expansion becomes

$$\mathbf{E}(\mathbf{R}, t) = \int_0^{\infty} \frac{d\omega}{c} \left(\mathbf{E}(\mathbf{R}) e^{-i\omega t} + \mathbf{E}^*(\mathbf{R}) e^{i\omega t} \right) \quad (2.30)$$

with

$$\mathbf{E}(\mathbf{R}) = \sum_{p=\text{TE, TM}} \sum_{\phi=\pm 1} \int \frac{d^2\mathbf{k}}{(2\pi)^2} \tilde{\alpha}_{p,\phi}(\omega, \mathbf{k}) \langle x, y, z | \omega, \mathbf{k}, p, \phi \rangle. \quad (2.31)$$

This is the angular spectral representation of the plane-wave basis [71]. The basis elements are expressed as $|\omega, \mathbf{k}, p, \phi\rangle$, and in position space they are given by

$$\langle x, y, z | \omega, \mathbf{k}, p, \phi \rangle = \hat{\epsilon}_p \left(\frac{1}{2\pi} \left| \frac{\omega}{ck_z} \right| \right)^{1/2} e^{i(\mathbf{k}\cdot\mathbf{r} + \phi k_z z)} \quad (2.32)$$

where $\mathbf{r} = (x, y, 0)$.

We will also express the wave vector \mathbf{K} in spherical coordinates

$$\mathbf{K} = \frac{\omega}{c} \left(\sin \theta_{\mathbf{k}}^\phi \cos \varphi_{\mathbf{k}}, \sin \theta_{\mathbf{k}}^\phi \sin \varphi_{\mathbf{k}}, \cos \theta_{\mathbf{k}}^\phi \right). \quad (2.33)$$

The angles $\theta_{\mathbf{k}}^\phi, \varphi_{\mathbf{k}}$ are determined by

$$\sin \theta_{\mathbf{k}}^\phi = \frac{ck}{\omega}, \quad \cos \theta_{\mathbf{k}}^\phi = \phi \frac{ck_z}{\omega}, \quad \cos \varphi_{\mathbf{k}} = \frac{k_x}{k}, \quad \sin \varphi_{\mathbf{k}} = \frac{k_y}{k}, \quad (2.34)$$

where $k = |\mathbf{k}|$. Within the scattering approach, the Casimir free energy is usually expressed in terms of imaginary frequencies $\omega = i\xi, \xi \in \mathbb{R}$. For imaginary frequencies, the z -component of the wave vector becomes purely imaginary and it is convenient to define $k_z \equiv i\kappa$ with

$$\kappa \equiv \sqrt{\frac{\xi^2}{c^2} + k^2}. \quad (2.35)$$

The polar angle $\theta_{\mathbf{k}}^\phi$ also becomes imaginary

$$\sin \theta_{\mathbf{k}}^\phi = -i \frac{ck}{\xi}, \quad \cos \theta_{\mathbf{k}}^\phi = \phi \frac{c\kappa}{\xi}, \quad (2.36)$$

while the expressions for the azimuth angle $\varphi_{\mathbf{k}}$ remain unchanged.

2.3 The translation operator

In the scattering approach the central object is the round-trip operator. Typically, the round-trip operator consists among others of translation operators. Evaluating the basis functions of the plane-wave basis in position space at $\mathbf{R} + a\hat{\mathbf{e}}_z$

$$\langle \mathbf{R} + a\hat{\mathbf{e}}_z | \omega, \mathbf{k}, p, \phi \rangle = e^{i\phi k_z a} \langle \mathbf{R} | \omega, \mathbf{k}, p, \phi \rangle, \quad (2.37)$$

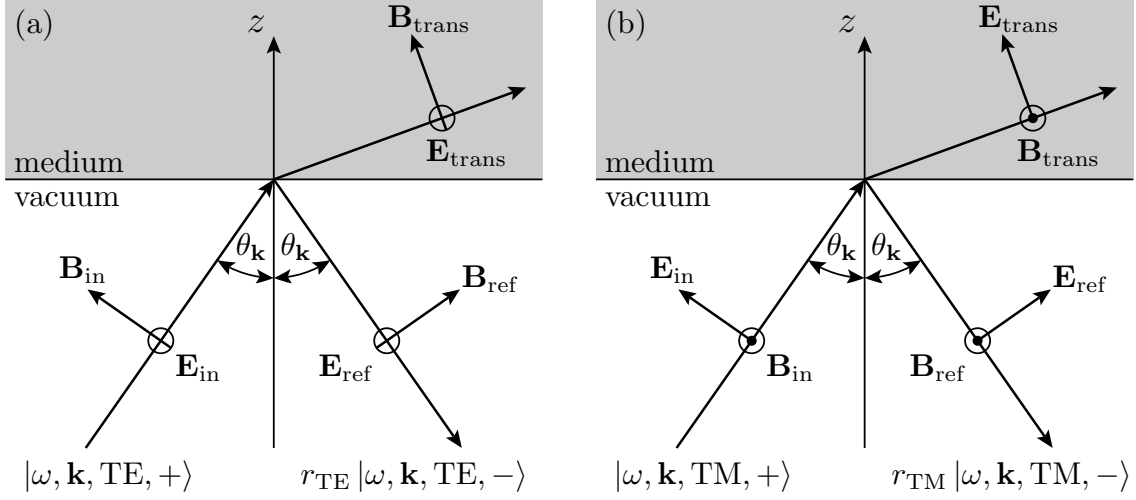


Figure 2.1: Scattering of plane-waves with (a) TE and (b) TM polarization at an interface between vacuum and a homogeneous medium. During the reflection, the wave vector projection \mathbf{k} , the polarization p , and the frequency ω are preserved, while the direction of propagation changes. The reflection coefficients r_p correspond to the Fresnel coefficients. The subscripts in, ref, and trans denote incident, reflected, and transmitted fields. (adapted from [55])

we find that a translation along the z -axis is diagonal in the plane-wave basis. The translation operator implementing the translation from z to $z + a$ is described by

$$\mathcal{T}(a) |\omega, \mathbf{k}, p, \phi\rangle = e^{i\phi k_z a} |\omega, \mathbf{k}, p, \phi\rangle . \quad (2.38)$$

For imaginary frequencies, this becomes

$$\mathcal{T}(a) |\xi, \mathbf{k}, p, \phi\rangle = e^{-\phi \kappa a} |\xi, \mathbf{k}, p, \phi\rangle . \quad (2.39)$$

2.4 Scattering at a plane

The Casimir effect in the geometries of two parallel planes and a sphere above a plane both involve the scattering at a planar surface. We consider the interface of vacuum and a homogeneous medium separated by the plane $z = 0$ with vacuum for $z < 0$. For simplicity, we restrict ourselves to non-magnetic media described by the dielectric function $\epsilon(\omega)$. The plane-wave basis is well adapted for this situation: As the angle of incidence is equal to the angle of reflection, the projection of the wave vector onto the x - y plane is conserved, i.e., incident and reflected plane waves are described by the same vector \mathbf{k} . Moreover, the frequency ω and the polarization $p = \{\text{TE}, \text{TM}\}$ are also conserved during the reflection, while the direction of propagation changes. The reflection operator \mathcal{R}_P acting on an element of the plane-wave basis yields

$$\mathcal{R}_P |\omega, \mathbf{k}, p, +\rangle = r_p |\omega, \mathbf{k}, p, -\rangle , \quad (2.40)$$

with the Fresnel coefficients [55]

$$r_{\text{TE}}(\theta_{\mathbf{k}}) = \frac{\cos \theta_{\mathbf{k}} - \sqrt{\epsilon(\omega) - \sin^2 \theta_{\mathbf{k}}}}{\cos \theta_{\mathbf{k}} + \sqrt{\epsilon(\omega) - \sin^2 \theta_{\mathbf{k}}}}, \quad (2.41a)$$

$$r_{\text{TM}}(\theta_{\mathbf{k}}) = \frac{\epsilon(\omega) \cos \theta_{\mathbf{k}} - \sqrt{\epsilon(\omega) - \sin^2 \theta_{\mathbf{k}}}}{\epsilon(\omega) \cos \theta_{\mathbf{k}} + \sqrt{\epsilon(\omega) - \sin^2 \theta_{\mathbf{k}}}}. \quad (2.41b)$$

The scattering is depicted in Fig. 2.1. If the z -axis is flipped, i.e., vacuum for $z > 0$ and medium for $z < 0$, (2.40) becomes

$$\mathcal{R}_{\text{P}} |\omega, \mathbf{k}, p, -\rangle = r_p |\omega, \mathbf{k}, p, +\rangle. \quad (2.42)$$

For imaginary frequencies the Fresnel coefficients become

$$r_{\text{TE}}(i\xi, k) = \frac{c\kappa - \sqrt{c^2\kappa^2 + \xi^2 [\epsilon(i\xi) - 1]}}{c\kappa + \sqrt{c^2\kappa^2 + \xi^2 [\epsilon(i\xi) - 1]}}, \quad (2.43a)$$

$$r_{\text{TM}}(i\xi, k) = \frac{\epsilon(i\xi)c\kappa - \sqrt{c^2\kappa^2 + \xi^2 [\epsilon(i\xi) - 1]}}{\epsilon(i\xi)c\kappa + \sqrt{c^2\kappa^2 + \xi^2 [\epsilon(i\xi) - 1]}}, \quad (2.43b)$$

and the dielectric function is evaluated at the imaginary axis. Here, we have used (2.36) to express sine and cosine in terms of ξ , k , and κ .

2.5 The plasma and Drude model

Within linear response theory, the interaction of the metal with electromagnetic radiation is described by the dielectric function $\epsilon(\omega)$. Assuming that metals reflect radiation perfectly for all frequencies ω and do not absorb or transmit any radiation, the dielectric function is given by $\epsilon(\omega) \rightarrow -\infty$. Metals described by this dielectric function are called perfect reflectors. For perfect reflectors the Fresnel coefficients are given by

$$r_{\text{TM}}^{\text{PR}} = 1, \quad r_{\text{TE}}^{\text{PR}} = -1, \quad (2.44)$$

and they are independent of the frequency and the wave vector.

The optical properties of metals at high frequencies are better described by the plasma model with the relative permittivity

$$\epsilon^{\text{plasma}}(\omega) = 1 - \frac{\omega_{\text{P}}^2}{\omega^2}, \quad (2.45)$$

where ω_{P} denotes the plasma frequency. The plasma model assumes that the conducting electrons move freely within the metal while the ion cores are static. Up to frequencies of the order of the plasma frequency ω_{P} , metals are good reflectors. For frequencies higher

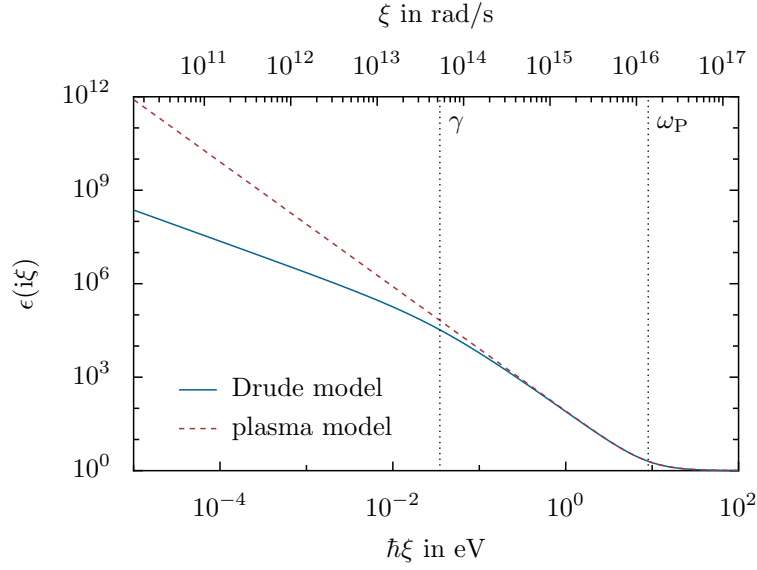


Figure 2.2: Relative permittivity $\epsilon(i\xi)$ as a function of the imaginary frequency ξ for the Drude model (solid line) and the plasma model (dashed line). The parameters $\hbar\omega_P = 9 \text{ eV}$ and $\hbar\gamma = 35 \text{ meV}$ correspond to typical values of gold. The dotted lines denote the plasma frequency ω_P and the relaxation frequency γ .

than the plasma frequency, the inertia of the electrons is too large for them to follow the electric field and the material becomes transparent. The relative permittivity is connected to the conductivity $\sigma(\omega)$ by

$$\epsilon(\omega) = 1 + i \frac{\sigma(\omega)}{\epsilon_0 \omega}. \quad (2.46)$$

For the plasma model the conductivity diverges like $1/\omega$ for small frequencies, yielding an infinite dc conductivity. Therefore, the plasma model cannot be regarded as a good description of metals at low frequencies.

The simplest model predicting a finite dc conductivity is the Drude model

$$\epsilon^{\text{Drude}}(\omega) = 1 - \frac{\omega_P^2}{\omega(\omega + i\gamma)}. \quad (2.47)$$

The Drude model assumes that the conducting electrons achieve thermal equilibrium by scattering with the ion cores, thus introducing the relaxation frequency γ . Setting $\gamma = 0$ the plasma model is recovered. For metals the relaxation frequency is typically much smaller than the plasma frequency. For instance, the plasma frequency of gold is $\hbar\omega_P \approx 9 \text{ eV}$ and the relaxation frequency is $\hbar\gamma \approx 35 \text{ meV}$ [72]. Both values depend on the preparation of the gold sample and thus vary from one reference to another.

For imaginary frequencies the plasma and the Drude model become

$$\epsilon^{\text{plasma}}(i\xi) = 1 + \frac{\omega_P^2}{\xi^2}, \quad \epsilon^{\text{Drude}}(i\xi) = 1 + \frac{\omega_P^2}{\xi(\xi + \gamma)}. \quad (2.48)$$

In Fig. 2.2 the relative permittivity for imaginary frequencies is shown for the Drude and the plasma model using typical parameters of gold. For frequencies $\xi \gtrsim \omega_p$ the relative permittivity approaches 1 and the metal becomes transparent in both models. For frequencies smaller than the relaxation frequencies $\xi \lesssim \gamma$, the dielectric functions of the Drude and the plasma model start deviating. While the dielectric function of the plasma model diverges like ω_p^2/ξ^2 for small frequencies, the dielectric function of the Drude model diverges like $\omega_p^2/\gamma\xi$. The different behavior of both models for small frequencies has severe consequences for the Fresnel coefficient for TE polarization [73]. While in the Drude model the Fresnel coefficient for TE polarization vanishes

$$r_{\text{TE}}^{\text{Drude}}(0, k) = 0, \quad (2.49)$$

the plasma model yields the finite value

$$r_{\text{TE}}^{\text{plasma}}(0, k) = \frac{c\kappa - \sqrt{c^2\kappa^2 + \omega_p^2}}{c\kappa + \sqrt{c^2\kappa^2 + \omega_p^2}}. \quad (2.50)$$

Evidently, the limits $\xi \rightarrow 0$ and $\gamma \rightarrow 0$ do not commute, and there is no continuous transition from the Drude model to the plasma model [74]. As a consequence, both the Casimir force and the Casimir free energy differ in the high-temperature limit by a factor of 2 for the Drude and the plasma model. For a more extensive discussion whether or not the transverse electric mode for $\xi \rightarrow 0$ contributes, see for example Refs. [75, 76]. The Fresnel coefficient r_{TM} tends to 1 in the limit $\xi \rightarrow 0$ for both the plasma and the Drude model.

Since the plasma model predicts an infinite dc conductivity, it cannot be regarded as a good model for metals at low frequencies. Surprisingly, most experiments are in better agreement with the lossless plasma model than with the Drude model [9, 10, 39, 40, 42]. A few experiments found agreement with the Drude model [30, 31, 77], but the results have also been questioned [46, 47]. This puzzle is also known as the Drude vs plasma controversy, and we will discuss it in more detail in chapter 7.

2.6 The dielectric function from optical data

Precise measurements of the Casimir force are carried out using metallic surfaces. The dielectric function of metals starts deviating from the Drude model once interband transitions are reached. An adequate comparison between theory and experiment thus requires the use of tabulated experimental data of the dielectric function. While in experiments the dielectric function is measured for real frequencies, the Casimir energy in the scattering approach is commonly evaluated at imaginary frequencies. Here, we derive a relation

between the dielectric function at imaginary frequencies and the imaginary part of the dielectric function at real frequencies. The general idea is discussed in Ref. [72], a detailed analysis of the dependence of the optical properties on the method of preparation and the variation of the Casimir force when using different optical data can be found in Ref. [78].

As the dielectric function $\epsilon(t)$ is real in the time domain, it obeys the symmetry $\epsilon(-\omega) = \epsilon^*(\omega)$ in the frequency domain, and the real part $\epsilon'(\omega)$ of the dielectric function is an even function, while the imaginary part $\epsilon''(\omega)$ is an odd function. The dielectric function at the imaginary axis can be obtained using the integral

$$\oint_{\mathcal{C}} dx x \frac{\epsilon(x) - 1}{x^2 + \omega^2} = \int_{-\infty}^{\infty} dx x \frac{\epsilon(x) - 1}{x^2 + \omega^2} = i\pi [\epsilon(i\omega) - 1], \quad (2.51)$$

where the integration contour \mathcal{C} is the real axis closed by a half-circle in the upper half plane. Due to high-frequency transparency, the half-circle does not contribute to the integral. Since $\epsilon'(x) - 1$ is an even function, only the imaginary part $\epsilon''(x)$ contributes to the integral and the dielectric function $\epsilon(i\omega)$ at the imaginary axis can be computed from the imaginary part of $\epsilon''(\omega)$

$$\epsilon(i\omega) - 1 = \frac{2}{\pi} \int_0^{\infty} dx \frac{x\epsilon''(x)}{x^2 + \omega^2}. \quad (2.52)$$

Experimental data for the imaginary part $\epsilon''(\omega)$ of the dielectric function are only available in a finite interval $\omega_{\min} \leq \omega \leq \omega_{\max}$. We split up the integral (2.52) in three contributions

$$\epsilon(i\omega) - 1 = \underbrace{\frac{2}{\pi} \int_0^{\omega_{\min}} dx \frac{x\epsilon''(x)}{x^2 + \omega^2}}_{\equiv \epsilon_1} + \underbrace{\frac{2}{\pi} \int_{\omega_{\min}}^{\omega_{\max}} dx \frac{x\epsilon''(x)}{x^2 + \omega^2}}_{\equiv \epsilon_2} + \underbrace{\frac{2}{\pi} \int_{\omega_{\max}}^{\infty} dx \frac{x\epsilon''(x)}{x^2 + \omega^2}}_{\equiv \epsilon_3}. \quad (2.53)$$

As $\hbar\omega_{\max} \simeq 10^4$ eV and $\epsilon''(\omega_{\max}) \simeq 5 \times 10^{-6}$, the contribution from ϵ_3 is negligible. The integral ϵ_2 can be evaluated using numerical quadrature. Typically, many points are available in this domain such that the integration causes no problems. Since no data are available for frequencies $\omega < \omega_{\min}$, the computation of ϵ_1 relies on an extrapolation of the optical data. Using the Drude model

$$\epsilon^{\text{Drude}}(\omega) = 1 - \frac{\omega_{\text{P}}^2}{\omega(\omega + i\gamma)} \quad (2.54)$$

to extrapolate the data to low frequencies, the integral ϵ_1 becomes

$$\epsilon_1 = \frac{2}{\pi} \frac{\omega_{\text{P}}^2}{\omega^2 - \gamma^2} \left[\arctan\left(\frac{\omega_{\min}}{\gamma}\right) - \frac{\gamma}{\omega} \arctan\left(\frac{\omega_{\min}}{\omega}\right) \right]. \quad (2.55)$$

The value of ϵ_1 depends sensitively on the value of the plasma frequency.

A metal commonly used in Casimir measurements is gold. The imaginary part $\epsilon''(\omega)$ of gold measured by Olmon *et al.* [80], Werner *et al.* [82], Brändli *et al.* [81], and the handbook

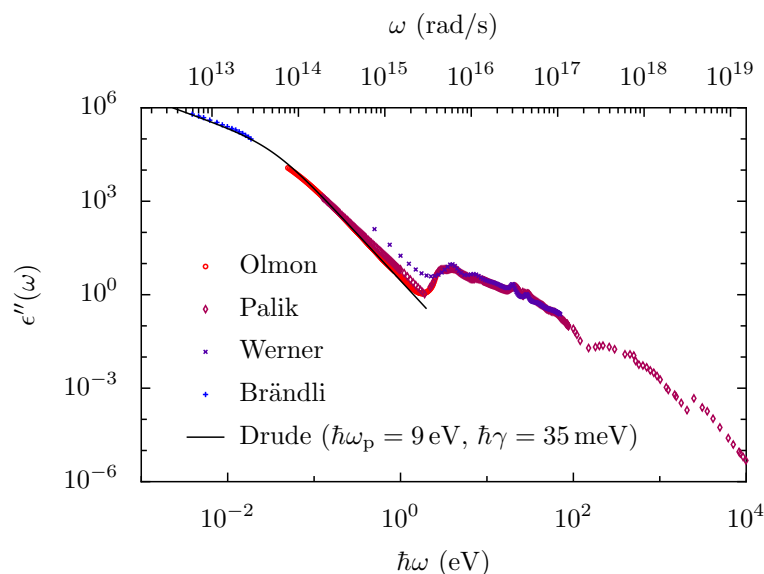


Figure 2.3: Imaginary part of the dielectric function $\epsilon''(\omega)$ for the data of Palik [79], and the experiments by Olmon *et al.* (EV; evaporated gold samples) [80], Brändli *et al.* [81], and Werner *et al.* [82]. The full line corresponds to the imaginary part of the Drude model (2.54).

data edited by Palik [79] is shown in Fig. 2.3 as a function of the frequency ω . The full line corresponds to the Drude model (2.54) with plasma frequency $\hbar\omega_p = 9$ eV and relaxation frequency $\hbar\gamma = 35$ meV. The Drude model is a reasonable fit of the data up to frequencies $\hbar\omega \sim 1$ eV, at higher frequencies interband transitions become important.

Fig. 2.4 depicts the dielectric function evaluated at imaginary frequencies obtained from Palik's handbook data [79]. For the extrapolation to small frequencies the Drude model with parameters $\hbar\omega_p = 9$ eV and $\hbar\gamma = 35$ meV has been used. The full line corresponds to the dielectric function at imaginary frequencies, the dashed and dash-dotted lines represent the contributions from ϵ_1 and ϵ_2 , respectively. Up to $\hbar\omega \lesssim 3$ eV, the dominant contribution comes from the extrapolation of the optical data using the Drude model. Since ϵ_1 sensitively depends on ω_p , it is important to determine the plasma frequency with high accuracy. Unfortunately, depending on the set of optical data, different values for the plasma frequency have been found: For the handbook data of Palik [79], the authors of Ref. [72] found $\hbar\omega_p = 9$ eV using estimates from solid state physics, while Pirozhenko *et al.* [78] obtained $\hbar\omega_p = 7.5$ eV by fitting the available infrared data for the real and imaginary part of the dielectric function. The plasma frequency obtained by Olmon *et al.* [80] depends on the method of preparation and ranges from 8.1 to 8.8 eV. Svetovoy *et al.* [83] also found that the plasma frequency depends on preparation with $\hbar\omega_p$ varying from 6.8 to 8.4 eV. As a consequence, the Casimir force for gold surfaces at room temperature may vary up to about 5% at distances $L \sim 100$ nm depending on the optical data used [78]. For this reason, a precise comparison between theory and experiment requires the gold samples to be prepared under well-defined conditions, and a measurement of the plasma

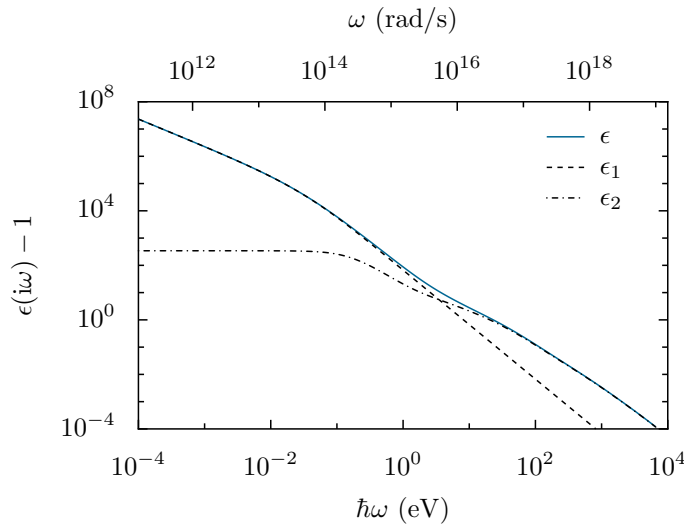


Figure 2.4: Dielectric function for imaginary frequencies obtained from Palik’s handbook data [79]. For the extrapolation to low frequencies the plasma frequency $\hbar\omega_P = 9\text{ eV}$ and the relaxation frequency $\hbar\gamma = 35\text{ meV}$ have been used. The full line corresponds to the dielectric function, the dashed and dash-dotted lines represent the contributions from ϵ_1 and ϵ_2 in (2.53).

frequency.

In order to decrease the contribution of ϵ_1 , it was proposed to alter the Kramers-Kronig relations by a window function $f(x)$ [84, 85]. More precisely, using the same derivation as before for $f(x)[\epsilon(x) - 1]$, one finds

$$\epsilon(i\omega) - 1 = \frac{2}{\pi f(i\omega)} \int_0^\infty dx \frac{x}{x^2 + \omega^2} \text{Im} \{ f(x) [\epsilon(x) - 1] \}. \quad (2.56)$$

The window function $f(x)$ can now be chosen in such a way that it suppresses the contribution of ϵ_1 . This method has been used in the analysis of a recent experiment [39]. However, it has been criticized that the use of a window function may amplify experimental errors in the optical data [86].

2.7 The plane-plane geometry

We will now consider the geometry of two parallel and infinite mirrors in vacuum that are separated by a distance L . For this geometry, Casimir found in 1948 an attractive force for perfect reflectors at zero temperature [1]. Casimir’s result was then generalized by Lifshitz to finite temperature and arbitrary dielectric materials [87]. The first experimental measurement of the Casimir force between two parallel mirrors was performed by Sparnaay in 1958 [88]. Due to large systematic errors and electrostatic forces, the accuracy of this experiment was poor, and Sparnaay concluded that his results “do not contradict

Casimir's prediction" [88]. In 2002 Bressi *et al.* were able to measure the Casimir force in the plane-plane geometry in the 0.5–3.0 μm range with 15% precision [89].

Apart from these remarkable experiments, most other experiments adopt the geometry of a plane and a sphere to avoid misalignments between the two plates. Experimental results are compared with theory using the proximity force approximation that we will introduce in the next chapter. The approximation links the Casimir free interaction energy in the plane-plane geometry with the Casimir force in the plane-sphere geometry. Therefore, within the proximity force approximation, the computation of the Casimir force in the plane-sphere geometry relies on the formula for the geometry of two parallel planes.

We first derive the Casimir force between the two mirrors by comparing the vacuum pressure inside and outside the cavity. We then discuss the Casimir interaction for perfect reflectors, and metals described by the plasma and the Drude model. While the plasma and the Drude model yield significant deviations from the results for perfect reflectors for distances comparable or smaller than the plasma wavelength $\lambda_P = 2\pi c/\omega_P$, the difference between the Drude and the plasma model at zero temperature is small. However, at finite temperature this is no longer true and the Casimir free energy at high temperatures differs by up to a factor of 2 for the two models.

2.7.1 Vacuum pressure for two parallel mirrors

We consider two parallel mirrors in vacuum separated by a distance L forming a Fabry-Pérot cavity as sketched in Fig. 2.5. The coordinate system is chosen in such a way that both mirrors are parallel to the x - y plane. We label the upper mirror with 2, and the lower mirror with 1. In the following, we follow the derivations given in Refs. [23, 70, 76, 90].

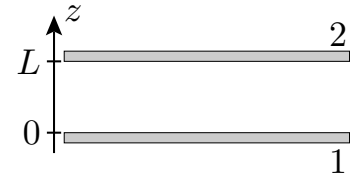


Figure 2.5: plane-plane geometry

The radiation pressure at temperature T outside of the cavity is given by the mean radiation pressure in vacuum

$$P_{\text{vac}} = \langle T_{zz} \rangle_{\text{vac}} = \sum_m \frac{\hbar\omega}{2} C(\omega) \cos^2 \theta_{\mathbf{k}}^{\phi} \quad (2.57)$$

with the number of photons per mode

$$C(\omega) = \coth \left(\frac{\hbar\omega}{2k_{\text{B}}T} \right) = 1 + 2n_{\omega}, \quad n_{\omega} = \frac{1}{\exp \left(\frac{\hbar\omega}{k_{\text{B}}T} \right) - 1}. \quad (2.58)$$

For zero temperature, $C(\omega) = 1$ and therefore we recover (2.22). Inside the cavity, the vacuum pressure is altered by the Airy function g_p [70]

$$P_{\text{cav}} = \langle T_{zz} \rangle_{\text{cav}} = \sum_m \frac{\hbar\omega}{2} C(\omega) g_p(\omega, \mathbf{k}) \cos^2 \theta_{\mathbf{k}}^\phi. \quad (2.59)$$

The Airy function

$$g_p(\omega, \mathbf{k}) = 1 + f_p(\omega, \mathbf{k}) + f_p^*(\omega, \mathbf{k}) \quad (2.60)$$

corresponds to the ratio of energy inside the cavity to energy outside the cavity for a given mode. Here, the closed-loop function

$$f_p(\omega, \mathbf{k}) = \sum_{n=1}^{\infty} \rho_p^n(\omega, \mathbf{k}) = \frac{\rho_p(\omega, \mathbf{k})}{1 - \rho_p(\omega, \mathbf{k})} \quad (2.61)$$

is given as a sum over the open-loop function

$$\rho_p(\omega, \mathbf{k}) = r_p^{(1)}(\omega, \mathbf{k}) r_p^{(2)}(\omega, \mathbf{k}) e^{2ik_z L}, \quad (2.62)$$

where the superscripts indicate the plane for which the Fresnel coefficient has to be taken. The open-loop function describes a complete round trip of an electromagnetic wave in the cavity.

The pressure acting on the mirrors is now merely the difference of the radiation pressure P_{cav} inside the cavity and the radiation pressure P_{vac} outside the cavity

$$\begin{aligned} P &= P_{\text{cav}} - P_{\text{vac}} = \sum_m \frac{\hbar\omega}{2} C(\omega) (g_p(\omega, \mathbf{k}) - 1) \cos^2 \theta_{\mathbf{k}}^\phi \\ &= \sum_m \frac{\hbar\omega}{2} C(\omega) (g_p(\omega, \mathbf{k}) - 1) \frac{c^2 k_z^2}{\omega^2}. \end{aligned} \quad (2.63)$$

The sign is chosen such that an attractive force corresponds to a negative pressure. Modes with $g_p > 1$ correspond to repelling contributions to the pressure P , and modes with $g_p < 1$ represent attracting contributions. As in the derivation of the plane-wave basis, it is convenient to express the summation over propagative and evanescent modes as summation over polarization p and integration over \mathbf{k} and ω . The pressure then becomes

$$P = \hbar \sum_{p=\text{TE, TM}} \int \frac{d^2\mathbf{k}}{(2\pi)^2} \int_0^\infty \frac{d\omega}{2\pi} C(\omega) (k_z f_p(\omega, \mathbf{k}) + k_z^* f_p^*(\omega, \mathbf{k})). \quad (2.64)$$

2.7.2 The Lifshitz formula

As the Airy function (2.60) is a causal function, the closed-loop function obeys $f_p(-\omega, \mathbf{k}) = -f_p^*(\omega, \mathbf{k})$. For real frequencies, the cotangent is an odd function and $C(-\omega) = -C(\omega)$.

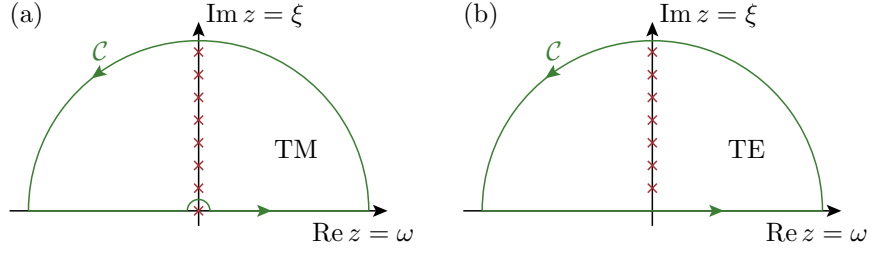


Figure 2.6: Integration contour C and positions of the poles for the integrand (2.66) for (a) TM and (b) TE polarization. Red crosses correspond to the poles of the cotangent. For TE polarization, the pole of $C(z)$ at $z = 0$ is removed by the Fresnel coefficient r_{TE} . Due to high-frequency transparency, the half-circles yield no contribution.

Choosing the definition of the square root such that $k_z(-\omega) = -k_z^*(\omega)$, the integration over ω can be extended to the whole real axis and the pressure becomes

$$P = \hbar \sum_{p=\text{TE, TM}} \int \frac{d^2\mathbf{k}}{(2\pi)^2} \int_{-\infty}^{\infty} \frac{d\omega}{2\pi} C(\omega) k_z f_p(\omega, \mathbf{k}). \quad (2.65)$$

We now extend the integration to the complex plane by closing the integration contour with an infinite half-circle in the upper half of the complex plane as depicted in Fig. 2.6. The half-circle gives no contribution due to high-frequency transparency of the mirrors. With $z \equiv \omega + i\xi$ the expression for the pressure becomes

$$P = \hbar \sum_{p=\text{TE, TM}} \int \frac{d^2\mathbf{k}}{(2\pi)^2} \oint_C \frac{dz}{2\pi} C(z) k_z f_p(z, \mathbf{k}). \quad (2.66)$$

The functions f_p and k_z are analytic in the upper half of the complex plane, and the function $C(z)$ has poles at the Matsubara frequencies $z = i\xi_n$

$$\xi_n = \frac{2\pi n k_B T}{\hbar}, \quad n \in \mathbb{Z}. \quad (2.67)$$

Assuming metallic mirrors with finite dc conductivity, the Fresnel coefficient for TE polarization vanishes for $\xi \rightarrow 0$, thereby removing the pole of $C(z)$ at $z = 0$. The positions of the poles of the integrand of (2.66) for TM and TE polarization are depicted in Fig. 2.6.

The Casimir pressure can now be written as a sum over Matsubara frequencies. Due to the residue theorem, the integral (2.66) is equal to the sum over the residues of the poles times $2\pi i$

$$P = -2k_B T \int \frac{d^2\mathbf{k}}{(2\pi)^2} \kappa \left[\frac{1}{2} f_{\text{TM}}(0, \mathbf{k}) + \sum_{p=\text{TE, TM}} \sum_{n=1}^{\infty} f_p(i\xi_n, \mathbf{k}) \right]. \quad (2.68)$$

Noting that the Fresnel coefficient for TE polarization vanishes for $\xi = 0$, we can add $f_{\text{TE}}(0, \mathbf{k})$ in order to simplify the expression

$$P = -2k_{\text{B}}T \sum_{p=\text{TE, TM}} \sum'_{n=0} \int \frac{d^2\mathbf{k}}{(2\pi)^2} \kappa \frac{r_p^{(1)} r_p^{(2)} e^{-2\kappa L}}{1 - r_p^{(1)} r_p^{(2)} e^{-2\kappa L}}. \quad (2.69)$$

The primed sum is used frequently in the Casimir community to indicate that the term $n = 0$ is counted as half

$$\sum'_{n=0} f_n = \frac{1}{2} f_0 + \sum_{n=1} f_n. \quad (2.70)$$

We will avoid this notation by extending the summation to negative values of n

$$P = \frac{F}{A} = -k_{\text{B}}T \sum_{p=\text{TE, TM}} \sum_{n=-\infty}^{\infty} \int \frac{d^2\mathbf{k}}{(2\pi)^2} \kappa \frac{r_p^{(1)} r_p^{(2)} e^{-2\kappa L}}{1 - r_p^{(1)} r_p^{(2)} e^{-2\kappa L}}, \quad (2.71)$$

where the Fresnel coefficients are evaluated at $r_p^{(j)} = r_p^{(j)}(i|\xi_n|, k)$. By means of the thermodynamic relation $F = -\partial\mathcal{F}/\partial L$, the Casimir free interaction energy is obtained as

$$\frac{\mathcal{F}}{A} = \frac{k_{\text{B}}T}{2} \sum_{p=\text{TE, TM}} \sum_{n=-\infty}^{\infty} \int \frac{d^2\mathbf{k}}{(2\pi)^2} \log \left(1 - r_p^{(1)} r_p^{(2)} e^{-2\kappa L} \right). \quad (2.72)$$

It is convenient to evaluate the integral in (2.72) in polar coordinates. Due to the rotational symmetry around the z -axis, the integrand does not depend on the polar angle and the integration gives 2π . Changing the integration variable from k to κ , we arrive at the Lifshitz formula [87]

$$\frac{\mathcal{F}}{A} = \frac{k_{\text{B}}T}{4\pi} \sum_{n=-\infty}^{\infty} \sum_{p=\text{TE, TM}} \int_{|\xi_n|/c}^{\infty} d\kappa \kappa \log \left[1 - r_p^{(1)}(i|\xi_n|, k) r_p^{(2)}(i|\xi_n|, k) e^{-2\kappa L} \right]. \quad (2.73)$$

Eq. (2.73) gives the Casimir free interaction energy per area for real materials described by their dielectric functions. The expression is valid under the assumptions that the area of the plates is large compared to the squared separation, $A \gg L^2$, and that the width of the plates is thicker than a few plasma wavelengths.

For the sake of simplicity, in the following we assume that both plates have the same dielectric properties so that the reflection can be described by the same Fresnel coefficients.

2.7.3 Perfect reflectors

For perfect reflectors the Fresnel coefficients are given by $r_{\text{TM}} = -r_{\text{TE}} = 1$. As only the square of the Fresnel coefficients enter the Lifshitz formula, both polarizations yield the same contribution to the free energy. Evaluating the integration over κ , the free energy

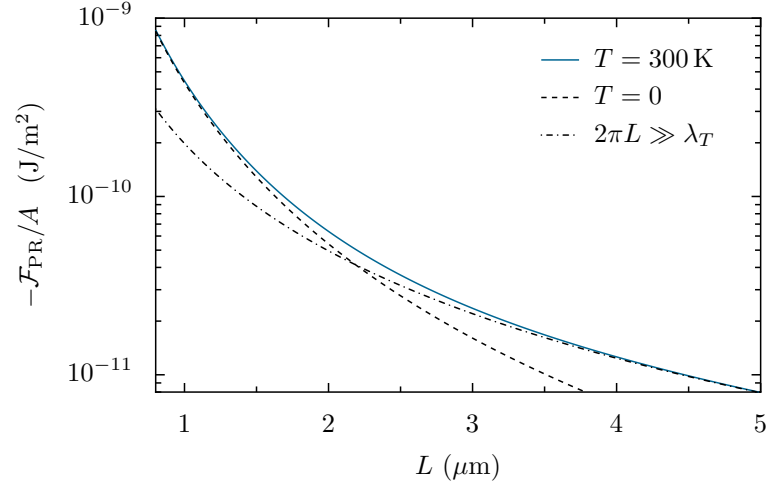


Figure 2.7: Casimir free energy per area as a function of the separation L of the two plates for perfect reflectors. The solid line corresponds to room temperature $T = 300$ K, the dashed line and the dash-dotted line denote the zero temperature limit (2.77) and the high-temperature limit (2.78), respectively.

becomes

$$\frac{\mathcal{F}_{\text{PR}}}{A} = -\frac{k_{\text{B}}T}{8\pi L^2} \sum_{n=-\infty}^{\infty} \left[\text{Li}_3 \left(e^{-2|\xi_n|L/c} \right) + \frac{2|\xi_n|L}{c} \text{Li}_2 \left(e^{-2|\xi_n|L/c} \right) \right], \quad (2.74)$$

where $\text{Li}_s(z)$ denotes the polylogarithm of order s and argument z [91, §25.12]. For low temperatures $2\pi L \ll \lambda_T$, where $\lambda_T = \hbar c/k_{\text{B}}T$ denotes the thermal wavelength, the summation over the Matsubara frequencies becomes dense and can be replaced by an integral

$$\frac{k_{\text{B}}T}{2} \sum_{n=-\infty}^{\infty} \rightarrow \hbar \int_0^{\infty} \frac{d\xi}{2\pi}. \quad (2.75)$$

At room temperature $\lambda_T \simeq 7.6 \mu\text{m}$ and thus thermal corrections become important at separations $L \gtrsim 1 \mu\text{m}$. Replacing the sum by an integral and substituting $x = 2\xi L/c$, (2.74) becomes

$$\frac{\mathcal{F}_{\text{PR}}(T=0)}{A} = -\frac{\hbar c}{16\pi^2 L^3} \int_0^{\infty} dx \left[\text{Li}_3 \left(e^{-x} \right) + x \text{Li}_2 \left(e^{-x} \right) \right]. \quad (2.76)$$

This integral yields $\pi^4/45$ and we find Casimir's famous result for two parallel, perfectly conducting mirrors at zero temperature [1]

$$\frac{\mathcal{F}_{\text{PR}}}{A} = -\frac{\hbar c \pi^2}{720 L^3} \quad \text{for } 2\pi L \ll \lambda_T. \quad (2.77)$$

In the opposite limit of high temperatures $2\pi L \gg \lambda_T$, the argument of the polylogarithms in (2.74) becomes small and the dominant contribution comes from the Matsubara frequency $\xi_0 = 0$. Since the polylogarithm $\text{Li}_s(z)$ reduces to the Riemann zeta function for

$z = 1$, the high-temperature limit reads

$$\frac{\mathcal{F}_{\text{PR}}}{A} = -\frac{k_{\text{B}}T \zeta(3)}{8\pi L^2} \quad \text{for } 2\pi L \gg \lambda_T \quad (2.78)$$

with Apéry's constant $\zeta(3) \approx 1.2020569$.

Fig. 2.7 shows the Casimir free energy per area as a function of the separation L at room temperature $T = 300$ K. As small separations correspond to low temperatures, Casimir's original formula (2.77) is recovered for small separations. With increasing separation the power law of the Casimir free energy undergoes a change from L^{-3} to L^{-2} .

2.7.4 Plasma and Drude model

We will now study the influence of finite conductivity and dissipation on the Casimir energy. At zero temperature the deviation of the Drude and the plasma model from the case of perfect reflectors depends only on the ratio of the separation L and the plasma wavelength $\lambda_{\text{P}} = 2\pi c/\omega_{\text{P}}$. For gold the plasma wavelength is $\lambda_{\text{P}} \simeq 138$ nm. For separations L much larger than the plasma wavelength λ_{P} , the expression (2.77) for perfect reflectors is recovered. This can be seen from the Lifshitz formula (2.73): Due to the exponential factor, the main contribution to the integral comes from values $\xi/c \lesssim \kappa \lesssim 1/L$. This means that the main contributions come from frequencies $\xi \sim c/L$. As metals are good reflectors for frequencies much smaller than the plasma wavelength ω_{P} , the case of perfect reflectors is recovered for $L \gg \lambda_{\text{P}}$.

Fig. 2.8a shows the deviation of the free energy from the case of perfect reflectors at $T = 0$ for the Drude and the plasma model. The curves for the Drude and the plasma model are rather close and dissipation has only a small effect. As expected, for separations much larger than the plasma wavelength the ratio tends to 1. For separations of the order of the plasma wavelength or smaller there is a considerable reduction of the Casimir energy. For the plasma model the correction in this limit was computed by Lambrecht and Reynaud [72]

$$\frac{\mathcal{F}_{\text{plasma}}(T = 0)}{A} = -\frac{\hbar c \pi^2}{480 L^2} \frac{\alpha}{\lambda_{\text{P}}} \quad \text{for } L \ll \lambda_{\text{P}} \quad (2.79)$$

with

$$\alpha = \frac{30\sqrt{2}}{\pi^2} \int_0^\infty dx e^{-x} x^2 \left(\frac{1}{\sqrt{1 - e^{-x}}} - \frac{1}{\sqrt{1 + e^{-x}}} \right) \simeq 1.19334405. \quad (2.80)$$

In contrast, for high temperatures the Drude and the plasma model differ up to a factor of 2 [73]. For $2\pi L \gg \lambda_T$ the dominant contribution to the free energy comes from the zeroth Matsubara frequency. In the Drude model, the Fresnel coefficient for TE polarization

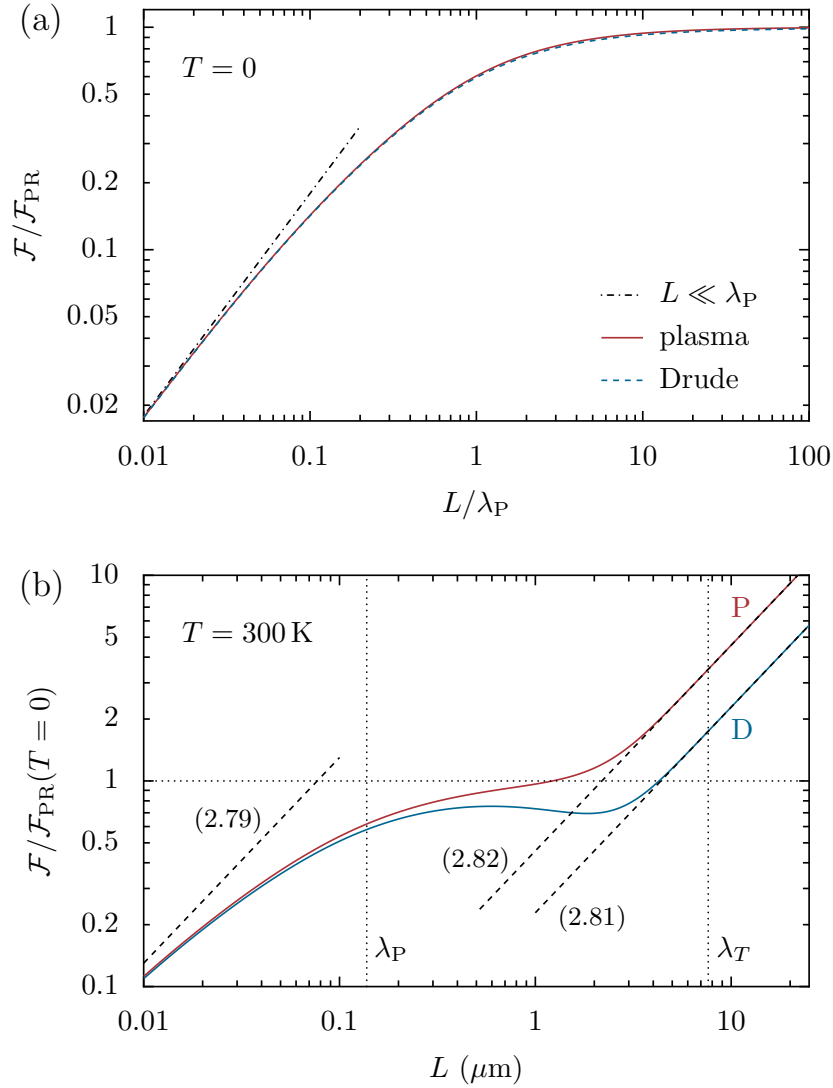


Figure 2.8: (a) Reduction factor for the plasma and the Drude model as a function of L/λ_P at zero temperature. The dash-dotted line corresponds to (2.79). (b) Free energy normalized by the ideal Casimir result (2.77) for the plasma model (P, upper curve) and the Drude model (D, lower curve) at room temperature $T = 300 \text{ K}$. The dashed lines correspond to the limit $L \ll \lambda_P, \lambda_T$ for the plasma model (2.79), and the high temperature limits for the Drude (2.81) and the plasma model (2.82). The parameters for the optical models correspond to gold ($\hbar\omega_P = 9 \text{ eV}$, $\hbar\gamma = 35 \text{ meV}$). Vertical lines depict the values of the plasma wavelength λ_P and the thermal wavelength λ_T .

	perfect reflectors	Drude	plasma
$L \ll \lambda_T$	$-\frac{\hbar c \pi^2}{720 L^3}$ (2.77)	-	$-\frac{\hbar c \pi^2}{480 L^2} \frac{\alpha}{\lambda_P}$ (2.79) for $L \ll \lambda_P$
$L \gg \lambda_T$	$-\frac{k_B T \zeta(3)}{8\pi L^2}$ (2.78)	$-\frac{k_B T \zeta(3)}{16\pi L^2}$ (2.81)	$-\frac{k_B T \zeta(3)}{8\pi L^2}$ (2.82) for $L \gg \lambda_P$

Table 2.1: Analytical limits of the free energy per area \mathcal{F}/A in the plane-plane geometry for perfect reflectors, Drude and plasma model.

vanishes and the high-temperature limit is given by

$$\frac{\mathcal{F}_{\text{Drude}}}{A} = -\frac{k_B T \zeta(3)}{16\pi L^2} \quad \text{for } 2\pi L \gg \lambda_T. \quad (2.81)$$

In the plasma model, however, the TE Fresnel coefficient yields a finite contribution for $\xi \rightarrow 0$. For separations much larger than the plasma wavelength, r_{TE} becomes -1 and the free energy is by a factor of 2 larger than in the Drude model

$$\frac{\mathcal{F}_{\text{plasma}}}{A} = -\frac{k_B T \zeta(3)}{8\pi L^2} \quad \text{for } 2\pi L \gg \lambda_T \quad \text{and} \quad L \gg \lambda_P. \quad (2.82)$$

The analytical limits for the different models are summarized in Tab. 2.1.

The free energy normalized by the zero-temperature limit for perfect reflectors (2.77) is presented for the Drude and the plasma model in Fig. 2.8b. The parameters of the plasma and Drude model correspond to gold, and the temperature is $T = 300$ K. For separations smaller than the plasma wavelength $L \lesssim \lambda_P \simeq 138$ nm, the curves for the Drude and the plasma model coincide and both models are in good agreement. At larger separations, the curves start deviating due to the finite dc conductivity in the Drude model. The difference increases and becomes a factor of 2 in the high-temperature limit. Due to imperfect reflection, the Casimir free energy is decreased with respect to the idealized Casimir energy (2.77) for separations $L \lesssim 1 \mu\text{m}$, while it is increased for larger separations due to the contribution of thermal photons. The dashed lines correspond to the limit $L \ll \lambda_P, \lambda_T$ of the plasma model (2.79), and the high-temperature limits for the Drude (2.81) and the plasma model (2.82).

2.8 The scattering formula

We now generalize the expression (2.72) for the free energy between two parallel planes

$$\frac{\mathcal{F}}{A} = \frac{k_B T}{2} \sum_p \sum_{n=-\infty}^{\infty} \int \frac{d^2 \mathbf{k}}{(2\pi)^2} \log \left(1 - r_p^{(1)} r_p^{(2)} e^{-2\kappa L} \right) \quad (2.83)$$

to objects of arbitrary shape. In the derivation of the Lifshitz formula, we have assumed that the area A of the plates is infinite. In fact, the expression holds, provided that the area of the plates is much larger than the separation, $A \gg L^2$. Using virtual quantization boxes, the integration over the projection of the wave vector can be expressed as an adimensional sum over transverse wave vectors

$$\sum_{\mathbf{k}} = \sum_{n_x \in \mathbb{Z}} \sum_{n_y \in \mathbb{Z}} \frac{2\pi n_x}{L_x} \frac{2\pi n_y}{L_y} \leftrightarrow \frac{A}{(2\pi)^2} \int d^2\mathbf{k}. \quad (2.84)$$

This replacement is valid in the continuum limit $L_x, L_y \rightarrow \infty$ since the summation over the wave vectors on the left-hand side becomes dense. The free energy is then expressed as

$$\mathcal{F} = \frac{k_B T}{2} \sum_{n=-\infty}^{\infty} \sum_p \sum_{\mathbf{k}} \log \left(1 - r_p^{(1)} e^{-\kappa L} r_p^{(2)} e^{-\kappa L} \right). \quad (2.85)$$

The key insight now is that the summation over polarization p and the wave vector projection \mathbf{k} can be expressed as a trace over a diagonal operator [23]. This leads to the scattering formula [23–25]

$$\mathcal{F} = \frac{k_B T}{2} \sum_{n=-\infty}^{\infty} \text{tr} \log [\mathbb{1} - \mathcal{M}(|\xi_n|)]. \quad (2.86)$$

Here, the round-trip operator

$$\mathcal{M} = \mathcal{R}_2 \mathcal{T}_{21} \mathcal{R}_1 \mathcal{T}_{12} \quad (2.87)$$

is the generalization of the open-loop function $\rho_p(i\xi, \mathbf{k})$ to non-specular reflection. The operator \mathcal{T}_{21} describes a translation from the reference frame of object 1 to object 2, and vice versa for \mathcal{T}_{12} . The operators \mathcal{R}_1 and \mathcal{R}_2 denote the reflection operators at object 1 and 2, respectively. The round-trip operator describes a complete round-trip of electromagnetic waves between the two objects. Reading from right to left, the round trip starts with a translation from the frame of reference of object 2 to the frame of reference of object 1, a reflection at object 1, and a translation back to the reference frame of object 2. The loop is closed by a reflection at object 2.

For the plane-plane geometry, the round trip of electromagnetic waves between the two planes is sketched in Fig. 2.9. Each reflection operator introduces a Fresnel coefficient r_p and the two translation operators together yield the exponential $e^{-2\kappa L}$. For more general setups, the reflection operators are typically no longer diagonal and the translation and reflection operators do not commute. Due to the trace, the free energy is invariant under cyclic permutations of the operators in the round-trip operator \mathcal{M} .

The scattering formula (2.86) provides an exact expression for the Casimir free interaction energy of arbitrary materials and geometries at zero and finite temperatures. The expression is valid in thermal equilibrium even if one or both objects, or the medium in between

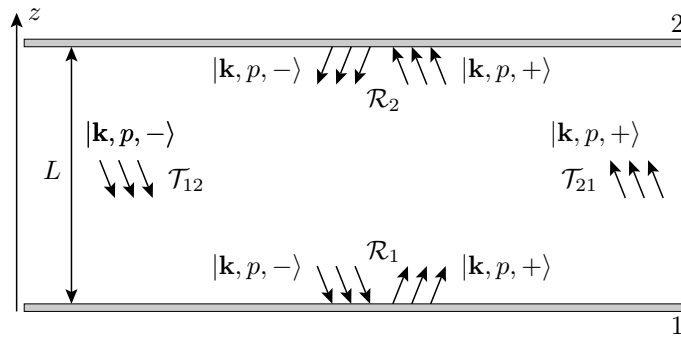


Figure 2.9: A complete round trip in the plane-plane geometry: The reflection operators \mathcal{R}_1 and \mathcal{R}_2 both introduce a Fresnel coefficient r_p , the translation operators \mathcal{T}_{21} and \mathcal{T}_{12} each yield an exponential factor $e^{-\kappa L}$.

are dissipative [92]. Thermal equilibrium means that the fluctuations of the electromagnetic fields, of the electrons, the phonons, or any other loss mechanism correspond to the same temperature [23, 70].

In the following chapters, we will make use of the scattering formula (2.86) to describe the more complicated geometry of a sphere above a plane. In the next chapter, we present the proximity force approximation that links the Casimir energy in the plane-plane geometry to the Casimir force in the plane-sphere geometry. In the subsequent chapters, we numerically evaluate the scattering formula in the plane-sphere geometry and compare the proximity force approximation with numerical results.

Chapter 3

The proximity force approximation

In order to avoid misalignments, experiments typically measure the Casimir interaction between a sphere and a plate. We denote the radius of the sphere by R and the separation of closest approach by L , as shown in Fig. 3.1. In principle, the scattering approach [23–25] introduced in the last chapter allows for an exact computation of the Casimir interaction in this geometry. However, as the numerical evaluation is challenging, all experiments reported in the literature so far use the proximity force approximation (PFA) [27] for comparison with theory. The PFA, also known as Derjaguin approximation, is also employed in surface science [93], in the comparison with experimental results for the van der Waals interaction between spherical colloids [94, 95], and in the study of internuclear forces [96].

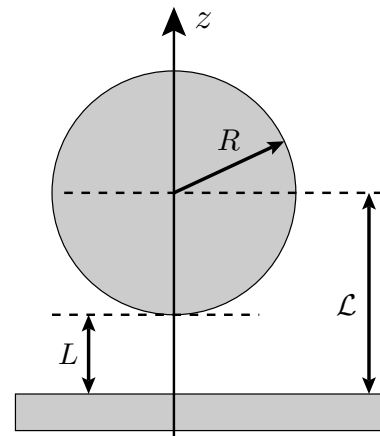


Figure 3.1: Sphere of radius R and plate separated by a distance L with center-to-plate distance $\mathcal{L} \equiv L + R$.

The validity of the PFA in the plane-sphere geometry was shown at zero temperature for a scalar field [97, 98], for perfect reflectors [48, 49], and for real metals [50]. In all cases, the scattering formula was evaluated using suitable asymptotic expansions for various special functions. In the limit of high temperatures, the Casimir energy for Drude metals was derived analytically using bispherical multipoles, and the leading order term of the PFA coincides with the leading order term of the exact result [51]. Recently, a similar derivation showed that also for perfect reflectors the leading order is in agreement with the PFA in the high temperature limit [52]. Despite all those results, the validity of the PFA in the plane-sphere geometry has not been shown in general for the plane-sphere geometry.

The connection between the PFA and the scattering approach was first studied in the context of roughness corrections. The second-order roughness correction to the Casimir energy for two parallel metallic mirrors was derived as a small perturbation of the ideal

plane-plane geometry [99]. The obtained correction coincides with the result predicted by the PFA in the limit of short separations and very smooth surfaces [99]. This line of reasoning was then generalized to the derivative expansion approach [100]. Using the derivative expansion approach, the PFA result was obtained for a curved surface in front of a plane [53]. The derivative expansion assumes that the curved surface can be obtained by a continuous deformation of a plane. Since this condition is not met for compact objects like spheres, this derivation does not constitute a proof of the PFA in the plane-sphere geometry. Nevertheless, the leading order correction to the PFA has been derived analytically from the derivative expansion for perfect reflectors at zero temperature [101], and numerically for gold metals at room temperature [102].

In this chapter, we first give the standard derivation of the PFA known in the literature. While this derivation is certainly intuitive, it is heuristic and does not constitute a proof of the validity of the approximation. In the subsequent sections, we show that the PFA yields the correct leading order term in the limit of small separations, $L \ll R$. We derive the exact matrix elements of the round-trip operator in the plane-wave basis and express the Mie scattering amplitudes by means of the Debye expansion [103]. In the PFA regime, only the direct reflection term in the Debye expansion contributes. We treat this contribution in the semiclassical WKB approximation, which has the physical interpretation of specular reflection at the surface of the sphere [104]. The condition of specular reflection makes the integration range for the conjugate momentum variable increasingly narrow as the distance between the sphere and the plate becomes small compared to the radius of the sphere. This allows us to obtain the PFA result from a saddle-point approximation of the scattering formula.

Our semiclassical derivation in the momentum representation is different from semiclassical treatments in the position space [105–107]. As the relevant surface area increases when the separation decreases [106], the standard Gutzwiller trace formula fails badly in the PFA regime. Therefore, the PFA limit cannot be connected with periodic orbits obtained from a stationary-phase approximation in the position representation, because position is poorly resolved in this limit.

The derivation presented here was first worked out by the author and then generalized by B. Spreng to the geometry of two spheres [108]. Even though the sphere-sphere geometry contains the plane-sphere geometry as a limit, we restrict ourselves to the plane-sphere geometry here. While the plane-sphere geometry is experimentally the most important geometry, recent experiments have also measured the Casimir interaction for two spheres [35, 44].

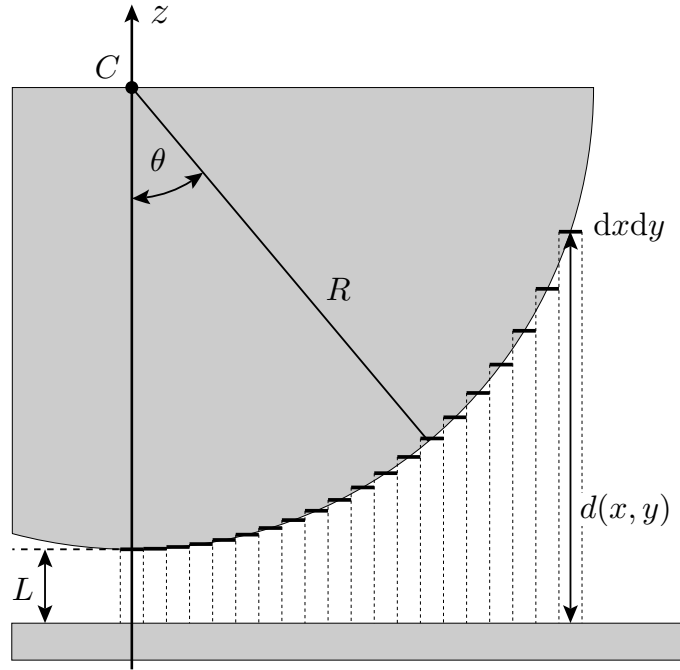


Figure 3.2: The proximity force approximation assumes that the sphere can be divided into infinitesimal small area elements which yield independent contributions to the free energy. The contributions are added up according to the Lifshitz formula (2.73) for parallel planes. The point C denotes the center of the sphere.

3.1 Heuristic derivation of the proximity force approximation

Here, we follow the heuristic derivation of the PFA given in Ref. [20]. We consider the Casimir interaction of two objects that can be separated by the x - y plane. The surface of the upper object may be described by $z_1 = z_1(x, y)$, and the surface of the lower object by $z_2 = z_2(x, y)$, respectively. The separation is then given by

$$d(x, y) \equiv z_1(x, y) - z_2(x, y) > 0. \quad (3.1)$$

The function $d(x, y)$ is strictly positive in the domain where it is defined. In the plane-sphere geometry $d(x, y)$ is only defined for $x^2 + y^2 \leq R^2$. By replacing the infinitesimal surface elements dS_1 at $z_1(x, y)$ and dS_2 at $z_2(x, y)$ by parallel surface elements $dx dy$, the unknown interaction energy can be expressed in terms of the well-known energy of the plane-plane geometry (2.73). Doing so, the Casimir free energy for arbitrary geometries can be obtained by averaging the local energy density \mathcal{F}_{PP}/A of the plane-plane geometry over the local distance $d(x, y)$

$$\mathcal{F}_{\text{PFA}} = \int_{\Sigma} dx dy \frac{\mathcal{F}_{PP}(d(x, y))}{A}. \quad (3.2)$$

Here, Σ denotes the area of the x - y plane where $d(x, y)$ is defined. The idea of the PFA for the plane-sphere geometry is sketched in Fig. 3.2.

In the case of the plane-sphere geometry, the separation is given by

$$d(x, y) = L + R - \sqrt{R^2 - x^2 - y^2} = L + R(1 - \cos \theta), \quad (3.3)$$

and the integration can be carried out in spherical coordinates

$$\mathcal{F}_{\text{PFA}} = \int_0^{2\pi} d\varphi \int_0^{\pi/2} d\theta R^2 \sin \theta \frac{\mathcal{F}_{\text{PP}}(L + R(1 - \cos \theta))}{A}. \quad (3.4)$$

The integration over φ yields a factor of 2π , and for the integration over θ we employ the substitution $u = L + R(1 - \cos \theta)$. The free energy in the plane-sphere geometry is then given by

$$\mathcal{F}_{\text{PFA}} = 2\pi R \int_L^{L+R} du \frac{\mathcal{F}_{\text{PP}}(u)}{A} \simeq 2\pi R \int_L^R du \frac{\mathcal{F}_{\text{PP}}(u)}{A}. \quad (3.5)$$

Here, the upper integration limit was set to R which is valid in the limit $R \gg L$ where the PFA is assumed to hold. By taking the negative derivative of the free energy with respect to the separation L , the Casimir force is given by

$$F_{\text{PFA}} = -\frac{\partial \mathcal{F}_{\text{PFA}}}{\partial L} = 2\pi R \frac{\mathcal{F}_{\text{PP}}(L)}{A}. \quad (3.6)$$

Therefore, the PFA connects the Casimir force in the plane-sphere geometry with the Casimir energy in the plane-plane geometry. We also note that the choice of the infinitesimal surfaces is not unique and different choices may yield different expressions for the PFA. However, the leading divergence is independent of the specific choice. The expressions for the energy (3.5) and for the force (3.6) are the most common ones found in the literature.

The evaluation of the Casimir interaction using the PFA is considerably simpler than within the scattering approach. However, the PFA neglects intrinsic properties of the plane-sphere geometry. It only considers the half of the sphere facing the plane. In fact, replacing the sphere by a half-sphere does not change the Casimir force within the proximity force approximation. Hence, resonances inside the sphere or along the surface of the sphere are not treated correctly by the approximation. By replacing the sphere by small parallel planes, the PFA ignores the finite curvature of the sphere. The curvature, however, changes the way electromagnetic waves are scattered. In addition, like van der Waals forces [109], the Casimir interaction is non-additive [28]. Moreover, while the TE and TM polarizations are in general coupled in the plane-sphere geometry, both polarizations are decoupled within the PFA and yield independent contributions.

3.2 Casimir free energy in the plane-wave basis

In the scattering approach to the Casimir effect, the free energy

$$\mathcal{F} = \frac{k_B T}{2} \sum_{n=-\infty}^{\infty} \text{tr} \log [\mathbb{1} - \mathcal{M}(|\xi_n|)] \quad (3.7)$$

is expressed as a sum over the Matsubara frequencies $\xi_n = 2\pi n k_B T / \hbar$. The round-trip operator

$$\mathcal{M} = \mathcal{R}_S \mathcal{T}_{SP} \mathcal{R}_P \mathcal{T}_{PS} \quad (3.8)$$

describes a complete round trip of an electromagnetic wave between the sphere and the plane. Here, \mathcal{R}_S denotes the reflection operator at the sphere, and \mathcal{R}_P the reflection operator at the plane. The operator $\mathcal{T}_{SP} \equiv \mathcal{T}(\mathcal{L})$ describes the translation from the reference frame of the plane to the reference frame of the sphere, and $\mathcal{T}_{PS} \equiv \mathcal{T}(-\mathcal{L})$ the translation from the sphere to the plane.

The translation operators and the reflection operator at the plane in (3.8) are diagonal in the plane-wave basis. Thus, the matrix elements of the round-trip operator in the plane-wave basis read

$$\langle \mathbf{k}_i, p_i, + | \mathcal{M} | \mathbf{k}_j, p_j, - \rangle = r_{p_j} e^{-2\kappa_j \mathcal{L}} \langle \mathbf{k}_i, p_i, - | \mathcal{R}_S | \mathbf{k}_j, p_j, + \rangle. \quad (3.9)$$

As a quick reminder, $\mathbf{k} = (K_x, K_y, 0)$ denotes the projection of the wave vector \mathbf{K} onto the x - y plane, and the dispersion relation for imaginary frequencies ξ reads $\xi^2/c^2 = \mathbf{k}^2 + \kappa^2$, cf. section 2.2. The logarithm in (3.7) can be expanded in a Mercator series

$$\mathcal{F} = -\frac{k_B T}{2} \sum_{n=-\infty}^{\infty} \sum_{r=1}^{\infty} \frac{1}{r} \text{tr} \mathcal{M}^r(|\xi_n|) \quad (3.10)$$

and the trace of the r th power of the round-trip operator is given by

$$\text{tr} \mathcal{M}^r = \sum_{p_1, \dots, p_r} \int \frac{d\mathbf{k}_1 \dots d\mathbf{k}_r}{(2\pi)^{2r}} \prod_{j=1}^r r_{p_j} e^{-2\kappa_j \mathcal{L}} \langle \mathbf{k}_j, p_j, - | \mathcal{R}_S | \mathbf{k}_{j+1}, p_{j+1}, + \rangle. \quad (3.11)$$

Here, we have used the convention of cyclic indices $p_{r+1} \equiv p_1$ and $\mathbf{k}_{r+1} \equiv \mathbf{k}_1$. The expression (3.11) has the natural interpretation of an expansion in round trips. The free energy consists of contributions from a single round trip within the cavity of the plane and the sphere, up to infinitely large numbers of round trips.

From a mathematical point of view the round-trip operator \mathcal{M} is a trace-class operator and $\det(\mathbb{1} - \mathcal{M})$ is a Fredholm determinant. The expansion in round trips corresponds to one of the definitions of the Fredholm determinant [110].

3.3 Scattering at a sphere

The matrix elements of the reflection operator \mathcal{R}_S at a sphere are derived in appendix C and given by [108]

$$\langle \mathbf{k}_j, \text{TM}, - | \mathcal{R}_S | \mathbf{k}_i, \text{TM}, + \rangle = \frac{2\pi c}{\xi \kappa_j} [A S_2(\Theta) + B S_1(\Theta)], \quad (3.12a)$$

$$\langle \mathbf{k}_j, \text{TE}, - | \mathcal{R}_S | \mathbf{k}_i, \text{TE}, + \rangle = \frac{2\pi c}{\xi \kappa_j} [A S_1(\Theta) + B S_2(\Theta)], \quad (3.12b)$$

$$\langle \mathbf{k}_j, \text{TM}, - | \mathcal{R}_S | \mathbf{k}_i, \text{TE}, + \rangle = -\frac{2\pi c}{\xi \kappa_j} [C S_1(\Theta) + D S_2(\Theta)], \quad (3.12c)$$

$$\langle \mathbf{k}_j, \text{TE}, - | \mathcal{R}_S | \mathbf{k}_i, \text{TM}, + \rangle = \frac{2\pi c}{\xi \kappa_j} [C S_2(\Theta) + D S_1(\Theta)]. \quad (3.12d)$$

The prefactor results from the normalization within the angular spectral representation introduced in section 2.2. The Mie scattering amplitudes for polarizations perpendicular and parallel to the scattering plane are given by [111]

$$S_1(\Theta) = \sum_{\ell=1}^{\infty} \frac{2\ell+1}{\ell(\ell+1)} [a_\ell \pi_\ell(\cos \Theta) + b_\ell \tau_\ell(\cos \Theta)], \quad (3.13a)$$

$$S_2(\Theta) = \sum_{\ell=1}^{\infty} \frac{2\ell+1}{\ell(\ell+1)} [a_\ell \tau_\ell(\cos \Theta) + b_\ell \pi_\ell(\cos \Theta)]. \quad (3.13b)$$

The scattering angle Θ is defined relative to the forward direction, cf. Fig. 3.3. For imaginary frequency, Θ is given by

$$\cos \Theta = -\frac{c^2}{\xi^2} (\mathbf{k}_i \cdot \mathbf{k}_j + \kappa_i \kappa_j). \quad (3.14)$$

The functions π_ℓ and τ_ℓ in (3.13) correspond to the angular functions [111]

$$\pi_\ell(z) = P'_\ell(z), \quad (3.15a)$$

$$\tau_\ell(z) = (z^2 - 1)P''_\ell(z) + zP'_\ell(z), \quad (3.15b)$$

with the Legendre polynomials P_ℓ and the prime denoting a derivative with respect to the argument z .

The coefficients A , B , C , and D in (3.12) are functions of \mathbf{k}_i and \mathbf{k}_j . Explicit expressions are given in (C.5). The Mie coefficients a_ℓ and b_ℓ [111] represent the partial wave electric and magnetic multipole scattering amplitudes, respectively, for an isotropic sphere. Like the Fresnel coefficients, they depend on the electromagnetic response of the sphere material. For simplicity, we restrict ourselves to non-magnetic materials.

3.4 The WKB approximation

In order to obtain the PFA in the limit of small separations $L \ll R$, we express the scattering amplitudes S_1 and S_2 by means of the Debye expansion [104]. This corresponds to a decomposition into an infinite series of terms representing multiple internal reflections. In the limit of large R , the main contribution comes from the direct reflection term in the Debye expansion since the phase factor acquired by propagation inside the sphere yields exponentially small terms when considering the imaginary frequency domain.

For real frequencies and large size parameters $\omega R/c \gg 1$, the asymptotic expression for the direct reflection term has been derived from the WKB approximations for the Mie coefficients and angular functions by taking the saddle point approximation for the integral over angular momenta [103]. The resulting expression is valid for all scattering directions except near the forward one, which is not relevant for the Casimir interaction. Instead of real frequencies, we need the asymptotics for imaginary frequencies ξ . A very similar WKB approximation derivation shows that the expression for imaginary frequencies coincides with the one obtained for real frequencies ω after replacing $\omega \rightarrow i\xi$. The leading asymptotics of the scattering amplitude is then given by

$$S_p(\Theta) \simeq \frac{\xi R}{2c} r_p((\pi - \Theta)/2) e^{2(\xi R/c) \sin(\Theta/2)} \quad (3.16)$$

with $p = 1, 2$ corresponding to TE and TM modes, respectively. Here, r_{TE} and r_{TM} are the Fresnel coefficients given in (2.41). The symbol \simeq indicates that the ratio of the left and right hand side of (3.16) tends to 1 in the limit $\xi R/c \rightarrow \infty$.

The asymptotics of the scattering amplitudes can be understood in terms of geometrical optics in the real frequency domain [112]. For a given scattering angle Θ , the main contribution to S_1 and S_2 in (3.13) comes from the neighborhood of the angular momentum value $\ell = (\omega R/c) \cos(\Theta/2)$ [112]. In the semiclassical approximation, the localization principle [104] connects waves with angular momentum $\ell \gg 1$ to localized rays defining an impact parameter $b = (c/\omega)\ell$. Thus, the derivation of the WKB approximation (3.16) defines rays corresponding to the impact parameter $b = R \cos(\Theta/2)$ shown in Fig. 3.3. Such rays hit the sphere surface with an incidence angle of $(\pi - \Theta)/2$. This is precisely the value required in order to obtain the scattering angle Θ from the condition of specular reflection at the tangent plane indicated in the figure. Comparing the reflection at the tangent plane (thick lines) and at the sphere with its center as reference point, one finds a difference in path length amounting to $2(\omega R/c) \sin(\Theta/2)$. In this way, the last two factors in (3.16) find their natural explanation. The first factor is responsible for providing the correct scattering cross section proportional to R^2 .

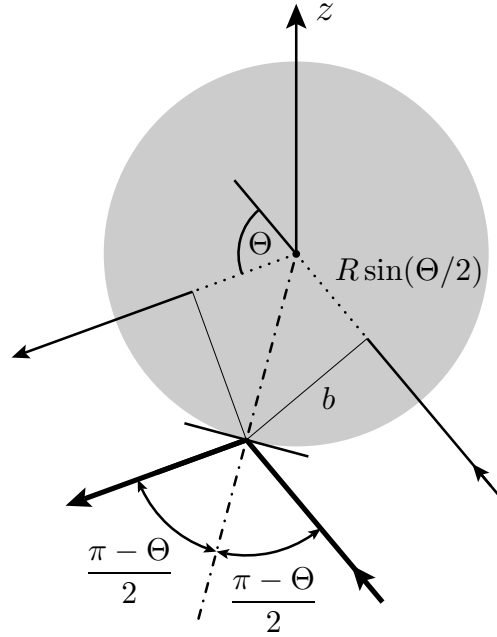


Figure 3.3: The limit of geometrical optics for the reflection at a sphere with radius R . Within the WKB approximation, a given scattering angle Θ defines the impact parameter $b = R \cos(\Theta/2)$. Seen from the tangent plane to the sphere, the angle of incidence is given by $(\pi - \Theta)/2$. The missing phase of a ray with frequency ω reflected at the sphere's surface with respect to a corresponding ray passing via the sphere's center before being deflected amounts to $(2\omega R/c) \sin(\Theta/2)$. (from [108])

In order to derive the leading asymptotic expression for the scattering matrix elements (3.12), we make use of (3.16) to obtain

$$\langle \mathbf{k}_j, p_j, - | \mathcal{R}_S | \mathbf{k}_i, p_i, + \rangle \simeq \frac{\pi R}{\kappa_j} e^{2(\xi R/c) \sin(\Theta/2)} \rho_{p_j, p_i} \quad (3.17)$$

with

$$\rho_{\text{TM}, \text{TM}} = Ar_{\text{TM}} + Br_{\text{TE}}, \quad (3.18a)$$

$$\rho_{\text{TE}, \text{TE}} = Ar_{\text{TE}} + Br_{\text{TM}}, \quad (3.18b)$$

$$\rho_{\text{TM}, \text{TE}} = -Cr_{\text{TE}} - Dr_{\text{TM}}, \quad (3.18c)$$

$$\rho_{\text{TE}, \text{TM}} = Cr_{\text{TM}} + Dr_{\text{TE}}. \quad (3.18d)$$

3.5 Saddle-point approximation

We now turn to the derivation of the PFA using the matrix elements (3.17) obtained within the WKB approximation. The central object in the expression (3.10) for the free energy is the trace over \mathcal{M}^r which is a $2r$ dimensional integral. In the limit that the sphere is much larger than the separation between the sphere and the plane, $R \gg L$, the integral can be

evaluated by means of the saddle point approximation

$$\int d^D \mathbf{x} g(\mathbf{x}) e^{-Rf(\mathbf{x})} \simeq \left(\frac{2\pi}{R} \right)^{D/2} \frac{g(\mathbf{x}_{\text{S.P.}})}{\sqrt{\det \mathbf{H}(\mathbf{x}_{\text{S.P.}})}} e^{-Rf(\mathbf{x}_{\text{S.P.}})}. \quad (3.19)$$

Here, D denotes the dimension, R is a big parameter, $\mathbf{x}_{\text{S.P.}}$ is the stationary point of $f(\mathbf{x})$, and \mathbf{H} corresponds to the Hessian of f . In the following, we will express the trace over \mathcal{M}^r in the form (3.19). The trace can then be evaluated after determining the stationary point of f and computing the determinant of the Hessian \mathbf{H} evaluated at the saddle point.

3.5.1 Saddle point manifold

We insert the WKB matrix elements corresponding to the scattering at the sphere (3.17) into the matrix elements of the round-trip operator (3.9). In polar coordinates after changing the integration variables k_j to κ_j , we obtain the expression

$$\text{tr } \mathcal{M}^r \simeq \int_{|\xi_n|/c}^{\infty} d\kappa_1 \dots d\kappa_r \int_0^{2\pi} d\varphi_1 \dots d\varphi_r g(\mathbf{k}_1, \dots, \mathbf{k}_r) e^{-Rf(\mathbf{k}_1, \dots, \mathbf{k}_r)} \quad (3.20)$$

which has a suitable form for an evaluation using the saddle-point approximation (3.19). Here, we have introduced the function

$$g(\mathbf{k}_1, \dots, \mathbf{k}_r) = \left(\frac{R}{4\pi} \right)^r \sum_{p_1, \dots, p_r} \prod_{j=1}^r r_{p_j} \rho_{p_j, p_{j+1}} e^{-2\kappa_j L}, \quad (3.21)$$

and the function in the exponent of (3.20) is given by

$$f(\mathbf{k}_1, \dots, \mathbf{k}_r) = \sum_{j=1}^r \left(2\kappa_j - \sqrt{2 \left[(\xi/c)^2 + \kappa_j \kappa_{j+1} + k_j k_{j+1} \cos(\varphi_j - \varphi_{j+1}) \right]} \right). \quad (3.22)$$

In order to evaluate the $2r$ integrals in (3.20) within the saddle-point approximation, we need to determine the stationary points of f . The derivative of f with respect to φ_j

$$\begin{aligned} \frac{\partial f}{\partial \varphi_j} = & - \frac{k_{j-1} k_j \sin(\varphi_{j-1} - \varphi_j)}{\sqrt{2 \left[(\xi^2/c^2) + \kappa_{j-1} \kappa_j + k_{j-1} k_j \cos(\varphi_{j-1} - \varphi_j) \right]}} \\ & + \frac{k_j k_{j+1} \sin(\varphi_j - \varphi_{j+1})}{\sqrt{2 \left[(\xi^2/c^2) + \kappa_j \kappa_{j+1} + k_j k_{j+1} \cos(\varphi_j - \varphi_{j+1}) \right]}} \end{aligned} \quad (3.23)$$

vanishes if all angles $\varphi_1 = \dots = \varphi_r$ are equal. For equal angles, the derivative of f with respect to κ_j reads

$$\left. \frac{\partial f}{\partial \kappa_j} \right|_{\varphi_1 = \dots = \varphi_r} = 2 - \frac{\kappa_{j-1} + k_{j-1} \frac{\kappa_j}{k_j}}{\sqrt{2 \left[(\xi/c)^2 + \kappa_{j-1} \kappa_j + k_{j-1} k_j \right]}} - \frac{\kappa_{j+1} + k_{j+1} \frac{\kappa_j}{k_j}}{\sqrt{2 \left[(\xi/c)^2 + \kappa_j \kappa_{j+1} + k_j k_{j+1} \right]}}. \quad (3.24)$$

This derivative yields 0 for $\kappa_1 = \dots = \kappa_r$. In this case, the denominators become $2\kappa_j$ and the second and third term in (3.24) simplify to -1 . Hence, there exists a two-dimensional manifold of saddle points

$$\kappa_1 = \dots = \kappa_r \equiv \kappa_*, \quad \varphi_1 = \dots = \varphi_r \equiv \varphi_*, \quad (3.25)$$

parametrized by κ_* and φ_* . On the saddle-point manifold, the change of angle $\varphi_j - \varphi_{j+1}$ vanishes and the coefficients in (3.18) simplify to $A = 1, B = C = D = 0$, which can be verified by setting $\varphi = 0$ in (C.5). Moreover, the polarization is conserved during scattering processes within the saddle-point approximation, because $\rho_{\text{TE, TM}}$ and $\rho_{\text{TM, TE}}$ in (3.18) depend on C and D only. The two polarizations decouple and yield independent contributions to the trace over r round-trip operators

$$\text{tr } \mathcal{M}^r = \text{tr } \mathcal{M}_{\text{TE}}^r + \text{tr } \mathcal{M}_{\text{TM}}^r. \quad (3.26)$$

As the change of the Wick rotated z -component of the wave vector vanishes, $\kappa_j - \kappa_{j+1} = 0$, the projection of the wave vector onto the x - y plane is conserved during reflections, $\mathbf{k}_j - \mathbf{k}_{j+1} = 0$. Within the WKB approximation, \mathbf{k} is conserved when the tangent plane on which the reflection occurs is perpendicular to the z -axis, cf. Fig. 3.3. Therefore, the main contribution comes from a small section of the sphere around the point of closest approach. Also, at the saddle point manifold the WKB shift $2(\xi R/c) \sin(\Theta/2)$ becomes $2\kappa R$ and cancels precisely the term arising from the translation from the sphere to the plane and back. Consequently, the exponent (3.22) vanishes on the saddle point manifold,

$$f|_{\text{S.P.}} = 0. \quad (3.27)$$

For the prefactor in the integrand of (3.20) we obtain for the two polarization contributions $p = \text{TE, TM}$

$$g_p|_{\text{S.P.}}(\kappa_*) = \left(\frac{R}{4\pi} r_p^2 \right)^r e^{-2r\kappa_* L} \quad (3.28)$$

on the saddle-point manifold, and the Fresnel coefficients are evaluated with arguments $r_p = r_p(i|\xi|, k_*)$. Here, we have introduced the natural abbreviation $k_* = (\kappa_*^2 - \xi^2/c^2)^{1/2}$. On the saddle-point manifold, only a translation by L remains, which corresponds to the distance of closest approach.

3.5.2 Hessian matrix

We now evaluate the Hessian matrix \mathbf{H} corresponding to the function f (3.22) at the saddle-point manifold. The derivative of f with respect to φ_j consists of two terms, one proportional to $\sin(\varphi_{j+1} - \varphi_j)$, and the other term proportional to $\sin(\varphi_j - \varphi_{j-1})$, cf. (3.23). Accordingly, a single derivative of f with respect to φ_j evaluated at the saddle-point

manifold vanishes, and for this reason the Hessian is block-diagonal

$$\mathbf{H} = \begin{pmatrix} \mathbf{H}_{\kappa\kappa} & 0 \\ 0 & \mathbf{H}_{\varphi\varphi} \end{pmatrix}. \quad (3.29)$$

The diagonal blocks read

$$\mathbf{H}_{\kappa\kappa} = \frac{\kappa_\star}{2k_\star^2} \mathbf{A}_r, \quad \mathbf{H}_{\varphi\varphi} = \frac{k_\star^2}{2\kappa_\star} \mathbf{A}_r, \quad (3.30)$$

and, apart from prefactors, they are given by the circulant $r \times r$ matrix

$$\mathbf{A}_r = \begin{pmatrix} 2 & -1 & & & -1 \\ -1 & 2 & -1 & & \\ & -1 & \ddots & \ddots & \\ & & \ddots & \ddots & -1 \\ -1 & & & -1 & 2 \end{pmatrix}, \quad (3.31)$$

where empty entries correspond to zero matrix elements. The eigenvalues of a circulant matrix can be evaluated analytically [113], and the eigenvalues of \mathbf{A}_r are found as

$$\lambda_j = 4 \sin^2 \left(\frac{\pi j}{r} \right), \quad j = 0 \dots, r-1. \quad (3.32)$$

Both $\mathbf{H}_{\kappa\kappa}$ and $\mathbf{H}_{\varphi\varphi}$ have a zero eigenvalue corresponding to the saddle-point manifold.

3.6 Casimir free energy and force

Within the saddle-point approximation, the directions perpendicular to the saddle-point manifold can now be integrated out in the usual way, while the integration along the families has to be carried out exactly. As we will see, the integral over φ_\star can be solved analytically, so that we are left with an integral over κ_\star .

The product of all non-vanishing eigenvalues of \mathbf{A}_r yields

$$\prod_{j=1}^{r-1} \lambda_j = \prod_{j=1}^{r-1} 4 \sin^2 \left(\frac{\pi j}{r} \right) = r^2. \quad (3.33)$$

We now change to the eigenbasis of \mathbf{H} , but keep κ_\star and φ_\star as variables for the integration. This means that we do not normalize the eigenvectors corresponding to the saddle-point

manifold, which yields a factor r arising from the Jacobian. Then, applying the multi-dimensional saddle-point integration formula (3.19), we obtain

$$\text{tr } \mathcal{M}_p^r \simeq \frac{R}{4\pi r} \int_{|\xi_n|/c}^{\infty} d\kappa_* \int_0^{2\pi} d\varphi_* (r_p^2 e^{-2\kappa_* L})^r = \frac{R}{2r} \int_{|\xi_n|/c}^{\infty} d\kappa_* (r_p^2 e^{-2\kappa_* L})^r \quad (3.34)$$

for the two polarization contributions $p = \text{TE}, \text{TM}$. Inserting this result into the formula for the free energy (3.7), and evaluating the sum over the number r of round trips, we obtain

$$\mathcal{F} \simeq \mathcal{F}_{\text{PFA}} = -\frac{k_B T R}{4} \sum_{n=-\infty}^{\infty} \sum_{p=\text{TE}, \text{TM}} \int_{|\xi_n|/c}^{\infty} d\kappa_* \text{Li}_2 (r_p^2 e^{-2\kappa_* L}) . \quad (3.35)$$

Here, Li_2 denotes the dilogarithm [91, §25.12] and the Fresnel coefficients are evaluated at $r_p = r_p(i|\xi|, k_*)$.

The Casimir force is now easily obtained by taking the negative derivative of the free energy (3.35) with respect to the separation L

$$F \simeq F_{\text{PFA}} = 2\pi R \frac{\mathcal{F}_{\text{PP}}(L, T)}{A} . \quad (3.36)$$

Here, $\mathcal{F}_{\text{PP}}(L, T)/A$ denotes the free energy per area in the plane-plane geometry, cf. (2.73). This result precisely coincides with the expression obtained using the heuristic derivation given in section 3.1.

Our derivation also allows to estimate the effective area that corresponds to the dominant contribution to the Casimir interaction. This is important as precise Casimir experiments in the plane-sphere geometry typically employ spherical lenses [30] or coated microspheres attached to a cantilever beam [9, 40, 42]. The spherical cap around the point of closest distance effectively contributing to the interaction is bounded by the angle $\theta \lesssim (L/R)^{1/2} \ll 1$ [108], cf. Fig. 3.2. The effective area is then given by $A \sim RL$. The same result has been obtained in Ref. [114] using a heuristic geometric argument.

In this chapter, we have derived the proximity force approximation for the free energy as the leading asymptotic result in the limit of small separations. We have expressed the round-trip matrix in the plane-wave basis. Taking only the direct reflection term of the Debye expansion into account and using the WKB Mie scattering amplitudes, the trace over a number of round-trip operators has been evaluated within the saddle-point approximation. The main contribution to the free energy results from specular reflection in the vicinity of the points of closest distance. We have found that no polarization mixing contributes in leading order. In the next chapter, we will derive the matrix elements of the round-trip operator in the multipole basis. After discussing numerical issues in chapter 5, we will compare the PFA with numerically exact results for zero temperature in chapter 6, and for ambient temperature with real metals in chapter 7.

Chapter 4

Symmetrized round-trip operator in the plane-sphere geometry

In this chapter, we apply the scattering formula to the geometry of a sphere above a plane. In contrast to the common choice found in the literature, we adopt a symmetrized form of the round-trip operator which is a key element to push the numerics to aspect ratios $R/L \sim 10^3$ used in typical experiments. We derive the matrix elements of the round-trip operator at imaginary frequencies, simplify the expressions, and study the mathematical properties of the resulting matrix. We conclude the chapter discussing how the scattering formula can be evaluated efficiently using techniques of hierarchical matrices.

4.1 Scattering at a sphere

While the plane-wave basis is well adapted to describe the reflection at a plane, the reflection at a sphere is naturally described in the multipole basis. The basis elements $|\ell, m, P, s\rangle$ of the multipole basis are eigenstates of the total angular momentum operator L^2 and the corresponding z -component L_z with eigenvalues $\hbar^2 \ell(\ell + 1)$ and $\hbar m$, respectively ($\ell = 1, 2, 3, \dots, m = -\ell, \dots, \ell$). The polarization P denotes either electric multipole waves ($P = E$) or magnetic multipole waves ($P = M$). The last index describes the radial dependence and takes the values $s = \{\text{reg}, \text{out}\}$. For $s = \text{reg}$, the radial dependence is given in terms of the spherical Bessel function j_ℓ , which is regular in the origin. The radial dependence for outgoing modes ($s = \text{out}$) is given in terms of the spherical Hankel function $h_\ell^{(1)}$, which is divergent in the origin [115]. The basis functions can be constructed from the scalar eigenstates of L^2 and L_z [56]. Explicit expressions are given in Ref. [115].

For a homogeneous, isotropic, and non-magnetic sphere in vacuum, the reflection operator \mathcal{R}_S is diagonal in the multipole basis with matrix elements [111]

$$\mathcal{R}_S |\ell, m, P, \text{reg}\rangle = r_{\ell, P}^{(S)} |\ell, m, P, \text{out}\rangle = \begin{cases} -a_\ell |\ell, m, P, \text{out}\rangle & \text{for } P = E \\ -b_\ell |\ell, m, P, \text{out}\rangle & \text{for } P = M \end{cases} \quad (4.1)$$

given in terms of the Mie coefficients a_ℓ and b_ℓ . The superscript (S) indicates that $r_{\ell,P}^{(S)}$ corresponds to the reflection coefficient at the sphere. The minus sign in (4.1) is a consequence of the definition of the Mie coefficients in Ref. [111].

For imaginary frequencies, the Mie coefficients are given by [116, 117]

$$a_\ell(ix) = (-1)^\ell \frac{\pi n^2 s_\ell^{(a)} - s_\ell^{(b)}}{2 n^2 s_\ell^{(c)} + s_\ell^{(d)}}, \quad (4.2a)$$

$$b_\ell(ix) = (-1)^{\ell+1} \frac{\pi s_\ell^{(b)} - s_\ell^{(a)}}{2 s_\ell^{(c)} + s_\ell^{(d)}}, \quad (4.2b)$$

where

$$s_\ell^{(a)}(x) = I_{\ell+\frac{1}{2}}(nx) \left[x I_{\ell-\frac{1}{2}}(x) - \ell I_{\ell+\frac{1}{2}}(x) \right], \quad (4.3a)$$

$$s_\ell^{(b)}(x) = I_{\ell+\frac{1}{2}}(x) \left[nx I_{\ell-\frac{1}{2}}(nx) - \ell I_{\ell+\frac{1}{2}}(nx) \right], \quad (4.3b)$$

$$s_\ell^{(c)}(x) = I_{\ell+\frac{1}{2}}(nx) \left[x K_{\ell-\frac{1}{2}}(x) + \ell K_{\ell+\frac{1}{2}}(x) \right], \quad (4.3c)$$

$$s_\ell^{(d)}(x) = K_{\ell+\frac{1}{2}}(x) \left[nx I_{\ell-\frac{1}{2}}(nx) - \ell I_{\ell+\frac{1}{2}}(nx) \right]. \quad (4.3d)$$

Here, $n = \sqrt{\varepsilon(i\xi)}$ denotes the refractive index, and the Mie coefficients are evaluated at the size parameter $x = \xi R/c$, where R is the radius of the sphere and ξ the imaginary frequency. The functions $I_\nu(x)$ and $K_\nu(x)$ denote the modified Bessel functions of the first and the second kind, respectively. As shown in appendix B.1, the coefficients $s_\ell^{(a)}$, $s_\ell^{(b)}$, $s_\ell^{(c)}$, $s_\ell^{(d)}$, and the numerators in (4.2) are positive. Therefore, the signs of the Mie coefficients are $(-1)^\ell$ for a_ℓ and $(-1)^{\ell+1}$ for b_ℓ , respectively.

For perfect reflectors the Mie coefficients become

$$a_\ell^{\text{PR}}(ix) = (-1)^\ell \frac{\pi x I_{\ell-1/2}(x) - \ell I_{\ell+1/2}(x)}{2 x K_{\ell-1/2}(x) + \ell K_{\ell+1/2}(x)}, \quad (4.4a)$$

$$b_\ell^{\text{PR}}(ix) = (-1)^{\ell+1} \frac{\pi I_{\ell+1/2}(x)}{2 K_{\ell+1/2}(x)}. \quad (4.4b)$$

4.2 The round-trip operator

The plane-sphere geometry consists of a sphere and an infinite plane. We choose the coordinate system such that the plane coincides with the x - y plane, and the center of the sphere is located at $z = R + L$. Here, R denotes the radius of the sphere and L is the surface-to-surface distance between both objects. For convenience, we will also use the abbreviation $\mathcal{L} \equiv L + R$ for the separation between the center of the sphere and the plane. The geometry is depicted in Fig. 4.1a.

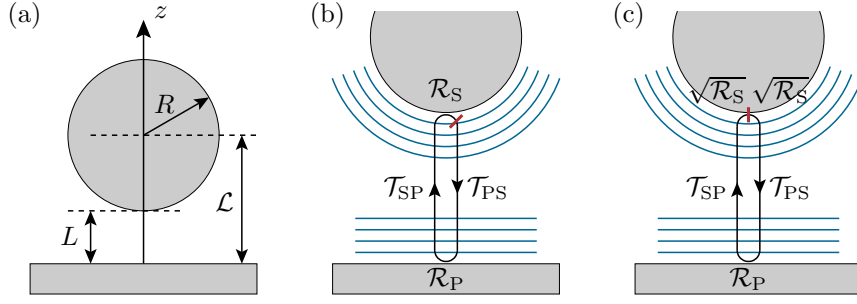


Figure 4.1: (a) Sphere of radius R and plate separated by a distance L with center-to-plate distance $\mathcal{L} \equiv L + R$. Schematic representation (b) of the round-trip operator \mathcal{M} defined in (4.6) and (c) the symmetrized round-trip operator $\widehat{\mathcal{M}}$ defined in (4.8).

The Casimir free interaction energy is given as a sum [23–25]

$$\mathcal{F} = \frac{k_B T}{2} \sum_{n=-\infty}^{\infty} \log \det [\mathbb{1} - \mathcal{M}(|\xi_n|)] \quad (4.5)$$

over the Matsubara frequencies $\xi_n = 2\pi n k_B T / \hbar$. In the plane-sphere geometry, the free energy depends on the separation L of the sphere and the plane, the radius R of the sphere, the temperature T , and the optical properties of the sphere and the plate. The round-trip operator

$$\mathcal{M} = \mathcal{R}_S \mathcal{T}_{SP} \mathcal{R}_P \mathcal{T}_{PS} \quad (4.6)$$

consists of the reflection operator at the sphere \mathcal{R}_S , the reflection operator at the plane \mathcal{R}_P , the translation operator from sphere to plane $\mathcal{T}_{PS} \equiv \mathcal{T}(-\mathcal{L})$, and the translation operator from plane to sphere $\mathcal{T}_{SP} \equiv \mathcal{T}(\mathcal{L})$. The round trip starts with a translation from the sphere to the plane, a reflection at the plane, a translation back to the sphere, and a reflection at the sphere. In Fig. 4.1b, we sketch the round trip corresponding to \mathcal{M} . Due to the rotational symmetry about the z -axis, the round-trip operator is block diagonal with respect to m

$$\mathcal{M} = \begin{pmatrix} \ddots & & & & & \\ & \mathcal{M}^{-1} & & & & \\ & & \mathcal{M}^0 & & & \\ & & & \mathcal{M}^1 & & \\ & & & & \ddots & \end{pmatrix}, \quad (4.7)$$

and every block \mathcal{M}^m yields an independent contribution to the free energy. Here, \mathcal{M}^m denotes a block corresponding to a given subspace m and should not be confused with a matrix power.

The definition (4.6) of the round-trip operator \mathcal{M} results in ill-conditioned matrices. In Fig. 4.2a, we depict the values of the matrix elements $\mathcal{M}_{\ell_1 \ell_2}^m = \langle \ell_1, m, P_1 | \mathcal{M} | \ell_2, m, P_2 \rangle$ on a logarithmic color scale. Even though the matrix elements depend on the chosen

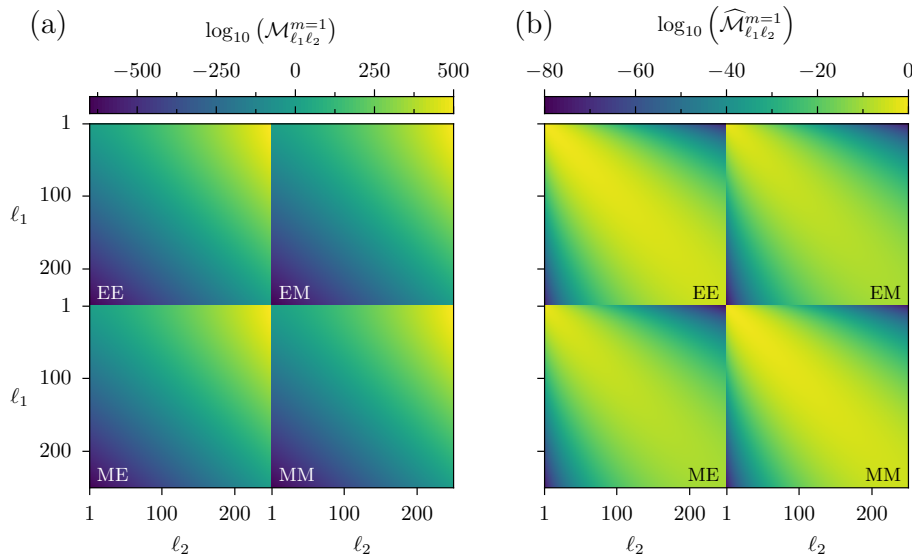


Figure 4.2: The logarithm of the matrix elements for (a) the non-symmetrized round-trip operator \mathcal{M}^m and (b) the symmetrized round-trip operator $\widehat{\mathcal{M}}^m$ in the multipole basis is shown on a logarithmic color scale for $R/L = 50$, $\xi(L+R)/c = 1$, $m = 1$, and perfect reflectors. The four blocks correspond to the different sequences of polarizations during a round trip. While the non-symmetrized round-trip matrix is ill-conditioned, the matrix elements of the symmetrized round-trip operator take their maximum on the diagonal of each polarization block and decrease away from it.

parameters, the data shown are typical. Already for the relatively small aspect ratio $R/L = 50$ used in Fig. 4.2a, the round-trip operator (4.6) clearly results in an ill-conditioned matrix with elements differing by hundreds of orders of magnitude. As a consequence, a fast and stable numerical evaluation of the determinant becomes extremely difficult. When evaluating the determinants in (4.5), the combination of very small and very large matrix elements may yield contributions of the order one. Small perturbations in the matrix elements may then cause large errors. Furthermore, common computer number formats cover a range of numbers from about 10^{-323} to 10^{308} [118] which is insufficient to represent all matrix elements in Fig. 4.2a. Instead, one has to use number formats that cover a wider range of numbers, but are also significantly slower.

To overcome these problems, we make use of the fact that the round-trip operator is only unique up to cyclic permutations. The free energy is invariant under such permutations which follows from Sylvester's determinant identity. In contrast to the common choice for the round-trip operator (4.6) in the literature [115, 116, 119–123], we choose the symmetrized version [29, 54]

$$\widehat{\mathcal{M}} = \sqrt{\mathcal{R}_S} \mathcal{T}_{SP} \mathcal{R}_P \mathcal{T}_{PS} \sqrt{\mathcal{R}_S}, \quad (4.8)$$

as illustrated in Fig. 4.1c. Since the scattering operator at the sphere \mathcal{R}_S is diagonal in the multipole basis, the matrix square root of \mathcal{R}_S can be computed readily. With this choice for the round-trip operator, the matrix elements take their maximum on the diagonal of each polarization block and decrease away from it, as can be seen in Fig. 4.2b. Here, the

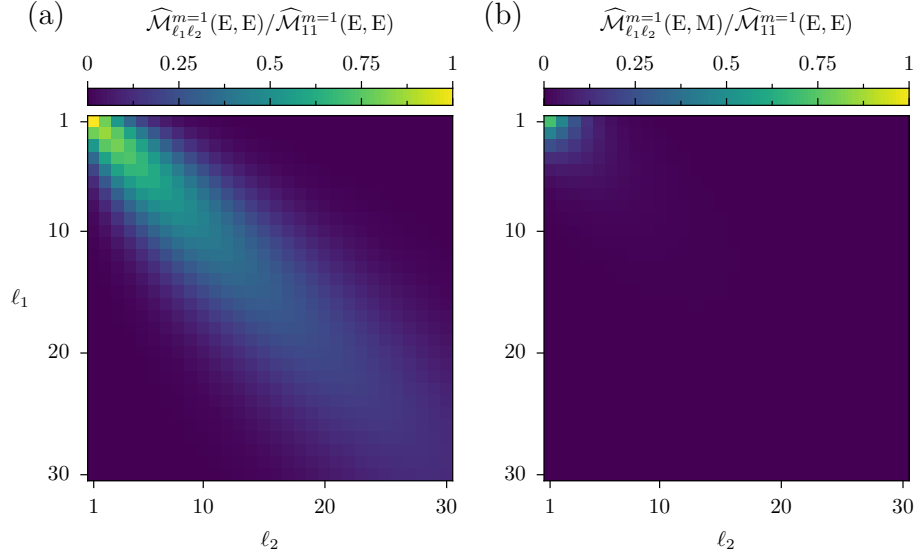


Figure 4.3: Details of the matrix elements for (a) the polarization maintaining block (E, E) and (b) the polarization mixing block (E, M) are shown for the same parameters as in Fig. 4.2, but now on a linear scale. All matrix elements are taken with respect to the largest matrix element in the round-trip matrix.

same parameters have been used as in Fig. 4.2a.

In Fig. 4.3, we depict a polarization-conserving block (left) and a polarization-mixing block (right) with the matrix elements taken from Fig. 4.2b, but now on a linear color scale. This representation emphasizes the fact that a sizable fraction of the matrix elements is numerically irrelevant. We will exploit this property in section 4.6 using hierarchical matrices. Furthermore, the contribution due to the polarization-mixing blocks is significantly smaller than that of the polarization-conserving blocks for aspect ratios $R/L \gg 1$.

4.3 Matrix elements of the round-trip operator

We now turn to the derivation of the matrix elements of the symmetrized round-trip operator $\widehat{\mathcal{M}}$ in the multipole basis. The action of the round-trip operator on a basis element of the multipole basis is given by

$$\widehat{\mathcal{M}} |\ell, m, P, \text{reg}\rangle = \sqrt{\mathcal{R}_S} \mathcal{T}_{\text{SP}} \mathcal{R}_P \mathcal{T}_{\text{PS}} \sqrt{\mathcal{R}_S} |\ell, m, P, \text{reg}\rangle. \quad (4.9)$$

The scattering operator at the sphere is diagonal in the multipole basis and the action of $\sqrt{\mathcal{R}_S}$ on $|\ell, m, P, \text{reg}\rangle$ yields the square root of the reflection coefficient $r_{\ell, P}^{(S)}$

$$\widehat{\mathcal{M}} |\ell, m, P, \text{reg}\rangle = \sqrt{r_{\ell, P}^{(S)}} \sqrt{\mathcal{R}_S} \mathcal{T}_{\text{SP}} \mathcal{R}_P \mathcal{T}_{\text{PS}} |\ell, m, P, \text{out}\rangle. \quad (4.10)$$

Inserting the resolution of the identity in the plane-wave basis

$$\mathbb{1} = \sum_{\phi=\pm} \sum_{p=\text{TE, TM}} \int_0^\infty \frac{d^2\mathbf{k}}{(2\pi)^2} |\mathbf{k}, p, \phi\rangle \langle \mathbf{k}, p, \phi|, \quad (4.11)$$

we can evaluate the translation operators and the reflection operator at the plane. The translation operators each yield a factor $e^{-\kappa\mathcal{L}}$, and the reflection at the plane introduces a Fresnel coefficient. Therefore, (4.10) becomes

$$\widehat{\mathcal{M}} |\ell, m, P, \text{reg}\rangle = \sqrt{r_{\ell, P}^{(S)}} \sum_{p=\text{TE, TM}} \int \frac{d^2\mathbf{k}}{(2\pi)^2} r_p^{(P)} e^{-2\kappa\mathcal{L}} \sqrt{\mathcal{R}_S} |\mathbf{k}, p, +\rangle \langle \mathbf{k}, p, -|\ell, m, P, \text{out}\rangle, \quad (4.12)$$

where we have denoted the Fresnel coefficients with a superscript (P) to avoid confusion with the reflection coefficient $r_{\ell, P}^{(S)}$ at the sphere. Inserting the resolution of the identity in the multipole basis

$$\mathbb{1} = \sum_{\ell=1}^{\infty} \sum_{m=-\ell}^{\ell} \sum_{P=\text{E, M}} \sum_{s=\text{reg, out}} |\ell, m, P, s\rangle \langle \ell, m, P, s| \quad (4.13)$$

and projecting the result on an element of the multipole basis, the matrix elements of the round-trip operator read

$$\begin{aligned} \langle \ell_1, m, P_1, \text{reg} | \widehat{\mathcal{M}} | \ell_2, m, P_2, \text{reg} \rangle &= \sqrt{r_{\ell_1, P_1}^{(S)}} \sqrt{r_{\ell_2, P_2}^{(S)}} \sum_{p=\text{TE, TM}} \int \frac{d^2\mathbf{k}}{(2\pi)^2} r_p^{(P)} e^{-2\kappa\mathcal{L}} \\ &\times \langle \ell_1, m, P_1, \text{reg} | \mathbf{k}, p, + \rangle \langle \mathbf{k}, p, - | \ell_2, m, P_2, \text{out} \rangle. \end{aligned} \quad (4.14)$$

Explicit expressions for the matrix elements implementing the change from the multipole to the plane-wave basis have been derived in Ref. [115] and are given in appendix D for convenience.

We organize the round-trip matrix in the form of a block matrix

$$\widehat{\mathcal{M}}^m = \begin{pmatrix} \widehat{\mathcal{M}}^m(\text{E}, \text{E}) & \widehat{\mathcal{M}}^m(\text{E}, \text{M}) \\ \widehat{\mathcal{M}}^m(\text{M}, \text{E}) & \widehat{\mathcal{M}}^m(\text{M}, \text{M}) \end{pmatrix} \quad (4.15)$$

where the diagonal blocks correspond to matrix elements preserving polarization, and the off-diagonal blocks represent matrix elements with a change of polarization. Expressing the double integral in (4.14) in polar coordinates, the integral over the polar angle yields 2π . After a similarity transform of the round-trip matrix in order to remove phase factors,

we obtain the matrix elements

$$\widehat{\mathcal{M}}_{\ell_1 \ell_2}^m(M, M) = \Lambda_{\ell_1 \ell_2}^m \sqrt{|b_{\ell_1} b_{\ell_2}|} (A_{\ell_1 \ell_2, \text{TM}}^m - B_{\ell_1 \ell_2, \text{TE}}^m), \quad (4.16a)$$

$$\widehat{\mathcal{M}}_{\ell_1 \ell_2}^m(E, E) = \Lambda_{\ell_1 \ell_2}^m \sqrt{|a_{\ell_1} a_{\ell_2}|} (B_{\ell_1 \ell_2, \text{TM}}^m - A_{\ell_1 \ell_2, \text{TE}}^m), \quad (4.16b)$$

$$\widehat{\mathcal{M}}_{\ell_1 \ell_2}^m(M, E) = \Lambda_{\ell_1 \ell_2}^m \sqrt{|b_{\ell_1} a_{\ell_2}|} (C_{\ell_1 \ell_2, \text{TM}}^m - C_{\ell_2 \ell_1, \text{TE}}^m), \quad (4.16c)$$

$$\widehat{\mathcal{M}}_{\ell_1 \ell_2}^m(E, M) = \Lambda_{\ell_1 \ell_2}^m \sqrt{|a_{\ell_1} b_{\ell_2}|} (C_{\ell_2 \ell_1, \text{TM}}^m - C_{\ell_1 \ell_2, \text{TE}}^m), \quad (4.16d)$$

which depend on the integrals

$$A_{\ell_1 \ell_2, p}^m = \frac{m^2 \xi}{c} \int_0^\infty dk \frac{1}{k \kappa} r_p(i\xi, k) e^{-2\kappa \mathcal{L}} P_{\ell_1}^m\left(\frac{\kappa c}{\xi}\right) P_{\ell_2}^m\left(\frac{\kappa c}{\xi}\right), \quad (4.17a)$$

$$B_{\ell_1 \ell_2, p}^m = \frac{c^3}{\xi^3} \int_0^\infty dk \frac{k^3}{\kappa} r_p(i\xi, k) e^{-2\kappa \mathcal{L}} P_{\ell_1}^{m'}\left(\frac{\kappa c}{\xi}\right) P_{\ell_2}^{m'}\left(\frac{\kappa c}{\xi}\right), \quad (4.17b)$$

$$C_{\ell_1 \ell_2, p}^m = \frac{m c}{\xi} \int_0^\infty dk \frac{k}{\kappa} r_p(i\xi, k) e^{-2\kappa \mathcal{L}} P_{\ell_1}^m\left(\frac{\kappa c}{\xi}\right) P_{\ell_2}^{m'}\left(\frac{\kappa c}{\xi}\right). \quad (4.17c)$$

Here, we have dropped the superscript (P) of the Fresnel coefficients to simplify the notation. The Legendre polynomials $P_\ell^m(x)$ are evaluated at arguments $x \geq 1$. It is convenient to use the phase convention defined in appendix A.2. The associated Legendre polynomials are then real and non-negative functions for $x \geq 1$. The normalizing coefficient $\Lambda_{\ell_1 \ell_2}^m$ is defined as

$$\Lambda_{\ell_1 \ell_2}^m = \frac{2N_{\ell_1}^m N_{\ell_2}^m}{\sqrt{\ell_1(\ell_1+1)} \sqrt{\ell_2(\ell_2+1)}} = \sqrt{\frac{(2\ell_1+1)(2\ell_2+1)(\ell_1-m)!(\ell_2-m)!}{\ell_1(\ell_1+1)\ell_2(\ell_2+1)(\ell_1+m)!(\ell_2+m)!}}, \quad (4.18)$$

where N_ℓ^m corresponds to the normalizing coefficient of the spherical harmonics as defined in (A.2).

The matrix elements of the round-trip operator \mathcal{M} differ from those of the symmetrized round-trip operator $\widehat{\mathcal{M}}$ only with respect to the Mie coefficients. While for the symmetrized round-trip operator $\widehat{\mathcal{M}}$ according to (4.16) the matrix elements are proportional to the square root of a product of Mie coefficients with different angular momenta, the matrix elements of \mathcal{M} are proportional to one Mie coefficient with angular momentum ℓ_1 ,

$$\mathcal{M}_{\ell_1 \ell_2}^m(E, E), \mathcal{M}_{\ell_1 \ell_2}^m(E, M) \propto a_{\ell_1}, \quad (4.19a)$$

$$\mathcal{M}_{\ell_1 \ell_2}^m(M, M), \mathcal{M}_{\ell_1 \ell_2}^m(M, E) \propto b_{\ell_1}. \quad (4.19b)$$

This causes the numerical problems discussed above.

4.4 Low-frequency limit

In the low-frequency limit $\xi \rightarrow 0$, the Legendre polynomials in (4.17) diverge. In order to evaluate the scattering formula for the Matsubara frequency $\xi_0 = 0$, the limit $\xi \rightarrow 0$ for the matrix elements of $\widehat{\mathcal{M}}$ has to be calculated analytically. Using (A.11a) for the behavior of the associated Legendre polynomials $P_\ell^m(x)$ when $x \rightarrow \infty$, one finds that the integrals (4.17) for $\xi \rightarrow 0$ scale like

$$A_{\ell_1 \ell_2, p}^m(\xi) \sim r_p(i\xi, k) \xi^{-(\ell_1 + \ell_2 - 1)}, \quad (4.20a)$$

$$B_{\ell_1 \ell_2, p}^m(\xi) \sim r_p(i\xi, k) \xi^{-(\ell_1 + \ell_2 + 1)}, \quad (4.20b)$$

$$C_{\ell_1 \ell_2, p}^m(\xi) \sim r_p(i\xi, k) \xi^{-(\ell_1 + \ell_2)}. \quad (4.20c)$$

Since the contribution of $A_{\ell_1 \ell_2, p}^m$ and $C_{\ell_1 \ell_2, p}^m$ is at least by a factor ξ suppressed compared to $B_{\ell_1 \ell_2, p}^m$, it is sufficient to consider only the integral $B_{\ell_1 \ell_2, p}^m$. As a consequence, the polarization-mixing blocks of the round-trip operator vanish, $\widehat{\mathcal{M}}(\mathbf{E}, \mathbf{M}) = \widehat{\mathcal{M}}(\mathbf{M}, \mathbf{E}) \rightarrow 0$, and the polarization-conserving blocks $\widehat{\mathcal{M}}(\mathbf{E}, \mathbf{E})$ and $\widehat{\mathcal{M}}(\mathbf{M}, \mathbf{M})$ yield independent contributions to the free energy.

In the following, we will derive the explicit matrix elements of the symmetrized round-trip operator in the limit $\xi \rightarrow 0$ for the Drude model, perfect reflectors, and the plasma model.

4.4.1 Drude model

Using the expansion of the modified Bessel functions for small arguments [91, §10.30(i)]

$$I_\nu(z) \simeq \frac{1}{\Gamma(1 + \nu)} \left(\frac{z}{2}\right)^\nu, \quad K_\nu(z) \simeq \frac{\Gamma(\nu)}{2} \left(\frac{2}{z}\right)^\nu, \quad (4.21)$$

the Mie coefficients in the limit $\xi \rightarrow 0$ become [26, p. 110]

$$a_\ell(ix) \simeq (-1)^\ell \frac{\ell + 1}{2\ell(2\ell + 1)} \left(\frac{\ell!}{(2\ell)!}\right)^2 (2x)^{2\ell+1}, \quad (4.22a)$$

$$b_\ell(ix) \propto x^{2\ell+2}, \quad (4.22b)$$

where $x = \xi R/c$. As described in more detail in section 2.5, in the low-frequency limit the Fresnel coefficients become $r_{\text{TM}} = 1$ and $r_{\text{TE}} = 0$ for the Drude model. Consequently, the only contribution comes from the (E, E) polarization block (4.16b)

$$\widehat{\mathcal{M}}_{\ell_1 \ell_2}^m(\mathbf{E}, \mathbf{E}) = \Lambda_{\ell_1 \ell_2}^m \sqrt{|a_{\ell_1} a_{\ell_2}|} B_{\ell_1 \ell_2, \text{TM}}^m. \quad (4.23)$$

Plugging the expression for the Mie coefficient a_ℓ (4.22a) into (4.23), the matrix elements become

$$\widehat{\mathcal{M}}_{\ell_1 \ell_2}^m(\mathbf{E}, \mathbf{E}) = \frac{1}{2} \frac{\ell_1!}{\ell_1(2\ell_1)!} \frac{\ell_2!}{\ell_2(2\ell_2)!} \sqrt{\frac{(\ell_1 - m)!(\ell_2 - m)!}{(\ell_1 + m)!(\ell_2 + m)!}} \left(\frac{2\xi R}{c}\right)^{\ell_1 + \ell_2 + 1} B_{\ell_1 \ell_2, \text{TM}}^m. \quad (4.24)$$

Inserting (4.17b) into (4.24) and using the expression (A.11a) for $P_\ell^m(x)$ when $x \rightarrow \infty$, yields

$$\widehat{\mathcal{M}}_{\ell_1 \ell_2}^m(\mathbf{E}, \mathbf{E}) = \frac{R^{\ell_1 + \ell_2 + 1}}{\sqrt{(\ell_1 + m)!(\ell_1 - m)!(\ell_2 + m)!(\ell_2 - m)!}} \int_0^\infty dk k^{\ell_1 + \ell_2} e^{-2k\mathcal{L}}, \quad (4.25)$$

where we have used that $k = \kappa$ for $\xi = 0$. The evaluation of the integral gives

$$\widehat{\mathcal{M}}_{\ell_1 \ell_2}^m(\mathbf{E}, \mathbf{E}) = \frac{(\ell_1 + \ell_2)!}{\sqrt{(\ell_1 + m)!(\ell_1 - m)!(\ell_2 + m)!(\ell_2 - m)!}} \left(\frac{R}{2\mathcal{L}}\right)^{\ell_1 + \ell_2 + 1} \quad (4.26)$$

for the matrix elements of the round-trip operator in the limit $\xi \rightarrow 0$.

The exact analytical expression for the Casimir free energy in the high-temperature limit for Drude metals has been derived in Ref. [51].

4.4.2 Perfect reflectors

In contrast to the Drude model, for perfect reflectors the Fresnel coefficient r_{TE} does not vanish in the limit $\xi \rightarrow 0$, but becomes $r_{\text{TE}} = -1$. The Mie coefficients become [26, p. 109]

$$a_\ell(ix) \simeq (-1)^\ell \frac{\ell + 1}{2\ell(2\ell + 1)} \left(\frac{\ell!}{(2\ell)!}\right)^2 (2x)^{2\ell + 1}, \quad (4.27a)$$

$$b_\ell(ix) \simeq -\frac{\ell}{\ell + 1} a_\ell. \quad (4.27b)$$

While the expression for a_ℓ is identical to the result obtained for the Drude model, b_ℓ is proportional to $x^{2\ell + 1}$ in contrast to $x^{2\ell + 2}$ in the Drude model. In addition to the contribution from the (E, E) polarization block (4.26), there is also a contribution from the (M, M) polarization block for perfect reflectors

$$\widehat{\mathcal{M}}_{\ell_1 \ell_2}^m(\mathbf{M}, \mathbf{M}) = -\Lambda_{\ell_1 \ell_2}^m \sqrt{|b_{\ell_1} b_{\ell_2}|} B_{\ell_1 \ell_2, \text{TE}}^m. \quad (4.28)$$

A straightforward calculation analogue to the Drude case gives

$$\widehat{\mathcal{M}}_{\ell_1 \ell_2}^m(\mathbf{M}, \mathbf{M}) = \sqrt{\frac{\ell_1 \ell_2}{(\ell_1 + 1)(\ell_2 + 1)}} \frac{(\ell_1 + \ell_2)! \left(\frac{R}{2\mathcal{L}}\right)^{\ell_1 + \ell_2 + 1}}{\sqrt{(\ell_1 + m)!(\ell_1 - m)!(\ell_2 + m)!(\ell_2 - m)!}}. \quad (4.29)$$

The matrix elements for the (E, E) polarization block are identical to the result (4.26) found for the Drude model.

4.4.3 Plasma model

For the plasma model the situation is more involved. The Fresnel coefficient for TM polarization is $r_{\text{TM}} = 1$ as in the cases for perfect reflectors and the Drude model. For TE polarization, however, the Fresnel coefficient becomes, cf. (2.50),

$$r_{\text{TE}} \simeq \frac{c\kappa - \sqrt{c^2\kappa^2 + \omega_{\text{P}}^2}}{ck + \sqrt{c^2k^2 + \omega_{\text{P}}^2}} \quad (4.30)$$

for $\xi \rightarrow 0$. Unlike for the Drude model or perfect reflectors, this expression is not universal and depends on the Plasma frequency ω_{P} . In the limit $\omega_{\text{P}} \rightarrow \infty$, the Fresnel coefficient r_{TE} becomes -1 and the expression for perfect reflectors is recovered. In the opposite limit of $\omega_{\text{P}} \rightarrow 0$, the numerator vanishes and we recover the result for the Drude model. For finite values of the plasma frequency, (4.30) interpolates between the behavior of the Drude model and perfect reflectors.

The Mie coefficient a_ℓ is identical to the expression found for the other two models, and the Mie coefficient b_ℓ becomes [26, pp. 110–111]

$$b_\ell(ix) \simeq (-1)^{\ell+1} \frac{(2x)^{2\ell+1}}{2(2\ell+1)} \left(\frac{\ell!}{(2\ell)!} \right)^2 \left(1 - \frac{2\ell+1}{\alpha} \frac{I_{\ell+1/2}(\alpha)}{I_{\ell-1/2}(\alpha)} \right) \quad (4.31)$$

where $\alpha = \omega_{\text{P}}R/c$. As for the Fresnel coefficient r_{TE} , this result interpolates between the behavior of perfect reflectors ($\alpha \rightarrow \infty$) and the Drude model ($\alpha \rightarrow 0$). The matrix elements corresponding to the (M, M) polarization block are given by [26, p. 120]

$$\begin{aligned} \widehat{\mathcal{M}}_{\ell_1\ell_2}^m(\text{M}, \text{M}) &= \sqrt{\frac{\ell_1\ell_2}{(\ell_1+1)(\ell_2+1)}} \frac{\left(\frac{R}{2\mathcal{L}}\right)^{\ell_1+\ell_2+1}}{\sqrt{(\ell_1+m)!(\ell_1-m)!(\ell_2+m)!(\ell_2-m)!}} \\ &\times \sqrt{1 - \frac{2\ell_1+1}{\alpha} \frac{I_{\ell_1+1/2}(\alpha)}{I_{\ell_1-1/2}(\alpha)}} \sqrt{1 - \frac{2\ell_2+1}{\alpha} \frac{I_{\ell_2+1/2}(\alpha)}{I_{\ell_2-1/2}(\alpha)}} \\ &\times \int_0^\infty dx x^{\ell_1+\ell_2} e^{-x} \frac{\sqrt{x^2 + \beta^2} - x}{\sqrt{x^2 + \beta^2} + x} \end{aligned} \quad (4.32)$$

where $\beta = 2\omega_{\text{P}}\mathcal{L}/c$. The integral in the last line of (4.32) has to be evaluated numerically. For the (E, E) polarization block, the matrix elements are identical to the result for the Drude model (4.26).

4.5 Properties of the round-trip matrices

In this section, we study properties of the symmetrized round-trip operator $\widehat{\mathcal{M}}^m$ and the corresponding scattering operator $\mathbb{1} - \widehat{\mathcal{M}}^m$. These properties ensure the stability of the numerical evaluation and can be used to improve the efficiency of the numerical evaluation.

4.5.1 Negative values of m

For negative values of m , the normalizing coefficient can be expressed as ($m > 0$)

$$\Lambda_{\ell_1 \ell_2}^{-m} = \frac{(\ell_1 + m)! (\ell_2 + m)!}{(\ell_1 - m)! (\ell_2 - m)!} \Lambda_{\ell_1 \ell_2}^m, \quad (4.33)$$

and the associated Legendre polynomials become (cf. appendix A.2)

$$P_\ell^{-m}(x) = \frac{(\ell - m)!}{(\ell + m)!} P_\ell^m(x). \quad (4.34)$$

Consequently, the polarization conserving blocks $\widehat{\mathcal{M}}^m(\text{E}, \text{E})$ and $\widehat{\mathcal{M}}^m(\text{M}, \text{M})$ do not change when $m \rightarrow -m$. In contrast, the polarization mixing blocks $\widehat{\mathcal{M}}^m(\text{M}, \text{E})$ and $\widehat{\mathcal{M}}^m(\text{E}, \text{M})$ change sign due to the factor of m in the integral $C_{\ell_1 \ell_2, p}^m$ (4.17c). The determinant of $\mathbb{1} - \widehat{\mathcal{M}}^{-m}$

$$\log \det \left(\mathbb{1} - \widehat{\mathcal{M}}^{-m} \right) = \log \det \begin{pmatrix} \mathbb{1} - \widehat{\mathcal{M}}^m(\text{E}, \text{E}) & +\widehat{\mathcal{M}}^m(\text{E}, \text{M}) \\ +\widehat{\mathcal{M}}^m(\text{M}, \text{E}) & \mathbb{1} - \widehat{\mathcal{M}}^m(\text{M}, \text{M}) \end{pmatrix} \stackrel{\text{(B.23)}}{=} \log \det \left(\mathbb{1} - \widehat{\mathcal{M}}^m \right) \quad (4.35)$$

is the same as that of $\mathbb{1} - \widehat{\mathcal{M}}^m$ as shown in appendix B.3. Therefore, positive and negative values of m yield the same contribution to the free energy.

4.5.2 Diagonal dominance

With the phase convention described in appendix A.2, the associated Legendre polynomials $P_\ell^m(x)$ are real and positive for $x > 1$. As a consequence, the matrix elements of the round-trip operator $\widehat{\mathcal{M}}^m$ are real. Since the integrals $A_{\ell_1 \ell_2, p}^m$ and $B_{\ell_1 \ell_2, p}^m$ are symmetric with respect to ℓ_1, ℓ_2 , and $\widehat{\mathcal{M}}_{\ell_1 \ell_2}^m(\text{M}, \text{E}) = \widehat{\mathcal{M}}_{\ell_2 \ell_1}^m(\text{E}, \text{M})$, the round-trip operator is symmetric

$$\left(\widehat{\mathcal{M}}^m \right)^T = \widehat{\mathcal{M}}^m. \quad (4.36)$$

The Fresnel coefficients are positive for $p = \text{TM}$ and negative for $p = \text{TE}$,

$$-1 \leq r_{\text{TE}} \leq 0 \leq r_{\text{TM}} \leq 1. \quad (4.37)$$

Therefore, all factors in (4.16) are non-negative and hence all matrix elements of $\widehat{\mathcal{M}}^m$ are non-negative. Consequently, all non-diagonal matrix elements of the scattering matrix $\mathbb{1} - \widehat{\mathcal{M}}^m$ are non-positive. Furthermore, numerical tests show that the diagonal elements of the scattering matrix are positive.

In the following, we will give analytical and numerical evidence that the scattering operator $\mathbb{1} - \widehat{\mathcal{M}}^m$ is strictly diagonally dominant. A matrix $A = (a_{jk})$ is said to be strictly diagonally dominant if

$$|a_{jj}| > \sum_{j \neq k} |a_{jk}| \quad \text{for all } k. \quad (4.38)$$

As all matrix elements of $\widehat{\mathcal{M}}^m$ and the diagonal elements of $\mathbb{1} - \widehat{\mathcal{M}}^m$ are non-negative, the condition (4.38) becomes

$$\sum_{\ell_1, P_1} \widehat{\mathcal{M}}_{\ell_1 \ell_2}^m(P_1, P_2) < 1 \quad \text{for all } \ell_2, P_2. \quad (4.39)$$

The matrix elements of the round-trip operator are largest for the model of perfect reflectors. Therefore, it is sufficient to consider perfect reflectors in the following. If the scattering operator is strictly diagonally dominant for perfect reflectors, then the scattering operator is strictly diagonally dominant for any dielectric function.

In the low frequency limit it is easy to show that the scattering operator is strictly diagonally dominant. For $\xi \rightarrow 0$ the scattering operator is block-diagonal with the polarization blocks $\widehat{\mathcal{M}}^m(\text{E}, \text{E})$ and $\widehat{\mathcal{M}}^m(\text{M}, \text{M})$. Since $\widehat{\mathcal{M}}_{\ell_1 \ell_2}^m(\text{E}, \text{E}) \geq \widehat{\mathcal{M}}_{\ell_1 \ell_2}^m(\text{M}, \text{M})$, it is sufficient to consider the (E, E) polarization block. For this block we find

$$\begin{aligned} \sum_{\ell_1=\max(1,m)}^{\infty} \widehat{\mathcal{M}}_{\ell_1 \ell_2}^m(\text{E}, \text{E}) &\leq \sum_{\ell_1=1}^{\infty} \widehat{\mathcal{M}}_{\ell_1 \ell_2}^0(\text{E}, \text{E}) = \sum_{\ell_1=1}^{\infty} \frac{(\ell_1 + \ell_2)!}{\ell_1! \ell_2!} \left(\frac{R}{2\mathcal{L}}\right)^{\ell_1 + \ell_2 + 1} \\ &< \sum_{\ell_1=1}^{\infty} \binom{\ell_1 + \ell_2}{\ell_2} \left(\frac{1}{2}\right)^{\ell_1 + \ell_2 + 1} = 1 - \left(\frac{1}{2}\right)^{\ell_2 + 1} \leq 1, \end{aligned} \quad (4.40)$$

where we used $(\ell+m)!(\ell-m)! \geq (\ell!)^2$ in the first line. In addition, the scattering operator is strictly diagonally dominant in the limit of large separations, because the matrix elements of the round-trip operator become small due to the exponential factor in (4.17).

For arbitrary values of m , ξ and R/L , it is challenging to prove that the scattering operator $\mathbb{1} - \widehat{\mathcal{M}}^m$ is strictly diagonally dominant. Instead, we compute the round-trip matrix numerically for different values of m and ξ , and show that the condition (4.39) is fulfilled for aspect ratios as high as $R/L = 2000$. Fig. 4.4 depicts the maximum row sum of the round-trip operator for $m = 0, 1, 2, 3$ as a function of $\xi\mathcal{L}/c$. In all cases, the maximum row sum is smaller than 1 implying that the scattering operator is strictly diagonally dominant. Therefore, it is highly probable that the scattering operator is strictly diagonally dominant for all parameters.

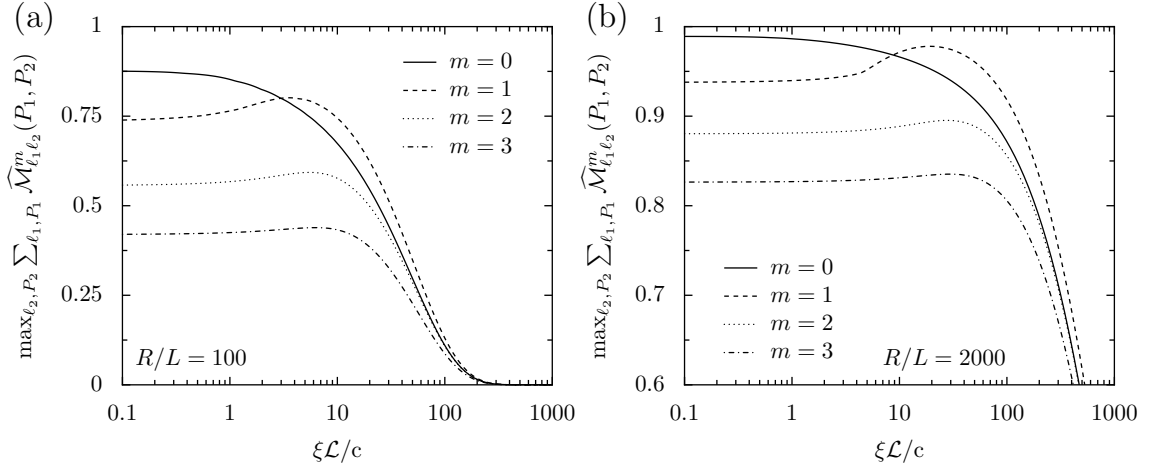


Figure 4.4: Maximum row sum of the round-trip operator $\widehat{\mathcal{M}}^m$ for perfect reflectors, and aspect ratios (a) $R/L = 100$ and (b) $R/L = 2000$ as a function of $\xi\mathcal{L}/c$. The different curves correspond to different values of m . In all cases, the maximum is smaller than 1 implying that the scattering operator $\mathbb{1} - \widehat{\mathcal{M}}^m$ is strictly diagonally dominant.

4.5.3 Positive definiteness

The scattering operator $\mathbb{1} - \widehat{\mathcal{M}}^m$ is symmetric, diagonally dominant, and all diagonal matrix elements are positive. These properties imply that the scattering operator is positive definite. As a consequence, the determinant is positive and the free energy is real. Moreover, this allows to compute the determinant of the scattering operator using a Cholesky decomposition which is roughly twice as fast as an LU decomposition.

The fact that the scattering operator is symmetric and diagonally dominant ensures the stability of the numerical evaluation of the determinant. Due to numerical errors, the scattering matrix $\mathcal{D}^m \equiv \mathbb{1} - \widehat{\mathcal{M}}^m$ cannot be computed exactly, but a slightly perturbed matrix $\widetilde{\mathcal{D}}^m$ will be computed. The numerical error will be dominated by the numerical evaluation of the integrals in (4.17). If the relative error of the matrix elements is bounded by $0 \leq \epsilon \ll 1$, then [124]

$$\log \det(\widetilde{\mathcal{D}}^m) = \log \det(\mathcal{D}^m) + \sum_{j=1}^N \log(1 + \eta_j), \quad (4.41)$$

where $N = 2\ell_{\text{dim}}$ denotes the dimension of the matrix and $|\eta_j| \leq \epsilon$. The error can be estimated by

$$\left| \sum_{j=1}^N \log(1 + \eta_j) \right| \lesssim N\epsilon. \quad (4.42)$$

Small perturbations in the matrix elements thus only cause small changes in the value of the determinant. In fact, numerical tests suggest that the typical error is considerable smaller than the bound (4.42).

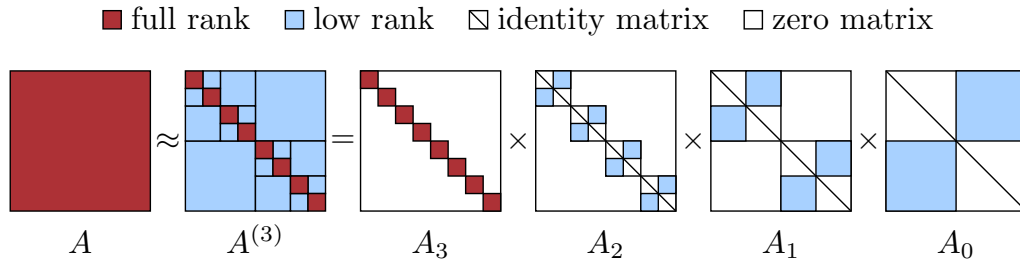


Figure 4.5: Graphical representation of the factorization (4.44) of a HODLR matrix for $n = 3$. Red blocks represent full-rank matrices while bright blue blocks correspond to low-rank matrices (after [125]).

4.6 Hierarchical matrices

The symmetrization allows to exploit further properties of the round-trip matrices. As the matrix elements decrease away from the diagonal, it is evident that the dominant contribution to the determinant comes from matrix elements close to the diagonal. In fact, it turns out that the matrices $\mathbb{1} - \widehat{\mathcal{M}}^m$ are hierarchical off-diagonal low-rank (HODLR) matrices [125–128]. This means that the round-trip matrices can be sub-divided into a hierarchy of rectangular blocks which can be approximated by low-rank matrices. Originally introduced in the context of integral equations, hierarchical matrices find application in finite element methods, kernel density estimation in machine learning, Gaussian processes, Kalman filtering, and radial basis interpolation (see Ref. [126] and references therein).

A low-rank matrix M of dimension $N \times N$ can be efficiently approximated by

$$M \approx UV^T, \quad (4.43)$$

where U and V are matrices of dimension $N \times p$ with $p \ll N$. The best rank p approximation of M can be obtained using the singular value decomposition [129]. Instead of a computationally expensive full singular-value decomposition, low-rank approximations can be computed using fast algorithms like adaptive cross approximation, pseudo-skeletal approximations, interpolatory decompositions or rank revealing QR and LU (see Ref. [125] and references therein).

A HODLR matrix A can be factored into $n + 1$ block-diagonal matrices

$$A \approx A^{(n)} = A_n A_{n-1} \dots A_0 \quad (4.44)$$

as sketched in Fig. 4.5 for $n = 3$. The matrix A_n consists of 2^n full-rank blocks around the diagonal while the other matrices A_{n-1} to A_0 represent low-rank updates to the identity. The error of this approximation can be made negligibly small by choosing appropriate ranks p .

The factorization (4.44) allows for a fast computation of the determinant $A^{(n)}$ for two reasons. Firstly, one can exploit the multiplicativity of determinants. Secondly, the block matrices appearing in A_0 to A_{n-1} are of the form

$$B = \begin{pmatrix} \mathbf{1} & U_1 V_1^T \\ U_2 V_2^T & \mathbf{1} \end{pmatrix}, \quad (4.45)$$

requiring at first sight the evaluation of the determinant of an $N \times N$ -matrix according to

$$\det(B) = \det(\mathbf{1} - U_1 V_1^T U_2 V_2^T). \quad (4.46)$$

However, exploiting Sylvester's determinant identity

$$\det(\mathbf{1} + AB) = \det(\mathbf{1} + BA), \quad (4.47)$$

we obtain

$$\det(B) = \det(\mathbf{1} - V_2^T U_1 V_1^T U_2). \quad (4.48)$$

It is thus sufficient to evaluate the determinant of a $p \times p$ -matrix, resulting in a significant speed-up.

In order to assess the numerical advantages of the approach discussed above, we compute the determinants of the scattering matrices either by means of a Cholesky decomposition or the implementation [130] of the algorithm for HODLR matrices described in Ref. [125]. The Cholesky decomposition factorizes a symmetric positive-definite matrix into the product of a triangular matrix and its transpose allowing for a simple computation of the determinant. The factorization requires $\mathcal{O}(N^3)$ of time for an $N \times N$ matrix and is about twice as fast as an LU decomposition. The computation of determinants using the HODLR approach takes $\mathcal{O}(p^2 N \log^2 N)$ steps where, depending on the nature of the problem, p may be a function of N .

In Fig. 4.6, we compare the average time to compute $\log \det(\mathbf{1} - \widehat{\mathcal{M}}^m(\xi))$ depending on the aspect ratio using the HODLR approach and a Cholesky decomposition. We specifically choose $m = 1$, $\xi = c/(L + R)$, and perfect reflectors, but other parameters yield similar results. For aspect ratios $R/L \lesssim 100$, both algorithms need roughly the same time. For larger aspect ratios $R/L \gtrsim 200$, the computational time using the Cholesky decomposition scales as $\propto (R/L)^{2.56}$. This is faster than the theoretical complexity $\mathcal{O}((R/L)^3)$ of the Cholesky decomposition, because our numerical implementation saves and reuses intermediate values so that the computational time per matrix element is not constant. In contrast, the HODLR algorithm becomes significantly faster for $R/L \gtrsim 200$ and the computational time scales only as $\propto (R/L)^{1.31}$. For the largest aspect ratio $R/L = 2000$ displayed in Fig. 4.6, we find a speed-up by a factor 33. At even larger aspect ratios, the time required by the Cholesky decomposition becomes prohibitively long.

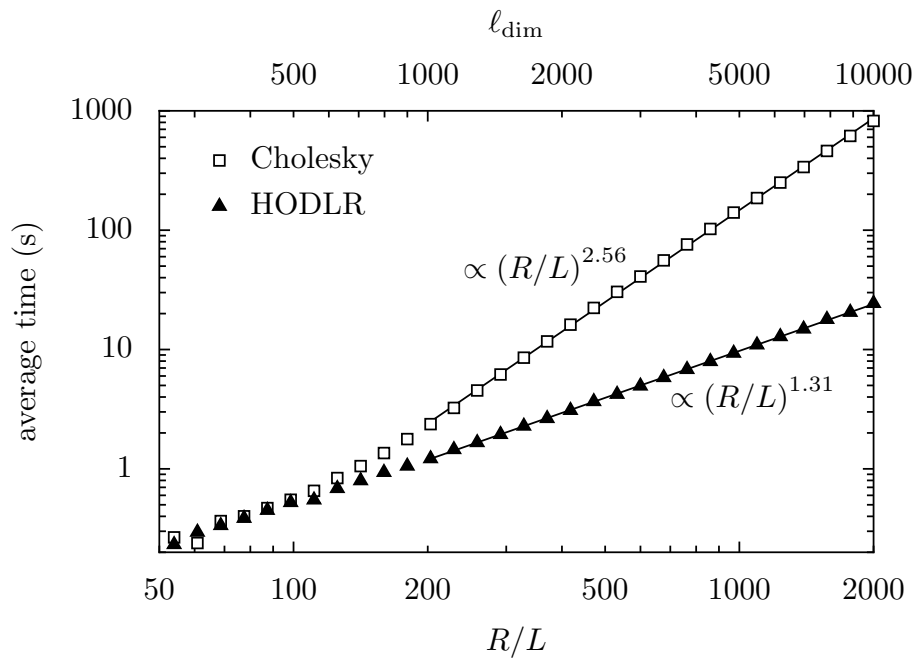


Figure 4.6: Average run-time to compute $\log \det (\mathbb{1} - \widehat{\mathcal{M}}^m(\xi))$ as a function of the aspect ratio R/L for $m = 1, \xi = c/(L + R)$, and perfect reflectors. The angular momentum is truncated at $\ell_{\text{dim}} = 5R/L$, yielding a scattering matrix of dimension $2\ell_{\text{dim}} \times 2\ell_{\text{dim}}$. Squares and triangles correspond to a computation using Cholesky decomposition and the HODLR algorithm [130], respectively. The lines represent fits and correspond to the asymptotic scaling of the two algorithms. The computations were carried out on an Intel Core i7 with 3.4 GHz. For the Cholesky decomposition LAPACK [131] in combination with ATLAS [132, 133] was used.

In this chapter, we have derived the matrix elements of the round-trip operator for the plane-sphere geometry in the multipole basis. Since the argument of the associated Legendre polynomials diverges for the Matsubara frequency $\xi_0 = 0$, we have computed the limit $\xi \rightarrow 0$ analytically. For the round-trip operator, we have used a symmetrized version that avoids ill-conditioned matrices. Moreover, the symmetrized round-trip operator allows an evaluation of the determinants using techniques of hierarchical matrices resulting in a significant speedup.

In the next chapter, we will discuss technical details of the numerical evaluation of the scattering formula in the multipole basis. After that, we will compare numerically exact results of the Casimir interaction with results obtained using the proximity force approximation.

Chapter 5

Numerical issues

In the last chapter, we have introduced the key ingredients to push the numerics to aspect ratios used in typical experiments: the symmetrization of the round-trip operator and the hierarchical factorization of the round-trip matrix. In this chapter, we will discuss various numerical issues that are also important for a fast and stable numerical implementation of the Casimir effect in the plane-sphere geometry. Since the issues are rather technical, a reader not interested in the details of the numerical implementation might want to skip this chapter.

In the first part of this chapter, we describe fast algorithms to evaluate the dilogarithm, modified Bessel functions of the first and of the second kind, ordinary Legendre polynomials, and associated Legendre polynomials. The algorithms presented here are tweaked for the requirements of the Casimir effect and are both faster and more stable than the general purpose implementations found in typical numerical libraries. We then study the effect of the truncation of the vector space and present an estimate for the truncation error. The evaluation of the integrals (4.17) appearing in the matrix elements of the round-trip operator is described in section 5.6. We then turn to the evaluation of the determinant of the scattering matrix. In particular, we show how the trace can be used to approximate the determinant. This helps to speed up the computation and to avoid a loss of significance in some cases. After a short discussion about numerical differentiation, we conclude the chapter listing various tests and checks we have made to ensure that the numerical implementation is correct.

5.1 Dilogarithm

The numerical evaluation of the free energy within the proximity force approximation (3.35) relies on the computation of the dilogarithm $\text{Li}_2(x)$. For arguments $0 \leq x \leq 1$, the

dilogarithm is defined as [91, §25.12.1]

$$\operatorname{Li}_2(x) = \sum_{n=1}^{\infty} \frac{x^n}{n^2}. \quad (5.1)$$

Special values are $\operatorname{Li}_2(0) = 0$ and $\operatorname{Li}_2(1) = \pi^2/6$. The n^2 rate of convergence of the series (5.1) can be improved to n^4 [134]

$$\operatorname{Li}_2(x) = \frac{x}{x+1} \left(3 + \sum_{n=1}^{\infty} \frac{x^n}{n^2(n+1)^2} \right) - 2 \frac{x-1}{x+1} \log(1-x). \quad (5.2)$$

It is sufficient to evaluate 30 terms of the series in (5.2) in order to achieve a relative error of less than 10^{-15} for arguments $0 \leq x \leq 0.5$. Arguments in the interval $(0.5, 1]$ can be mapped to $[0, 0.5)$ using [91, §25.12.6]

$$\operatorname{Li}_2(x) = \frac{\pi^2}{6} - \log(x) \log(1-x) - \operatorname{Li}_2(1-x), \quad \frac{1}{2} < x < 1. \quad (5.3)$$

From (5.3) one also finds $\operatorname{Li}_2(1/2) = \pi^2/12 - (\log 2)^2/2$.

5.2 Modified Bessel functions

The evaluation of the Legendre polynomials $P_\ell(x)$ described in section 5.3 relies on the computation of modified Bessel functions of the first kind $I_n(x)$ at integer orders n . To compute the Mie coefficients $a_\ell(ix)$, $b_\ell(ix)$, one has to evaluate the modified Bessel functions of the first kind $I_{n+1/2}(x)$ and of the second kind $K_{n+1/2}(x)$ at half-integer orders. In this section, we briefly describe how the modified Bessel functions can be computed efficiently for integer and half-integer orders.

5.2.1 Modified Bessel functions of integer order

The modified Bessel functions $I_0(x)$ and $I_1(x)$ have exponential behavior for large arguments. Once the exponential factor is removed, both functions are smooth and can be evaluated using Chebychev expansions. We partition the range into the sub-intervals $[0, 8]$ and $(8, \infty)$, and evaluate the functions in each sub-interval using a Chebychev expansion [135].

For orders $n \geq 2$, the modified Bessel functions $I_n(x)$ can be computed using the recurrence relation [91, §10.29(i)]

$$I_{n+1}(x) = -\frac{2n}{x} I_n(x) + I_{n-1}(x). \quad (5.4)$$

Unfortunately, this recurrence relation is unstable in upwards direction. Since the Bessel functions grow exponentially, the terms on the right hand-side become large, and the subtraction causes a catastrophic loss of significance. In contrast, in downwards direction the recurrence relation is stable and any seed values will converge to the correct sequence of functions. Choosing two seed values for large orders, one obtains the correct value of $I_n(x)$ times a normalization constant. The normalization constant can be fixed by a comparison with $I_0(x)$. This idea is also known as Miller's algorithm [136, pp. 230–240].

5.2.2 Modified Bessel functions of half-integer order

The modified Bessel functions for half-integer orders $n + 1/2$, n being an integer, satisfy the recurrence relations [91, §10.29(i)]

$$I_{n+1/2}(x) = -\frac{2n-1}{x}I_{n-1/2}(x) + I_{n-3/2}(x), \quad (5.5a)$$

$$K_{n+1/2}(x) = +\frac{2n-1}{x}K_{n-1/2}(x) + K_{n-3/2}(x). \quad (5.5b)$$

Using the analytical expressions for low orders [91, §10.39.1, §10.39.2]

$$I_{1/2}(x) = \sqrt{\frac{2}{\pi x}} \sinh x, \quad K_{1/2}(x) = \sqrt{\frac{\pi}{2x}} e^{-x}, \quad (5.6a)$$

$$I_{3/2}(x) = \sqrt{\frac{2}{\pi x}} \left(\cosh x - \frac{\sinh x}{x} \right), \quad K_{3/2}(x) = \sqrt{\frac{\pi}{2x}} \left(1 + \frac{1}{x} \right) e^{-x}, \quad (5.6b)$$

the recurrence relations can in principle be used to evaluate the modified Bessel functions. For $K_{n+1/2}(x)$ the recurrence relation is stable in upwards direction and the computation is straightforward. However, as for integer orders, the recurrence relation for $I_{n+1/2}(x)$ is unstable in upwards direction. The function $I_{n+1/2}(x)$ can be once more computed using Miller's algorithm [136, pp. 230–240]. The fraction $I_{n+3/2}(x)/I_{n+1/2}(x)$ can be evaluated using the continued fraction [91, §10.33]

$$\frac{I_{n+3/2}(x)}{I_{n+1/2}(x)} = \frac{1}{a_1 + \frac{1}{a_2 + \frac{1}{a_3 + \dots}}} = [a_1, a_2, a_3, \dots] \quad (5.7)$$

where

$$a_j = \frac{2(n+j)+1}{x}. \quad (5.8)$$

Consequently, we can choose an arbitrary constant for $I_{n+1/2}(x)$ and compute $I_{n-1/2}(x)$ using the continued fraction (5.7) depending on the chosen constant. The constant and hence $I_{n+1/2}(x)$ can then be obtained using the recurrence relation (5.5a) in downwards direction and a comparison with $I_{1/2}(x)$. The numerical evaluation of continued fractions is described in Ref. [136, pp. 169–173] or in Ref. [91, §3.10].

5.3 Legendre polynomials

The efficient evaluation of associated Legendre functions $P_\ell^m(x)$ presented in section 5.4 relies on a fast computation of ordinary Legendre polynomials $P_\ell(x)$ for $x \geq 1$. In this section, we describe an algorithm developed by Bogaert, Michiels and Fostier to compute the Legendre polynomials

$$P_\ell(x) = \frac{1}{2^\ell \ell!} \frac{d^\ell}{dx^\ell} (x^2 - 1)^\ell \quad (5.9)$$

with complexity $\mathcal{O}(1)$ [137]. While the algorithm was originally developed for arguments $x \in [-1, 1]$, it can be adapted to the domain $x \geq 1$. For $\ell < 100$, we evaluate the Legendre polynomials using a recurrence relation. Orders $\ell \geq 100$ are computed using asymptotic expansions for either small or large arguments. For the sake of completeness and since the asymptotic expansions slightly differ for $x \in [-1, 1]$ and $x \geq 1$, we will state all equations needed to compute $P_\ell(x)$.

5.3.1 Evaluation using recurrence relation

For $\ell < 100$, we compute the Legendre polynomials using the recurrence relation

$$(\ell + 1)P_{\ell+1}(x) = (2\ell + 1)xP_\ell(x) - \ell P_{\ell-1}(x) \quad (5.10)$$

with the initial values $P_0(x) = 1$ and $P_1(x) = x$. Since the recurrence relation is stable in upwards direction, the evaluation is straightforward.

5.3.2 Asymptotic expansion for large arguments

For $\ell \geq 100$ and large arguments

$$(\ell + 1) \sinh x > 25, \quad (5.11)$$

the Legendre polynomials can be evaluated using the asymptotic expansion

$$P_\ell(\cosh x) \simeq \left(\frac{2}{\pi \sinh x} \right)^{1/2} \sum_{m=0}^{M-1} C_{\ell,m} \frac{\cosh \left[\left(m + \ell + \frac{1}{2} \right) x \right]}{\sinh^m x}. \quad (5.12)$$

The coefficients $C_{\ell,m}$ are given in terms of the recurrence relation

$$C_{\ell,m+1} = \frac{\left(m + \frac{1}{2} \right)^2}{2(m+1) \left(\ell + m + \frac{3}{2} \right)} C_{\ell,m} \quad (5.13)$$

with the initial value

$$C_{\ell,0} = \frac{\Gamma(\ell + 1)}{\Gamma(\ell + \frac{3}{2})}. \quad (5.14)$$

Choosing $M = 17$, the error of (5.12) is smaller than machine precision.

5.3.3 Asymptotic expansion for small arguments

For $\ell \geq 100$ and

$$(\ell + 1) \sinh x \leq 25, \quad (5.15)$$

the Legendre polynomials can be evaluated using the asymptotic expansion

$$P_\ell(\cosh x) \simeq \sum_{n=0}^{12} \frac{f_n(x\nu)}{\nu^n} \quad (5.16)$$

where $\nu = \ell + 1/2$. The functions $f_n(x)$ vanish for odd values of n

$$f_{2n+1}(x) = 0, \quad (5.17)$$

and for even values of n they are given by

$$\begin{aligned} f_0(x) &= h_0(x), \\ f_2(x) &= \frac{1}{8}h_1(x) - \frac{1}{12}h_2(x), \\ f_4(x) &= \frac{11}{384}h_2(x) - \frac{7}{160}h_3(x) + \frac{1}{160}h_4(x), \\ f_6(x) &= \frac{173}{15360}h_3(x) - \frac{101}{3584}h_4(x) + \frac{671}{80640}h_5(x) - \frac{61}{120960}h_6(x), \\ f_8(x) &= \frac{22931}{3440640}h_4(x) - \frac{90497}{3870720}h_5(x) + \frac{217}{20480}h_6(x) - \frac{1261}{967680}h_7(x) + \frac{1261}{29030400}h_8(x), \\ f_{10}(x) &= \frac{1319183}{247726080}h_5(x) - \frac{10918993}{454164480}h_6(x) + \frac{1676287}{113541120}h_7(x) - \frac{7034857}{2554675200}h_8(x) \\ &\quad + \frac{1501}{8110080}h_9(x) - \frac{79}{20275200}h_{10}(x), \\ f_{12}(x) &= \frac{233526463}{43599790080}h_6(x) - \frac{1396004969}{47233105920}h_7(x) + \frac{2323237523}{101213798400}h_8(x) \\ &\quad - \frac{72836747}{12651724800}h_9(x) + \frac{3135577}{5367398400}h_{10}(x) - \frac{1532789}{61993451520}h_{11}(x) \\ &\quad + \frac{66643}{185980354560}h_{12}(x), \end{aligned} \quad (5.18)$$

where the function $h_n(x)$ is defined as

$$h_n(x) = (-x)^n I_n(x). \quad (5.19)$$

Here, $I_n(x)$ denotes the modified Bessel function of the first kind.

5.4 Associated Legendre polynomials

The evaluation of the integrals (4.17) requires the evaluation of the associated Legendre polynomials $P_\ell^m(x)$. For large aspect ratios $R/L \gg 1$, the dominant contribution to the Casimir free energy comes from $\ell \sim R/L$ and $m \sim \sqrt{R/L}$ [48–50]. Therefore, the numerical implementation of the associated Legendre polynomials should be optimized for $\ell \gg m$.

We choose the phase convention according to Ref. [138, p. 94] and define the associated Legendre polynomials as

$$P_\ell^m(x) = (x^2 - 1)^{m/2} \frac{d^m}{dx^m} P_\ell(x). \quad (5.20)$$

Then the associated Legendre polynomials for arguments $x \geq 1$ are real and non-negative for all degrees and orders. Further properties of the associated Legendre polynomials are described in appendix A.2.

Depending on ℓ and m , we use three different approaches to compute $P_\ell^m(x)$:

- For $m = 0$, the associated Legendre polynomials become ordinary Legendre polynomials and can be evaluated using the algorithm described in section 5.3.
- If order and degree are close, $\ell - m \lesssim 200$, we use an upwards recurrence in ℓ .
- Otherwise, a downwards recurrence in m is used.

5.4.1 Upwards recurrence in ℓ

The associated Legendre polynomials $P_\ell^m(x)$ satisfy the recurrence relation (A.5c)

$$(\ell - m + 1)P_{\ell+1}^m(x) = (2\ell + 1)xP_\ell^m(x) - (\ell + m)P_{\ell-1}^m(x) \quad (5.21)$$

with the initial values given by (A.6)

$$P_m^m(x) = \frac{(2m)!}{2^m m!} (x^2 - 1)^{m/2}, \quad (5.22a)$$

$$P_{m+1}^m(x) = (2m + 1)xP_m^m(x). \quad (5.22b)$$

The recurrence relation is stable in upwards direction. Since the recurrence requires $\mathcal{O}(\ell - m)$ steps, this approach is only efficient if degree and order are close.

5.4.2 Downwards recurrence in m

For $\ell - m \gtrsim 200$, it is more efficient to use the recurrence relation (A.5b)

$$P_\ell^{m+1}(x) = (\ell + m)(\ell - m + 1)P_\ell^{m-1}(x) - \frac{2mx}{\sqrt{x^2 - 1}}P_\ell^m(x) \quad (5.23)$$

starting from $P_\ell(x)$. The recurrence in m only requires $\mathcal{O}(m)$ steps, in contrast to the recurrence (5.21) in ℓ which needs $\mathcal{O}(\ell - m)$ steps.

Unfortunately, the recurrence relation (5.23) is numerically unstable in upwards direction. The difference of the two terms on the right hand side of (5.23) results in a loss of significance. The solution to this problem is once more Miller's algorithm [136, pp. 230–240] in combination with a continued fraction. The ratio of $P_\ell^m(x)$ and $P_\ell^{m-1}(x)$ can be computed using the continued fraction [91, §14.14]

$$\frac{1}{2}(x^2 - 1)^{1/2} \frac{P_\ell^m(x)}{P_\ell^{m-1}(x)} = \frac{x_0}{y_0 +} \frac{x_1}{y_1 +} \frac{x_2}{y_2 +} \frac{x_3}{y_3 +} \cdots \quad (5.24)$$

where

$$\begin{aligned} x_k &= \frac{1}{4}(\ell - m - k + 1)(\ell + m + k)(x^2 - 1), \\ y_k &= (m + k)x. \end{aligned} \quad (5.25)$$

The notation and the numerical evaluation of continued fractions are described in Ref. [136, pp. 169–173] or Ref. [91, §3.10]. The evaluation is analogous to the computation of the modified Bessel functions $I_{n+1/2}(x)$ for half-integer order.

5.4.3 Logarithmic derivative

For the fast evaluation of the integrals (4.17) described in section 5.6, the first and second logarithmic derivative of the associated Legendre polynomials are needed. The first logarithmic derivative can be obtained using (A.7)

$$\frac{d}{dx} \log(P_\ell^m(x)) = \frac{1}{\sqrt{x^2 - 1}} \frac{P_\ell^{m+1}(x)}{P_\ell^m(x)} + \frac{mx}{x^2 - 1}, \quad (5.26)$$

and the second logarithmic derivative is given by

$$\frac{d^2}{dx^2} \log(P_\ell^m(x)) = \frac{1}{x^2 - 1} \left[\frac{P_\ell^{m+2}(x)}{P_\ell^m(x)} - \left(\frac{P_\ell^{m+1}(x)}{P_\ell^m(x)} \right)^2 - \frac{m(x^2 + 1)}{x^2 - 1} \right]. \quad (5.27)$$

The fractions of associated Legendre polynomials with differing order can be computed using the continued fraction (5.24) noting that

$$\frac{P_\ell^{m+2}(x)}{P_\ell^m(x)} = \frac{P_\ell^{m+2}(x)}{P_\ell^{m+1}(x)} \frac{P_\ell^{m+1}(x)}{P_\ell^m(x)}. \quad (5.28)$$

Interestingly, the associated Legendre polynomials for $x > 1$ and $m > 0$ obey the inequality

$$[P_\ell^m(x)]^2 - P_\ell^{m+1}(x)P_\ell^{m-1}(x) \geq 0 \quad (5.29)$$

which is similar to Turán's inequality

$$P_\ell(x)^2 - P_{\ell-1}(x)P_{\ell+1}(x) \geq 0 \quad \text{for } n > 1, -1 \leq x \leq 1. \quad (5.30)$$

Similar inequalities have been found for other orthogonal polynomials like Gegenbauer, Hermite, Laguerre or Bessel functions [139]. The inequality (5.29), however, seems to be unknown in the literature. Using inequality (5.29), one can show that the second logarithmic derivative is negative for $m \geq 0$

$$\frac{d^2}{dx^2} \log(P_\ell^m(x)) \leq -\frac{m(x^2+1)}{(x^2-1)^2} \leq 0. \quad (5.31)$$

As a consequence, the function $\log(P_\ell^m(x))$ is concave. A proof of (5.29) is given in appendix B.2.

5.5 Truncation of the vector space

The multipole basis $\{|\ell, m, P, s\rangle\}$ with

$$\ell = 1, 2, 3, \dots, \quad |m| \leq \ell, \quad P = \{E, M\}, \quad s = \{\text{reg}, \text{out}\}, \quad (5.32)$$

is a discrete and infinite basis. For a numerical evaluation, the vector space has to be truncated according to $\ell_{\min} \leq \ell \leq \ell_{\max}$. As discussed in more detail in chapter 3, in the semiclassical approximation the localization principle [104] connects waves with angular momenta $\ell \gg 1$ to localized rays defining an impact parameter $b = \ell c / \xi$. Impact parameters $b \gg R$ correspond to rays that do not hit the sphere implying that angular momenta $\ell \gg \xi R / c$ yield a negligible contribution to the Casimir interaction. For small separations $L \ll R$, we have $\kappa \sim 1/L$ which can be seen from the expression of the proximity force approximation (3.35). As $\kappa \sim \xi/c$, the main contribution comes from angular momentum values $\ell \lesssim R/L$. The same result has also been obtained by an asymptotic expansion of the Casimir energy in the multipole basis [48–50].

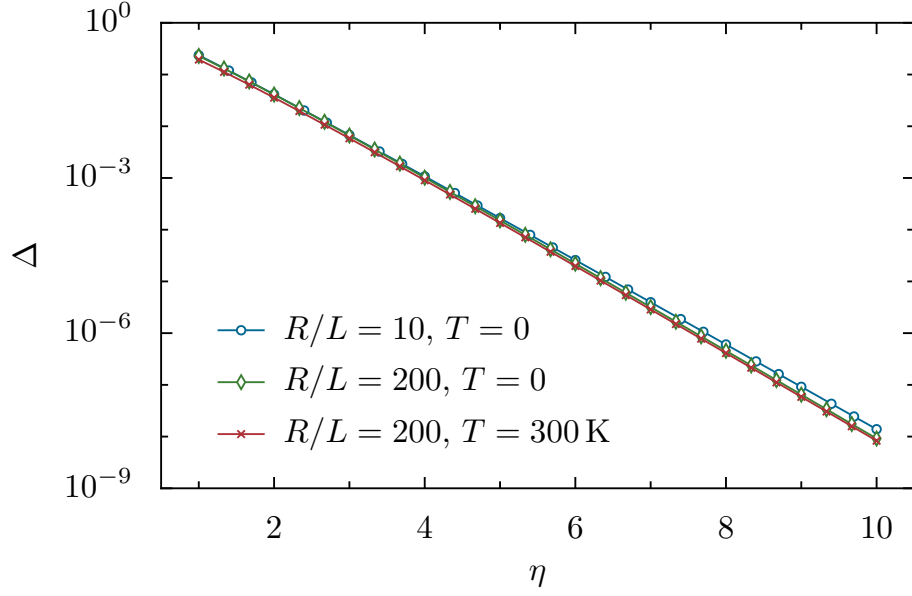


Figure 5.1: Relative error Δ due to the truncation of the vector space as a function of η for different aspect ratios and temperatures. The relative error depends only weakly on the aspect ratio or the temperature. All plots are for perfect reflectors.

For this reason, we choose the dimension of the vector space proportional to the aspect ratio

$$\ell_{\text{dim}} = \left\lceil \eta \frac{R}{L} \right\rceil, \quad (5.33)$$

where η controls the error caused by the truncation of the vector space. Larger values of η yield a higher accuracy. From the high-temperature limit of Drude metals [51], one finds that the maximum value on the diagonal of the round-trip matrix is roughly obtained at $\ell \simeq m\sqrt{R/2L}$. Therefore, we restrict the vector space as $\ell_{\text{min}} \leq \ell \leq \ell_{\text{max}}$ with

$$\ell_{\text{min}} = \begin{cases} 1 & \text{for } m = 0 \\ \max\left(m, \text{round}\left(m\sqrt{\frac{R}{2L}} - \frac{\ell_{\text{dim}}}{2}\right)\right) & \text{for } m > 0 \end{cases} \quad (5.34)$$

and

$$\ell_{\text{max}} = \ell_{\text{min}} + \ell_{\text{dim}}. \quad (5.35)$$

Fig. 5.1 depicts the relative error

$$\Delta(\eta) = \frac{\mathcal{F}_{\text{ref}} - \mathcal{F}(\eta)}{\mathcal{F}_{\text{ref}}} \quad (5.36)$$

due to the truncation of the vector space as a function of η for perfect reflectors. The value of \mathcal{F}_{ref} has been obtained with a much higher accuracy using $\eta = 20$. As expected, the relative error decreases as a function of η and depends only weakly on temperature and the aspect ratio. The value of η required to achieve a certain relative error Δ can be

Δ	10^{-2}	10^{-3}	10^{-4}	10^{-5}	10^{-6}	10^{-7}	10^{-8}
η	2.8	4	5.2	6.4	7.6	8.8	10

Table 5.1: Required value of η in order to achieve the relative error Δ .

estimated from Fig. 5.1. A fit of the points corresponding to $T = 0$, $R/L = 200$ yields

$$\eta \approx -1.21 \log_{10}(\Delta) + 0.343. \quad (5.37)$$

The relative error Δ decreases by an order of magnitude when η is increased by about 1.2. For convenience, Tab. 5.1 lists the required value of η for some specific values of Δ . The results presented in this section are in agreement with that of Ref. [26]. The results found here also hold for more general materials than perfect reflectors.

For rather small aspect ratios $R/L \lesssim 10$, the semiclassical argument no longer holds and the estimate (5.37) becomes invalid. In this case it is preferable to use a fixed value of ℓ_{dim} . Since the numerical implementation is fast, one can simply use $\ell_{\text{dim}} = 100$ for $R/L \leq 10$.

5.6 Integration over k

We now turn to the numerical evaluation of the integrals (4.17) for $\xi > 0$. Employing the substitution $x = \kappa c/\xi$, the integrals (4.17) become

$$A_{\ell_1 \ell_2, p}^m(\alpha) = m^2 \int_1^\infty dx \frac{r_p}{x^2 - 1} e^{-\alpha x} P_{\ell_1}^m(x) P_{\ell_2}^m(x), \quad (5.38a)$$

$$B_{\ell_1 \ell_2, p}^m(\alpha) = \int_1^\infty dx r_p (x^2 - 1) e^{-\alpha x} P_{\ell_1}^{m'}(x) P_{\ell_2}^{m'}(x), \quad (5.38b)$$

$$C_{\ell_1 \ell_2, p}^m(\alpha) = m \int_1^\infty dx r_p e^{-\alpha x} P_{\ell_1}^m(x) P_{\ell_2}^{m'}(x), \quad (5.38c)$$

where we have introduced $\alpha = 2\xi\mathcal{L}/c$ for brevity. The Fresnel coefficients $r_p(i\xi, k)$ are now evaluated at $k = (\xi/c)(x^2 - 1)^{1/2}$. Since each matrix element of the round-trip operator contains two integrals, computing the full round-trip matrix requires the evaluation of $\mathcal{O}(\ell_{\text{dim}}^2)$ integrals.

In order to evaluate the integrals (5.38), we express the derivatives of the associated Legendre polynomials as linear combinations of associated Legendre polynomials and use Gaunt coefficients to express the integrals $A_{\ell_1 \ell_2, p'}^m$, $B_{\ell_1 \ell_2, p'}^m$ and $C_{\ell_1 \ell_2, p}^m$ as a combination of only $\mathcal{O}(\ell_{\text{dim}})$ different integrals. For the numerical integration, we use an adaptive Gauss–Kronrod quadrature formula. The quadrature works stable after the integrand is scaled appropriately. We show that the integrand has one maximum and discuss how the maximum and the width of the maximum can be estimated.

5.6.1 Reducing the number of integrals

We postpone the discussion of $m = 0$ to the end of this section and first discuss the case $m > 0$. Using the recurrence relation (A.8), the integrals (5.38) can be written as

$$A_{\ell_1 \ell_2, p}^m(\alpha) = m^2 J_{\ell_1, \ell_2, p}^m, \quad (5.39a)$$

$$\begin{aligned} B_{\ell_1 \ell_2, p}^m(\alpha) &= \frac{(\ell_1 + 1)(\ell_1 + m)(\ell_2 + 1)(\ell_2 + m)}{(2\ell_1 + 1)(2\ell_2 + 1)} J_{\ell_1 - 1, \ell_2 - 1, p}^m \\ &\quad - \frac{\ell_1(\ell_1 - m + 1)(\ell_2 + 1)(\ell_2 + m)}{(2\ell_1 + 1)(2\ell_2 + 1)} J_{\ell_1 + 1, \ell_2 - 1, p}^m \\ &\quad - \frac{(\ell_1 + 1)(\ell_1 + m)\ell_2(\ell_2 - m + 1)}{(2\ell_1 + 1)(2\ell_2 + 1)} J_{\ell_1 - 1, \ell_2 + 1, p}^m \\ &\quad + \frac{\ell_1(\ell_1 - m + 1)\ell_2(\ell_2 - m + 1)}{(2\ell_1 + 1)(2\ell_2 + 1)} J_{\ell_1 + 1, \ell_2 + 1, p}^m, \end{aligned} \quad (5.39b)$$

$$C_{\ell_1 \ell_2, p}^m(\alpha) = m \frac{\ell_2(\ell_2 - m + 1)}{\ell_2 + 1} J_{\ell_1, \ell_2 + 1, p}^m - m \frac{(\ell_2 + 1)(\ell_2 + m)}{\ell_2 + 1} J_{\ell_1, \ell_2 - 1, p}^m, \quad (5.39c)$$

with

$$J_{\ell_1 \ell_2, p}^m(\alpha) = \int_1^\infty dx \frac{r_p e^{-\alpha x}}{x^2 - 1} P_{\ell_1}^m(x) P_{\ell_2}^m(x). \quad (5.40)$$

The product of two associated Legendre polynomials can be expressed as a linear combination of associated Legendre polynomials

$$P_{\ell_1}^m(x) P_{\ell_2}^m(x) = \sum_{q=0}^{q_{\max}} c_q P_{\ell_1 + \ell_2 - 2q}^{2m}(x), \quad q_{\max} = \min\left(\ell_1, \ell_2, \frac{\ell_1 + \ell_2 - 2m}{2}\right), \quad (5.41)$$

where c_q denotes a Gaunt coefficient. The efficient computation of the Gaunt coefficients c_q using a recursive approach is described in Ref. [140]. Expressing the product of associated Legendre polynomials using (5.41), the integral $J_{\ell_1 \ell_2, p}^m$ becomes

$$J_{\ell_1 \ell_2, p}^m(\alpha) = \sum_{q=0}^{q_{\max}} c_q L_{\ell_1 + \ell_2 - 2q, p}^m(\alpha) \quad (5.42)$$

where we have defined

$$L_{n, p}^m(\alpha) = \int_1^\infty dx \frac{r_p e^{-\alpha x}}{x^2 - 1} P_n^{2m}(x) \quad \text{for } m > 0. \quad (5.43)$$

Therefore, the integrals $A_{\ell_1 \ell_2, p}^m$, $B_{\ell_1 \ell_2, p}^m$ and $C_{\ell_1 \ell_2, p}^m$ can be expressed as linear combinations of $\mathcal{O}(\ell_{\dim})$ integrals $L_{n, p}^m$.

For $m = 0$ every integral but

$$B_{\ell_1 \ell_2, p}^0(\alpha) = \int_1^\infty dx r_p (x^2 - 1) e^{-\alpha x} P_{\ell_1}'(x) P_{\ell_2}'(x) \quad (5.44)$$

vanishes. Using $P'_\ell(x) = \sqrt{x^2 - 1}P'_\ell^1(x)$, the integral becomes

$$B_{\ell_1 \ell_2, p}^0(\alpha) = \int_1^\infty dx r_p e^{-\alpha x} P_{\ell_1}^1(x) P_{\ell_2}^1(x) = J_{\ell_1 \ell_2, p}^0. \quad (5.45)$$

Using (5.42), the integral $J_{\ell_1 \ell_2, p}^0$ can be expressed as a linear combination of the integral

$$L_{n, p}^0(\alpha) = \int_1^\infty dx r_p e^{-\alpha x} P_n^2(x). \quad (5.46)$$

5.6.2 Shape of integrand and estimate of $L_{n, p}^m$

The shape of the integrand of $L_{n, p}^m$ and an estimate of the value of the integral are necessary to scale the integrand appropriately for a numerical integration. The integrand of $L_{n, p}^m$ typically has one peak. The position of the maximum can be computed using Newton's method to find the root of the derivative of the integrand. The width of the maximum and the value of $L_{n, p}^m$ may be estimated using the saddle-point approximation (3.19).

We now express the integrand in a form suitable for the saddle-point approximation

$$L_{n, p}^m(\alpha) = \int_1^\infty dx r_p e^{-f(x)} \quad (5.47)$$

with

$$f(x) = \begin{cases} \alpha x - \log(P_n^2(x)) & \text{for } m = 0 \\ \alpha x - \log(P_n^{2m}(x)) + \log(x^2 - 1) & \text{for } m > 0 \end{cases}. \quad (5.48)$$

The function $f(x)$ depends on n , m , and p , but to keep the notation simple we omit the indices. In the following, we assume that the Fresnel coefficient r_p varies only slowly with x . Also, we restrict ourselves to $m > 0$, the behavior of $L_{n, p}^m(\alpha)$ for $m = 0$ is very similar.

The first and second derivative of f with respect to x are given by

$$f'(x) = \alpha - \frac{d}{dx} \log(P_n^{2m}(x)) + \frac{2x}{x^2 - 1}, \quad (5.49a)$$

$$f''(x) = -\frac{d^2}{dx^2} \log(P_n^{2m}(x)) - \frac{2(x^2 + 1)}{(x^2 - 1)^2}. \quad (5.49b)$$

Due to (5.31) the second derivative is positive for $m > 1$ and $f(x)$ is strictly convex. Using (A.11) for the behavior of the associated Legendre polynomials for $x \rightarrow 1$ and $x \rightarrow \infty$, one can show that $f(x)$ has one unique minimum in $x \in (1, \infty)$ for $m > 1$. We will discuss the case $m = 1$ at the end of this section.

The position x_{\min} of the minimum of f is determined by $f'(x_{\min}) = 0$. This equation can be solved efficiently for x_{\min} using Newton's method [136, pp. 362–368]. In the vicinity of x_{\min} , Newton's method converges quadratically. In order to obtain a good initial guess

we use the asymptotic expansion [141]

$$P_n^m(x) \simeq \left(2\pi\sqrt{x^2-1}\right)^{-1/2} \frac{\Gamma(n+m+1)}{\Gamma\left(n+\frac{3}{2}\right)} e^{(n+\frac{1}{2})\operatorname{arccosh}x} \quad (5.50)$$

and find for the first derivative

$$f'(x) \simeq \alpha - \frac{n+\frac{1}{2}}{\sqrt{x^2-1}} + \frac{5}{2} \frac{x}{x^2-1} \stackrel{!}{=} 0. \quad (5.51)$$

With the further approximation $x^2 - 1 \approx x^2$ valid for $x_{\min} \gg 1$, the equation can be solved and we find

$$x_0 = \frac{n-2}{\alpha}. \quad (5.52)$$

If $x_0 \lesssim 1$, the assumption $x_{\min} \gg 1$ breaks down and another initial guess has to be chosen. In this case $x_0 = 1 + n^2/2\alpha^2$ gives a good estimate.

Using the saddle-point method, we find the approximation

$$L_{n,p}^m \approx r_p \sqrt{\frac{2\pi}{f''(x_{\min})}} e^{-f(x_{\min})}, \quad (5.53)$$

where the Fresnel coefficient $r_p(i\xi, k)$ is evaluated at $k = (\xi^2/c^2)\sqrt{x_{\min}^2 - 1}$. The width of the peak such that the integrand at $x = x_{\min} \pm \Delta(\epsilon)$ is approximately ϵ times the value of the maximum, is given by

$$\Delta(\epsilon) \simeq -\frac{\log \epsilon}{\sqrt{f''(x_{\min})}}. \quad (5.54)$$

Fig. 5.2 depicts the integrand of $L_{n,p}^m$ for different values of n, m, α , for $p = \text{TM}$ and perfect reflectors. The solid line corresponds to the integrand of $L_{n,p}^m$, the dashed line corresponds to the Gaussian approximation used by the saddle-point method. For the examples shown in Fig. 5.2a–c, the approximation gives good estimates of the behavior of the integrands. Moreover, one can check that the estimate x_0 of the maximum of the integrand is good in all cases.

For $m = 1$ the integral becomes

$$L_{n,p}^1(\alpha) = \int_1^\infty dx \frac{r_p}{x^2-1} e^{-\alpha x} P_n^2(x) = \int_1^\infty dx r_p g(x), \quad g(x) = e^{-\alpha x} P_n''(x). \quad (5.55)$$

We assume that the Fresnel coefficient r_p varies slowly with respect to x and study the behavior of $g(x)$. As all derivatives of ordinary Legendre polynomials are positive for $x \geq 1$, the function $g(x)$ is positive in the integration interval. For $x \rightarrow \infty$ the integrand vanishes, $g(x \rightarrow \infty) \rightarrow 0$, and in the limit $x \rightarrow 1$ the integrand goes to a constant $g(1) =$

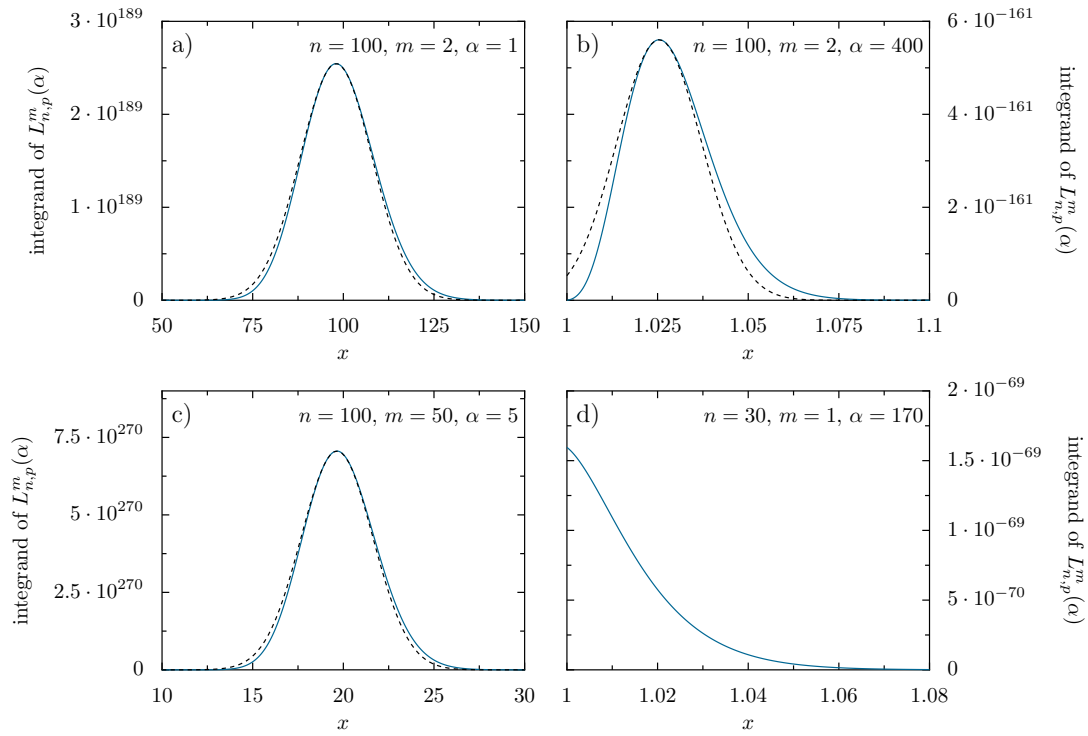


Figure 5.2: Integrand of $L_{n,p}^m$ for perfect reflectors, $p = \text{TM}$, and different values of n , m , and α . The solid line corresponds to the integrand, the dashed line corresponds to the Gaussian approximation.

$e^{-\alpha} P_n''(1)$. The derivative of g is given by

$$g'(x) = \frac{d}{dx} (e^{-\alpha x} P_n''(x)) = e^{-\alpha x} (-\alpha P_n''(x) + P_n'''(x)). \quad (5.56)$$

Since $-\alpha P_n''(x)$ is monotonically decreasing with x and $P_n'''(x)$ is monotonically increasing with x , the function g has at most one local maximum in the integration interval. The integrand attains its maximum at $x = 1$ if $g'(1) \leq 0$, otherwise $g(x)$ has one local maximum in $x \in (1, \infty)$. With the first and second derivative of the Legendre polynomials at $x = 1$ (A.17)

$$P_n''(1) = \frac{(n-1)n(n+1)(n+2)}{8}, \quad (5.57a)$$

$$P_n'''(1) = \frac{(n-2)(n-1)n(n+1)(n+2)(n+3)}{48}, \quad (5.57b)$$

one finds that $g'(1) \leq 0$ for $(n-2)(n+3)/6 \leq \alpha$. In this case, the integrand attains its maximum at $x = 1$ and $g(x)$ is a monotonically decreasing function. In all other cases, the integrand of $L_{n,p}^1$ has exactly one local maximum. Fig. 5.2d shows the integrand of $L_{n,p}^1$ for a case when the integrand is a monotonically decreasing function.

5.6.3 Numerical integration

In order to evaluate the integral $L_{n,p}^m$ numerically, we split the range of integration in three sub-intervals $[1, a]$, $[a, b]$ and $[b, \infty)$. The borders a and b are chosen such that the main contribution to the integral comes from the interval $[a, b]$. Also, with the approximation $A \approx L_{n,p}^m$ obtained using the saddle-point method, we can express the integral as

$$L_{n,p}^m = A \left(\int_1^a dx r_p e^{-f(x)-\log A} + \int_a^b dx r_p e^{-f(x)-\log A} + \int_b^\infty dx r_p e^{-f(x)-\log A} \right). \quad (5.58)$$

This representation is suitable for a numerical evaluation. The integrals are integrated using an adaptive integration scheme. We use CQUADPACK [142] which is a port of the FORTRAN 77 library QUADPACK [143] to C. For the second integral, an adaptive quadrature based on 21-point Gauss-Kronrod quadrature within each sub-interval is used. For the intervals $(1, a)$ and (b, ∞) , it is sufficient to use a lower point adaptive Gauss-Kronrod quadrature. Also, for the integral (b, ∞) it is useful to make the substitution $z = \alpha x$, so that the integrand decreases of order $\mathcal{O}(1)$.

5.6.4 Analytical results for $L_{n,p}^m(\alpha)$

For perfect reflectors the Fresnel coefficients are mere numbers and the integrals $L_{n,p}^m$ can be solved analytically. However, it seems that no simple closed form for arbitrary values of n and m exists. Here, we list some analytical results that are especially useful for testing the numerical integration.

For $m = 1$ we find

$$\begin{aligned} L_{n,p}^1(\alpha) &= r_p \int_1^\infty dx \frac{e^{-\alpha x}}{x^2 - 1} P_n^2(x) = r_p \int_1^\infty dx e^{-\alpha x} P_n''(x) \\ &= r_p \left[\alpha^2 \int_1^\infty dx e^{-\alpha x} P_n(x) - e^{-\alpha} (P_n'(1) + \alpha P_n(1)) \right]. \end{aligned} \quad (5.59)$$

The Legendre polynomial and its derivative evaluated at $x = 1$ are given by (A.17), the integral in the last line of (5.59) is listed in Ref. [144, 7.141], and thus

$$L_{n,p}^1(\alpha) = r_p \left[\alpha^2 \sqrt{\frac{2}{\pi\alpha}} K_{n+1/2}(\alpha) - e^{-\alpha} \left(\alpha + \frac{n(n+1)}{2} \right) \right]. \quad (5.60)$$

With this result the integral $L_{n,p}^0$ can also be evaluated:

$$\begin{aligned} L_{n,p}^0(\alpha) &= r_p \int_1^\infty dx (x^2 - 1) e^{-\alpha x} P_n''(x) = (\partial_\alpha^2 - 1) L_{n,p}^1(\alpha) \\ &= r_p \left[2e^{-\alpha} + \sqrt{\frac{2}{\pi\alpha}} \left[(n+1)(n+2) K_{n+1/2}(\alpha) - 2\alpha K_{n+3/2}(\alpha) \right] \right] \end{aligned} \quad (5.61)$$

Using

$$P_m^m(x) = \frac{(2m)!}{2^m m!} (x^2 - 1)^{m/2}, \quad (5.62)$$

the integral $L_{2m,p}^m$ yields

$$L_{2m,p}^m(\alpha) = r_p(m-1)! \frac{(4m)!}{4^m (2m)!} \sqrt{\frac{\alpha}{2\pi}} \left(\frac{2}{\alpha}\right)^m K_{m-1/2}(\alpha). \quad (5.63)$$

In principle all integrals can be evaluated analytically, but the expressions become more and more cumbersome.

5.7 Computation of the determinant

The determinants of the scattering matrices $\mathbb{1} - \widehat{\mathcal{M}}^m$ can be evaluated efficiently using the algorithm suited for hierarchical off-diagonal low-rank (HODLR) matrices [125] described in section 4.6. We use the public implementation [130] of the algorithm written by the authors of Ref. [125]. The computation of the determinant might be sped up further using a version of the algorithm adapted to symmetric positive-definite hierarchical matrices [128]. The authors of Ref. [128] also provide a public implementation [145]. However, due to lack of time, it has been not possible yet to adapt the numerics to this algorithm.

In order to test the accuracy of the HODLR approach, the numerical implementation also supports the computation of the determinants using Cholesky, LU or QR decomposition. The QR and LU decomposition work for general matrices and do not require specific properties of the matrix. In general, a LU decomposition is about twice as fast as a QR decomposition, while a Cholesky decomposition of a symmetric and positive definite matrix is about twice as fast as an LU decomposition. The Cholesky decomposition has the form

$$\mathbb{1} - \widehat{\mathcal{M}}^m(\xi) = L^T L, \quad (5.64)$$

where L is a lower triangular matrix. After factorization, the logarithm of the determinant can be computed readily

$$\log \det \left(\mathbb{1} - \widehat{\mathcal{M}}^m \right) = \log \det (L^T L) = 2 \sum_j \log (L_{jj}). \quad (5.65)$$

The computation using QR or LU decomposition works similarly. We use the implementation of the QR, LU and Cholesky decomposition provided by LAPACK [131].

If the matrix elements of the round-trip operator are small, $\widehat{\mathcal{M}}_{\ell_1 \ell_2}^m(P_1, P_2) \ll 1$, computing the diagonal elements of the scattering matrix $\mathbb{1} - \widehat{\mathcal{M}}^m$ might result in a loss of significance.

To avoid this problem, we expand the logarithm in a Mercator series

$$\log \det(\mathbb{1} - A) = \text{tr} \log(\mathbb{1} - A) = - \sum_{j=1}^{\infty} \frac{\text{tr}(A^j)}{j} = - \text{tr} A + R, \quad (5.66)$$

where we have introduced the abbreviation $A = \widehat{\mathcal{M}}^m$. Here, A^j denotes the j th matrix power of A . The trace of A provides an approximation for the logarithm of the determinant with the remainder given by

$$R = - \sum_{j=2}^{\infty} \frac{\text{tr}(A^j)}{j}. \quad (5.67)$$

As all eigenvalues λ_j of A are positive, the contribution of R is negative and the trace gives an upper bound

$$\log \det(\mathbb{1} - A) \leq - \text{tr} A. \quad (5.68)$$

Moreover, since the eigenvalues are bounded by $0 \leq \lambda_j \leq 1$, it follows that $\text{tr}(A^j) \leq (\text{tr} A)^j$. Thus the remainder R can be estimated by

$$|R| = \sum_{j=2}^{\infty} \frac{\text{tr}(A^j)}{j} \leq \sum_{j=2}^{\infty} \frac{(\text{tr} A)^j}{j} < \sum_{j=2}^{\infty} \frac{(\text{tr} A)^j}{2} = \frac{1}{2} \frac{(\text{tr} A)^2}{1 - \text{tr} A}. \quad (5.69)$$

For $\text{tr} A \ll 1$, the relative error using the trace approximation is given by $\text{tr} A/2$. This means that if the trace is sufficiently small, the trace approximation can be used to avoid a loss of significance and to speed up the computation.

5.8 Differentiation

The scattering approach provides an exact formula for the Casimir free interaction energy. Experimentally, the Casimir force

$$F = - \frac{\partial \mathcal{F}}{\partial L} \quad (5.70)$$

and the Casimir force gradient

$$F' = - \frac{\partial^2 \mathcal{F}}{\partial L^2} \quad (5.71)$$

are more accessible. In order to compute the force and the force gradient, one has to derive the free energy with respect to the separation L .

The derivative of the logarithm of the determinant of a matrix A is given by

$$\frac{\partial}{\partial x} \log \det A = \frac{\partial}{\partial x} \text{tr} \log A = \text{tr} \left(\frac{\partial}{\partial x} \log A \right) = \text{tr} (A^{-1} A') \quad (5.72)$$

where $(A')_{jk} = \frac{\partial}{\partial x} A_{jk}$. Similarly, the second derivative is given by

$$\frac{\partial^2}{\partial x^2} \log \det A = \text{tr} (A^{-1} A'' + A' A^{-1} A' A^{-1}) . \quad (5.73)$$

This method is in principle well suited for hierarchical matrices: After the factorization of A , both the matrix inversion and the matrix product can be computed efficiently.

Unfortunately, the HODLR library [130] does not support matrix inversion. Instead, we evaluate the free energy \mathcal{F} on an equidistant grid and use finite difference formulae [146] to compute the first and second derivative numerically. Unfortunately, finite difference formulae are ill-conditioned. In order to achieve a good accuracy for the Casimir force and force gradient, the free energy needs to be computed with high accuracy and one needs to use a difference formula of high order. We mainly use the symmetric finite difference formulae of orders 6 and 8. A detailed discussion about difficulties and errors of numerical differentiation can be found in Ref. [136, pp. 186–189].

5.9 Numerical tests

The numerical evaluation of the Casimir free energy in the plane-sphere geometry is a complicated task. On the one hand, the implementation needs to be fast and efficient to reach large aspect ratios. On the other hand, the implementation must ensure that results are correct within controllable error bounds for all parameters of interest. In order to ensure that the numerical implementation works correctly, the code has been tested thoroughly using unit tests, and numerical results have been compared with results known in the literature.

We use unit tests to check simple functions of the numerical implementation. In particular, the Fresnel coefficients (810), the Mie coefficients (910), the modified Bessel functions (572), and the associated Legendre functions (1412) are tested against high-accuracy results obtained using Mathematica [147]. Here, the number in brackets denotes the number of unit tests. Whenever the code was modified, the unit tests were run to make sure that the changes did not break any of these functions.

The numerical integration of $L_{n,p}^m$ has been tested against the analytical results presented in section 5.6.4. The computation of the determinant using the HODLR approach has been compared with results obtained using the Cholesky decomposition. The high-temperature limit for the plasma model has been tested against a much simpler implementation written in Python.

In addition, we have compared our numerical data with analytical and numerical results known in the literature: For small aspect ratios and perfect reflectors, the numerical results agree with the analytical long-distance expansion [26, 148]. As shown in Fig. 5.3, we find

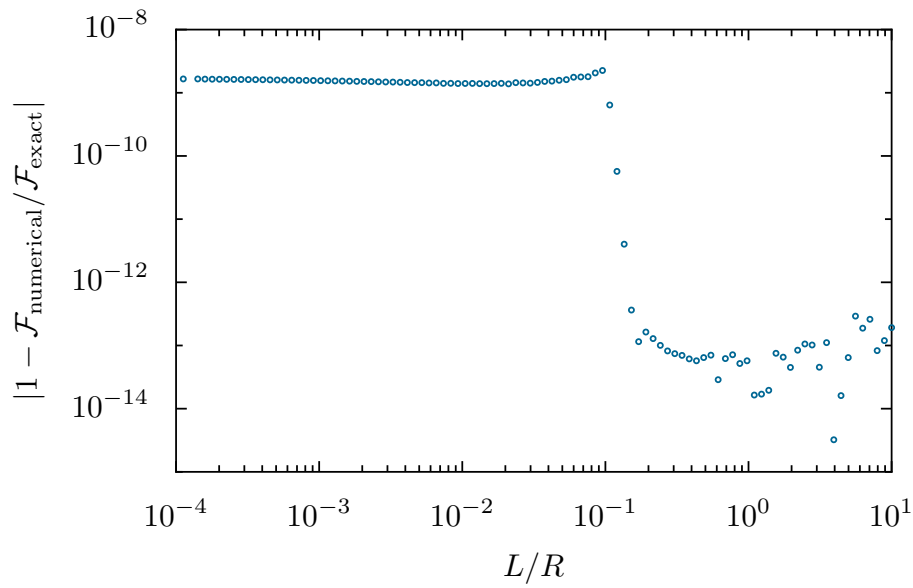


Figure 5.3: Relative error of the numerically computed free energy $\mathcal{F}_{\text{numerical}}$ for Drude metals in the high-temperature limit as a function of the inverse aspect ratio. The numerical data are compared with the exact expression for the free energy $\mathcal{F}_{\text{exact}}$ given in Ref. [51]. The truncation of the vector space was chosen as $\ell_{\text{dim}} = \max(100, \eta R/L)$ with $\eta = 10$. For $L/R \ll 10^{-1}$, the error is dominated by the truncation of the vector space which is of the order 10^{-9} in agreement with the results presented in section 5.5. For $L/R \gg 10^{-1}$, the numerical error is dominated by the computation of the determinant using the algorithm for HODLR matrices, cf. section 4.6. The accuracy of the computation of the determinant in the numerical implementation is chosen as 10^{-13} .

excellent agreement with the exact analytical result for the Drude model in the high-temperature limit [51]. Moreover, we also find the first leading correction to the PFA for perfect reflectors in the high-temperature limit [52]. For zero temperature, our numerical results agree with the leading correction to the PFA for perfect reflectors [49, 101], as well as the Drude and plasma model [50], cf. chapter 6. Finally, for the Drude prescription at room temperature, our results presented in chapter 7 are consistent with those obtained from the derivative expansion [102, 149].

Our careful testing also revealed problems in other libraries: We have found bugs in `mpmath`¹ [150], `CQUADPACK`^{2,3,4} [142], and the `HODLR` library^{5,6,7} [130].

¹<https://github.com/fredrik-johansson/mpmath/issues/331>

²<https://github.com/ESSS/cquadpack/pull/5>

³<https://github.com/ESSS/cquadpack/pull/6>

⁴<https://github.com/ESSS/cquadpack/pull/8>

⁵<https://github.com/sivaramambikasaran/HODLR/pull/11>

⁶<https://github.com/sivaramambikasaran/HODLR/issues/13>

⁷<https://github.com/sivaramambikasaran/HODLR/issues/14>

Chapter 6

Corrections beyond the proximity force approximation at zero temperature

In the last two chapters, we have presented the ideas and concepts that make it possible to extend the range of numerically accessible aspect ratios to $R/L \sim 10^3$. This allows us to compare numerically exact results with results obtained using the proximity force approximation (PFA), and to assess deviations from it for aspect ratios used in typical experiments. While we consider the experimentally important configuration of gold metals at ambient temperature in the next chapter, we here focus on the zero temperature limit.

The Casimir interaction is caused by a combination of zero-point fluctuations and thermal fluctuations. For non-zero temperature, thermal fluctuations cause logarithmic corrections to the PFA for perfect reflectors and metals described by the Drude and the plasma model [51, 52]. For $T = 0$, the leading order correction to the PFA has been obtained by means of an asymptotic expansion of the scattering formula [49, 50], and using the derivative expansion [101]. It turns out that the first correction to the PFA result is linear in the inverse aspect ratio L/R . As we will show in the following, for perfect reflectors and metals described by the Drude and the plasma model, the next-to-leading-order correction to the PFA is proportional to $(L/R)^{3/2}$.

6.1 Perfect reflectors

For perfect reflectors at zero temperature, the only length scales are the separation L between plane and sphere, and the radius R of the sphere. The Casimir energy E multiplied by the separation L is a function that only depends on the aspect ratio R/L . This can be verified from the scattering formula (4.5) with the matrix elements of the round-trip operator in the multipole basis (4.16), (4.17). Within the proximity force approximation

(3.35), the Casimir energy is given by

$$E_{\text{PFA}} = -\frac{\hbar c \pi^3 R}{720 L^2}. \quad (6.1)$$

The first correction to the PFA for perfect reflectors was calculated by Bordag and Nikolaev [48]. They found a linear and logarithmic corrections in L/R to the PFA result. However, due to a sign error, their result was incorrect. In a recalculation Teo together with the authors of Ref. [48] found a linear correction [49]

$$E = E_{\text{PFA}} \left(1 + \theta_1 \frac{L}{R} + \dots \right), \quad \theta_1 = \frac{1}{3} - \frac{20}{\pi^2} \approx -1.69309. \quad (6.2)$$

The linear correction also agrees with a result obtained using the derivative expansion [101]. Using a Padé approximation of numerical data at large distances together with the linear correction (6.2) at small separations, the authors of Ref. [101] concluded

$$E = E_{\text{PFA}} \left(1 + \theta_1 \frac{L}{R} + \theta_2 \left(\frac{L}{R} \right)^2 \log \left(\frac{L}{R} \right) + \dots \right), \quad \theta_2 \approx -4.52, \quad (6.3)$$

for the correction to the PFA.

In Fig. 6.1a, we plot the correction $1 - E/E_{\text{PFA}}$ to the PFA as a function of the inverse aspect ratio L/R . The data have been computed with a truncation of the vector space given by $\ell_{\text{dim}} = \eta R/L$ and $\eta = 10$, cf. section 5.5. For the largest aspect ratio $R/L = 4000$ shown in the figure, more than 56 000 determinants of dimension $80\,000 \times 80\,000$ have been computed. The numerical error of the data is dominated by the numerical integration over the Matsubara frequencies ξ , and for $L/R \lesssim 0.002$ the error is of the order 5×10^{-8} . As expected, the data approach the linear correction given by (6.2) for large aspect ratios.

In Fig. 6.1b, we plot the correction to the PFA, but now we also subtract the linear term $\theta_1 L/R$. The circles and triangles correspond to numerical results, while the dashed line represents the correction (6.3) obtained in Ref. [101] using a Padé approximation. The agreement of the dashed line with our data is poor. As the slopes of the numerical data and the dashed line do not coincide, the mismatch is independent of the value of θ_2 , suggesting that the correction is not of the form (6.3). In addition, we have considered terms of the form $\theta_2 (L/R)^n \log^m(L/R)$ with integers $0 \leq n, m \leq 5$ for the next-to-leading-order correction to the PFA. However, all functions yield poor fits of the numerical data, suggesting that the correction has a different form.

In order to find the correct form of the correction to the PFA, we analyze the power law of the numerical points in Fig. 6.1b. It turns out that for small values of L/R , the data are well described by $\propto (L/R)^{3/2}$. This suggests an expansion of the correction in powers of

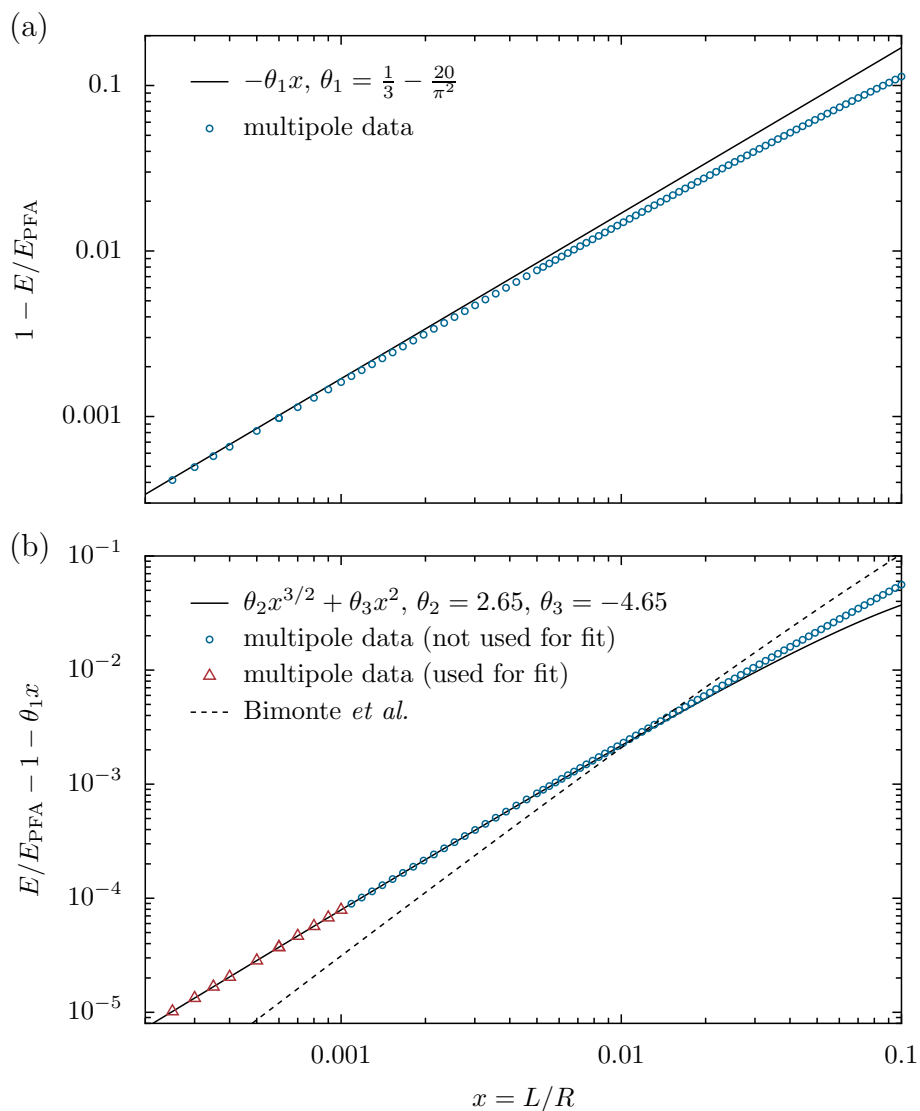


Figure 6.1: (a) Correction to the PFA for perfect reflectors as a function of the inverse aspect ratio L/R at zero temperature. Circles correspond to numerical data, the full line is the linear correction (6.2) to the PFA. For large aspect ratios, the numerical points approach the linear correction. (b) Same plot as in (a) but with the linear correction subtracted. Circles and triangles correspond to numerical data, the dashed line is the correction (6.3) obtained in Ref. [101] using a Padé approximation. The full line corresponds to a fit using the data points shown as red triangles. The numerical error for the points $L/R \leq 0.002$ is of the order 5×10^{-8} .

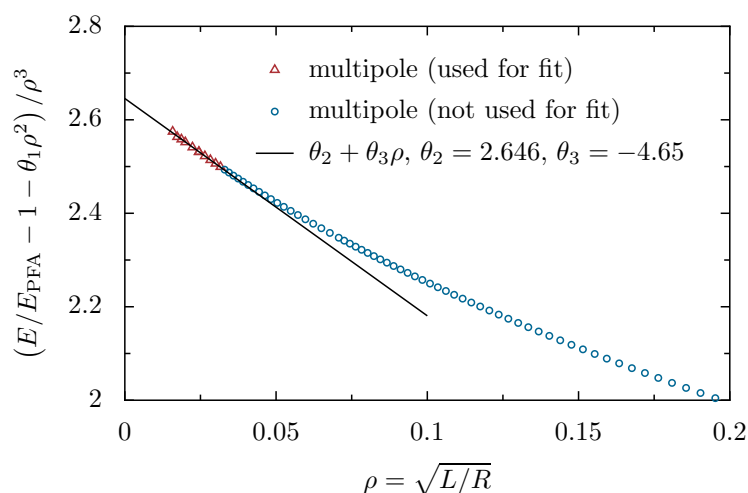


Figure 6.2: Corrections to the PFA beyond the linear term divided by $(L/R)^{3/2}$ as a function of $\rho = (L/R)^{1/2}$ for perfect reflectors. The circles and triangles correspond to numerical data. The full line is a linear fit using the red triangles.

$$(L/R)^{1/2}, \quad \frac{E}{E_{\text{PFA}}} = 1 + \theta_1 x + \theta_2 x^{3/2} + \theta_3 x^2 + \dots, \quad x = \frac{L}{R}. \quad (6.4)$$

After rearranging the terms and dividing by $x^{3/2}$

$$\frac{1}{\rho^3} \left(\frac{E}{E_{\text{PFA}}} - 1 - \theta_1 \rho^2 \right) = \theta_2 + \theta_3 \rho + \dots, \quad \rho = \sqrt{\frac{L}{R}}, \quad (6.5)$$

the parameters θ_2 and θ_3 can be obtained using a linear fit. There are two sources of error for the fit, the truncation error caused by neglecting higher order terms, and the numerical error due to the finite accuracy of the numerics. As the numerical error is small, we use points with large aspect ratios in order to reduce the truncation error. In Fig. 6.2, we plot the left-hand side of (6.5) as a function of ρ . If the next-to-leading order correction to the PFA is proportional to $x^{3/2}$, the data should approach a finite value in the limit $x \rightarrow 0$. In contrast, if the correction is not of the form (6.4), the data should approach either 0 or diverge. As can be seen in Fig. 6.2, the data in fact approach a non-zero constant. From a fit using the points $L/R \leq 0.001$, we find for the coefficients

$$\theta_2 = 2.65, \quad \theta_3 = -4.65. \quad (6.6)$$

Due to numerical and truncation errors, the values of θ_2 and θ_3 slightly depend on the points chosen for the fit. From fits with different degrees and using different points, we find that θ_2 varies up to about 2%, and θ_3 varies up to about 15%. A more accurate determination of the coefficients requires data points at larger aspect ratios in order to reduce the truncation error.

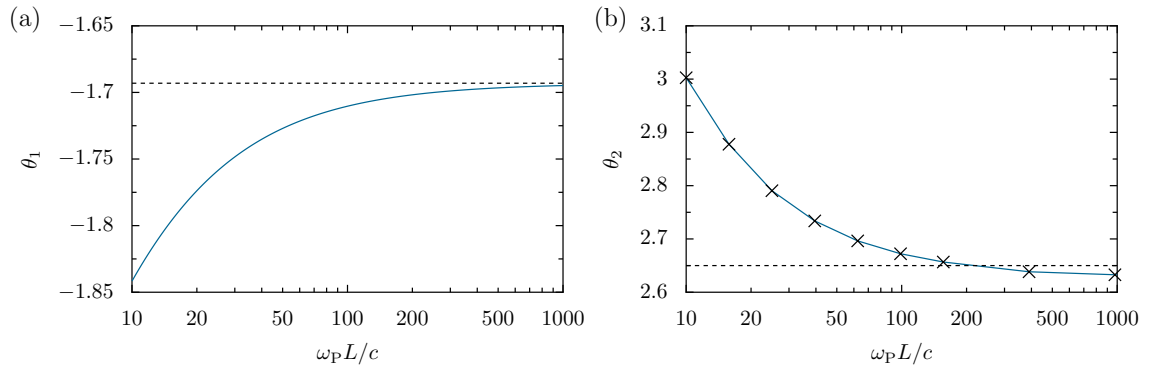


Figure 6.3: (a) Linear correction θ_1 as a function of $\omega_P L/c$ for the plasma model computed using the formulae given in Ref. [50]. The dashed line corresponds to the limit of perfect reflectors, $\theta_1 = 1/3 - 20/\pi^2$. (b) The coefficient θ_2 of the next-to-leading order correction to the PFA for the plasma model as a function of $\omega_P L/c$ obtained using our numerics. The crosses have been computed using fits. The dashed line corresponds to the limit of perfect reflectors found in section 6.1, $\theta_2 \approx 2.65$. For large values of $\omega_P L/c$, the points approach ≈ 2.63 which differs slightly from the result for perfect reflectors because of numerical errors. The solid line serves as a guide for the eye.

6.2 Plasma model

The assumption of perfect reflectors is a very idealized one. We now study whether the next-to-leading order correction to the PFA is still of the form $\theta_2 x^{3/2}$ for more realistic dielectric functions. The simplest model respecting the high-frequency transparency of metals is the plasma model. For the plasma model, the coefficient θ_1 depends only on $\omega_P L/c$ [50]. In the limit $\omega_P \rightarrow \infty$, the coefficient θ_1 approaches the result for perfect reflectors, $\theta_1 \rightarrow 1/3 - 20/\pi^2$, and for arbitrary values of $\omega_P L/c$, the value of θ_1 has been derived analytically by Teo [50]. Fig. 6.3a depicts the coefficient θ_1 as a function of $\omega_P L/c$. The dashed line in the figure corresponds to the value of θ_1 for perfect reflectors, i.e., for $\omega_P \rightarrow \infty$. Interestingly, the leading order correction θ_1 to the PFA is minimal for perfect reflectors.

In Fig. 6.4, we plot the correction to the PFA beyond the linear term as a function of the inverse aspect ratio L/R for $\omega_P L/c = 25$. The circles and triangles are numerical data, the full line corresponds to the function $\theta_2 x^{3/2} + \theta_3 x^2$. As in the case of perfect reflectors, the coefficients θ_2 and θ_3 have been determined using a fit of the numerical points with $L/R \leq 0.001$. In both cases, the fits are in good agreement with the numerical data for about two orders of magnitude. For $L/R \gtrsim 0.05$, higher corrections become important and the numerical data deviate from the fit. Most importantly, the Casimir energy is also of the form (6.4) for the plasma model, and the correction $\theta_2 x^{3/2}$ is not a peculiarity of idealized boundary conditions.

Fig. 6.3b depicts the coefficient θ_2 as a function of $\omega_P L/c$. Each data point has been obtained using a fit as described above. The points used for the fit for $\omega_P L/c = 25$ are shown

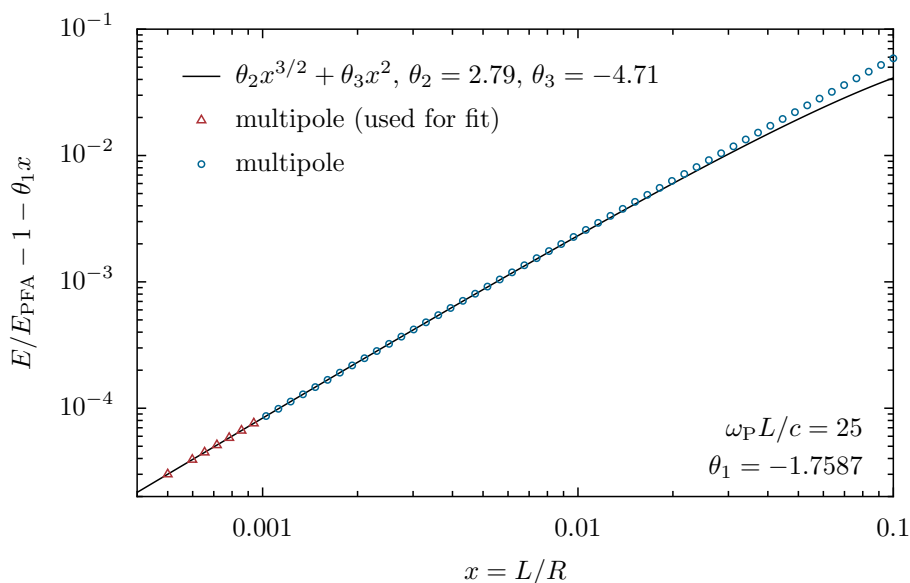


Figure 6.4: Corrections to the PFA for the plasma model beyond the linear term as a function of $x = L/R$ for $\omega_P L/c = 25$. Circles and triangles correspond to numerical data, the full line is a fit using the red triangles. The value of the linear correction θ_1 has been obtained using the formulae in Ref. [50].

as red triangles in Fig. 6.4, for all other values of $\omega_P L/c$, we have used the points

$$L/R = \{0.001, 0.0009, 0.0008, 0.0007, 0.0006\}. \quad (6.7)$$

For $\omega_P \rightarrow \infty$ the coefficient θ_2 should approach the value of perfect reflectors plotted as dashed line in Fig. 6.3b. In fact, the points do not exactly approach the result for perfect reflectors. While we found $\theta_2 \approx 2.65$ in the last section, the points in Fig. 6.3b approach $\theta_2 \approx 2.63$ in the limit $\omega_P L/c \rightarrow \infty$. The reason for this is that the values of θ_2 have been obtained with fits using points with smaller aspect ratios than in the case of perfect reflectors. This causes a larger error of θ_2 , thus explaining the slight mismatch in Fig. 6.3b.

6.3 Drude model

In the Drude model, the coefficient θ_1 depends on the separation L , the plasma frequency ω_P , and the relaxation frequency γ . However, θ_1 is independent of the radius R . For this reason, we plot in Fig. 6.5 the correction to the PFA beyond the linear term divided by $x^{3/2}$ for fixed separation $L = 150$ nm as a function of $\rho = \sqrt{x}$. The plasma frequency ω_P and the relaxation frequency γ correspond to gold, $\hbar\omega_P = 9$ eV and $\hbar\gamma = 35$ meV. The value of γ is given for room temperature, in general the relaxation frequency depends on temperature [151, 152]. The points take on a local maximum at $\rho \approx 0.047$. A linear fit of the three points with largest aspect ratio yields $\theta_2 \approx 2.12$. As the points used for the fit are rather close to the maximum, the actual value of θ_2 is probably a bit smaller than 2.12.

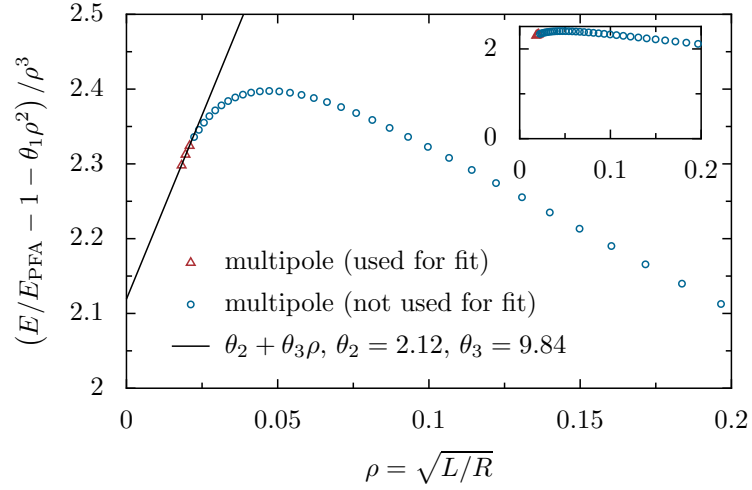


Figure 6.5: Corrections to the PFA beyond the linear term divided by ρ^3 as a function of $\rho = (L/R)^{1/2}$ for the Drude model. The circles and triangles correspond to numerical data. The full line is a linear fit using the red triangles. The data have been obtained for a fixed separation $L = 150$ nm varying the radius R . The parameters for the Drude model correspond to typical values of gold, $\hbar\omega_P = 9$ eV and $\hbar\gamma = 35$ meV. The value of $\theta_1 \approx -1.8325715$ has been obtained using the formulae in Ref. [50]. The inset shows the same data with a different scale for the y -axis.

The inset in Fig. 6.5 depicts the same data but with a different scale for the y -axis. This representation emphasizes the fact that it is unlikely that the points approach 0 in the limit $L/R \rightarrow 0$. We therefore conclude that the next-to-leading-order correction to the PFA in the Drude model has the same form (6.4) as in the plasma model or for perfect reflectors.

The fact that for zero temperature the next-to-leading order correction to the PFA scales as $x^{3/2}$ is remarkable. The expansion of the Casimir energy for scalar fields [98] and for the electromagnetic field [48–50] is actually an asymptotic expansion in powers of \sqrt{x} . For symmetry reasons, the first correction to the PFA is not proportional to \sqrt{x} but linear in x [48, 98]. The integrands containing \sqrt{x} terms are odd in the integration variable. Since the integration limits are symmetric, the respective integrals vanish. Nevertheless, it is unclear why this symmetry argument no longer holds for higher corrections. Commonly, it is believed that the correction following the linear term is either quadratic x^2 or of logarithmic form $x^n \log x$ [100–102]. Both terms are, however, incompatible with our numerical data.

Yet another method to derive corrections to the PFA is provided by the derivative expansion [53, 100]. The derivative expansion describes the Casimir energy as a functional of the shape of the interacting bodies. The first correction to the PFA can then be obtained by the derivatives describing the shape of the surfaces, as has been done for the plane-sphere geometry [101]. In principle, this method also allows one to derive higher corrections taking into account higher derivatives. However, the derivative expansion incorrectly predicts a term proportional to x^2 . The failure of the derivative expansion gives some hints for

possible physical reasons for the occurrence of the $x^{3/2}$ correction. The derivative expansion considers only the hemisphere facing the plane and contains only local information about the geometry. This suggests that the correction $\theta_2 x^{3/2}$ might be caused by non-local effects [100] and/or due to the hemisphere averted from the plate.

In the next chapter, we study the corrections to the PFA for real metals at room temperature. In particular, we consider gold and compare our numerical results with experimental data.

Chapter 7

Comparison with experiments

In this chapter, we calculate the Casimir force and the force gradient for gold surfaces at room temperature with parameters corresponding to the experiments reported in Refs. [9, 10, 38, 42]. We compare our numerically exact results with those obtained within the proximity force approximation (PFA) employed in the analysis of all Casimir force experiments reported in the literature so far. For the zero Matsubara frequency, we use both the Drude model and the dissipationless plasma model. We find that the correction to the PFA is too small to explain the discrepancy between the experimental data and the PFA result based on the Drude model.

In Ref. [38], the force-gradient variation with the sphere radius R was probed experimentally, and an upper bound for the correction was derived. It turns out that for the plasma model, the corrections to the PFA lie well outside the experimental bound obtained. The corresponding corrections based on the Drude model are significantly smaller but still in violation of the experimental bound for small distances between plane and sphere.

Although the PFA provides the correct leading divergence in the limit of large aspect ratios $R/L \rightarrow \infty$, as shown in chapter 3, the magnitude of the correction to the PFA under real experimental conditions was not known until now. On the theoretical side, recent advances were based either on asymptotic expansions valid in the particular case of perfect reflectors at zero temperature [49] or on the derivative expansion approach [100–102]. The latter relies on a re-summation of the perturbative expansion around the planar geometry. Its application to compact objects like the sphere thus relies on the assumption that only the hemisphere facing the plate contributes when $R/L \gg 1$ [53]. Moreover, the derivative expansion requires analyticity of the perturbative kernel, a condition not met for the zero-frequency contribution when taking the plasma model [153].

None of these approaches allow for a direct comparison with the experimental bound derived in Ref. [38], since they provide only the leading-order correction to the PFA result. In fact, the next-to-leading-order correction might be comparable to the leading-order one for typical experimental aspect ratios $R/L \sim 10^3$, as for instance in the case of Drude

metals at high temperatures [51]. A recent proposal combines the leading-order correction for the positive Matsubara frequencies and the exact result for the zero frequency contribution in the case of Drude metals [149]. However, no such result is available for the plasma model.

7.1 Drude and plasma prescription

We will focus on gold surfaces [9, 10, 38, 42] at room temperature $T = 295$ K. The permittivity of gold at imaginary frequencies entering the reflection coefficients can be derived from tabulated optical data [79] as explained in section 2.6. For gold, we find from the optical data the plasma frequency $\hbar\omega_P = 9$ eV and the relaxation frequency $\hbar\gamma = 30$ meV which, differ slightly from the values $\hbar\omega_P = 8.9$ eV and $\hbar\gamma = 35.7$ meV used to analyze the experiment in Ref. [9]. As shown in Fig. 7.1, the frequency range covered by this procedure includes all required Matsubara frequencies ξ_n except for $n = 0$.

The treatment of the zero frequency is a matter of ongoing debate in the Casimir community. Commonly, experiments have been analyzed using either the Drude prescription or the plasma prescription. In both prescriptions, the dielectric function obtained from the tabulated optical data is used for all Matsubara frequencies but $\xi_0 = 0$. For the zero frequency, either the Drude or the plasma model as introduced in section 2.5 is employed.

Since for $n = 0$ no polarization mixing occurs [154], TM and TE modes contribute independently. The TM mode for both models is perfectly reflected by the plane and the sphere, and thus its contribution to the Casimir free energy only depends on the aspect ratio R/L . In contrast, the contribution for the TE mode depends on the model chosen. While for the Drude model no contribution arises [73], the contribution for the plasma model is non-vanishing and also depends on the plasma frequency ω_P [122]. As a consequence, the difference between the Drude and the plasma prescription arises merely from the TE mode at zero frequency.

Whereas the Drude model accounts for dissipation and thus yields a finite dc conductivity, the plasma model predicts an infinite dc conductivity. Surprisingly, a number of

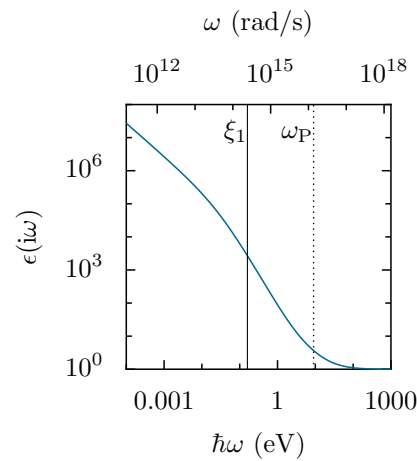


Figure 7.1: Frequency dependence of the permittivity of gold used in the numerical calculations. The vertical solid line indicates the first Matsubara frequency ξ_1 while the dotted line indicates the plasma frequency ω_P .

experiments are in agreement with the plasma prescription [9, 10, 39, 40, 42]. In particular, the Drude prescription has been experimentally excluded at a 95% confidence level for separations between 223 and 350 nm in Ref. [40], and at a 99.9% confidence level for separations between 210 and 620 nm in Refs. [9, 10]. In a few cases experimental support for the Drude prescription has been claimed [30, 31], but also questioned [46, 47].

Theoretically, it has been argued that the use of the Drude model results in negative entropies and a violation of the Nernst heat theorem [155–157]. Since the Casimir entropy is an interaction entropy, negative entropies are not in contradiction to thermodynamics [74]. In fact, negative Casimir entropies also occur for perfect reflectors in the plane-sphere geometry [158], and for perfect reflectors and the plasma model in the sphere-sphere geometry [159]. However, the entropy should still satisfy the Nernst heat theorem. While the Drude model violates the Nernst heat theorem for perfect lattices [157], the theorem is not violated for lattices with impurities [160]. Moreover, it has been argued that the Drude model leads to Joule heating which violates the assumption of thermal equilibrium used to derive the Lifshitz formula [20]. Therefore, it has been suggested that the scattering approach might not be valid for dissipative materials [161]. On the other hand, it has been shown that the scattering formula also holds for dissipative objects [92]. In addition, Ref. [76] argues that even in the plasma model the TE mode does not contribute to the Casimir free energy. Furthermore, since the plate in experiments is grounded, it has been argued that the zero frequency should be described by Dirichlet boundary conditions [162]. For small separations, however, Dirichlet and Drude boundary conditions give the same result to leading order [162]. All in all, there is no agreement yet on how the zero-frequency contribution should be accounted for.

7.2 Corrections beyond the proximity force approximation

We calculate the Casimir force $F = -\partial\mathcal{F}/\partial L$ and compare the results with the proximity force approximation $F_{\text{PFA}} = 2\pi R\mathcal{F}_{\text{PP}}(L)/A$, where $\mathcal{F}_{\text{PP}}(L)/A$ is the Casimir free energy per unit area for parallel plates at a distance L . In particular, we focus on an experiment by Krause *et al.* which derived an upper bound for deviations from the PFA [38]. Within the derivative expansion approach, the leading correction to the PFA is of the form

$$\frac{F}{F_{\text{PFA}}} - 1 = \beta(L)\frac{L}{R} + \dots, \quad (7.1)$$

with the coefficient $\beta(L)$ being independent of R [100]. The sub-leading corrections might contain logarithmic terms, as for instance in the case of high temperatures [51, 52]. For the special case of perfect reflectors and zero temperature, the coefficient β is independent of L and given by $\beta_{T=0}^{\text{PR}} = 1/6 - 10/\pi^2 \approx -0.847$ [49, 101].

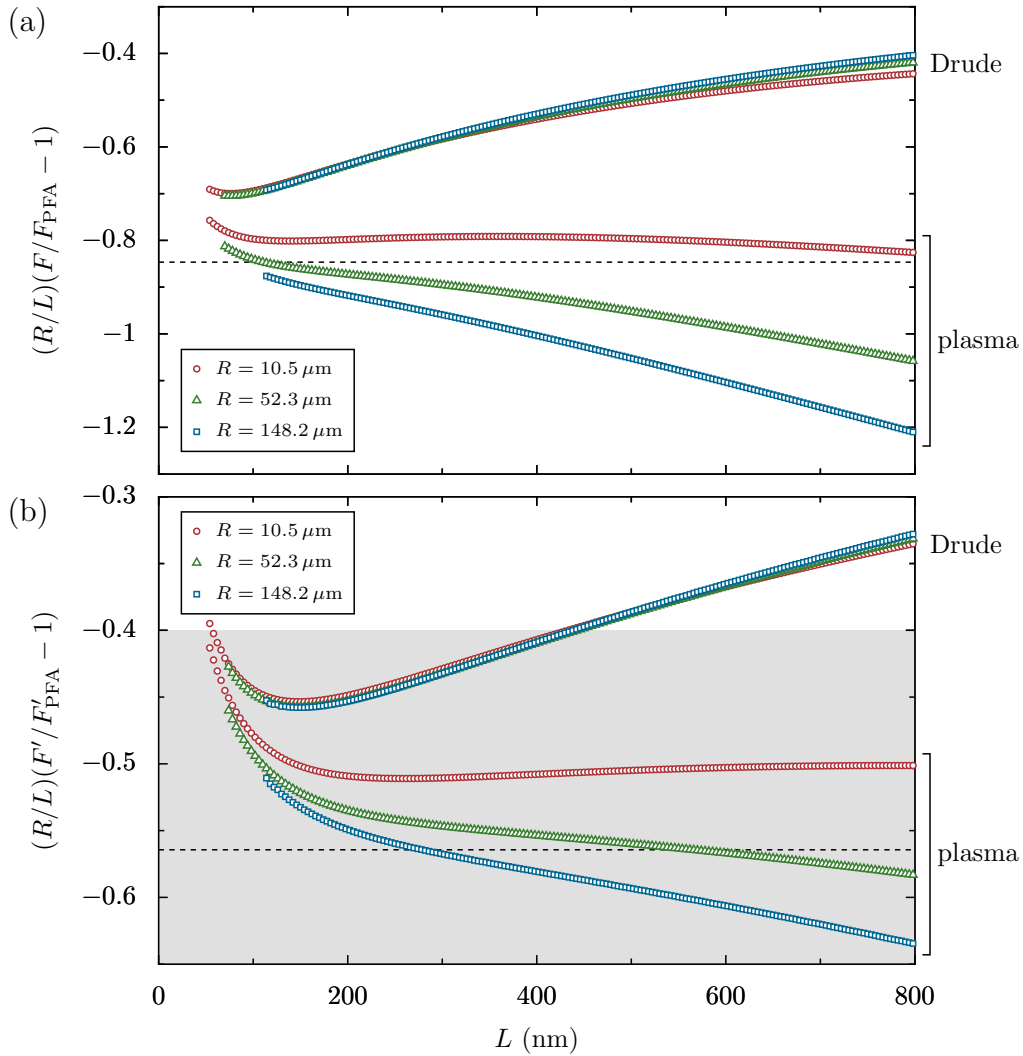


Figure 7.2: Beyond-PFA corrections to (a) the force and (b) the force gradient are shown as function of the distance between sphere and plane. We multiply the correction by the aspect ratio R/L . The upper three and lower three lines refer to the Drude and plasma prescription, respectively. The dashed horizontal lines indicate the results for perfect reflectors at zero temperature, corresponding to the constant coefficients $\beta_{T=0}^{\text{PR}}$ and $\beta'_{T=0}^{\text{PR}}$ for the force and force gradient, respectively, as defined in the text. In the lower panel, the grey area marks the parameter range for the force gradient excluded experimentally at the 95% confidence level [38]. (Same plot as in Ref. [54] but for slightly different radii.)

In order to test (7.1) and obtain a numerical approximation for $\beta(L)$, we plot in Fig. 7.2a the variation of $(R/L)(F/F_{\text{PFA}} - 1)$ with the distance L for radii $R = 10.5, 52.3,$ and $148.2 \mu\text{m}$. The values chosen correspond to the sphere radii measured in Ref. [38]. The upper three curves correspond to the Drude prescription while the lower three curves correspond to the plasma prescription. The dashed line indicates the value of $\beta_{T=0}^{\text{PR}}$. According to (7.1), the correction to the force scaled with R/L should approach $\beta(L)$ and be independent of R for sufficiently small values of L/R . This is indeed the case when considering the Drude prescription for $L \lesssim 400 \text{ nm}$ and the sphere radii shown in Fig. 7.2. As the distance increases, the curves representing different radii start to deviate from each other. This behavior can be associated with the contribution of sub-leading corrections which become comparatively more important as L increases. At a fixed temperature, larger distances result in an increase of the relative contribution of the zero Matsubara frequency [51], for which the sub-leading correction is comparable to the leading one for the parameters represented in the figure.

On the other hand, when taking the plasma prescription for the zero-frequency contribution, the curves corresponding to different values of R , shown in the lower part of Fig. 7.2a, are well separated from each other, indicating that the correction to the PFA is not of the form (7.1) in this case. The contributions from the Matsubara frequencies with $n \neq 0$ are exactly the same for the two models. Hence the difference shown in Fig. 7.2a is entirely due to the TE zero-frequency contribution present in the plasma prescription but not in the Drude prescription.

The zero-frequency contribution becomes relatively more important as L increases, separating the plasma curves from each other and from the Drude curve. The derivative expansion approach fails in the plasma model at finite temperatures precisely because of the non-analytical nature of the perturbative kernel corresponding to the TE zero-frequency contribution [153], thus resulting in the structure shown in the lower part of Fig. 7.2a. We also remark that in contrast to what is frequently believed, the case of perfect reflectors at zero temperature, indicated by the horizontal dashed line in Fig. 7.2a, does not provide an upper bound for the magnitude of the force correction for $L \gtrsim 100 \text{ nm}$ due to the contribution of the TE zero-frequency mode in the plasma model.

The magnitude of the correction to the PFA result was experimentally investigated in Ref. [38]. The Casimir force gradient $F' = -\partial^2 \mathcal{F} / \partial L^2$ was measured for different sphere radii, and a linear dependence with $1/R$ similar to (7.1) was proposed

$$\frac{F'}{F'_{\text{PFA}}} - 1 = \beta'(L) \frac{L}{R} + \dots \quad (7.2)$$

While the authors of Ref. [38] were unable to measure the correction term, they nonetheless derived the upper bound $|\beta'(L)| < 0.4$ at the 95% confidence level for separations L between 164 and 300 nm. In Fig. 7.2b, we plot the variation of $(R/L)(F'/F'_{\text{PFA}} - 1)$ as a

function of the separation L for the same radii used in Fig. 7.2a. This quantity provides an approximation for the coefficient $\beta'(L)$ as long as the results are independent of R . The shaded area represents values for the correction excluded by the experiment [38], while the dashed line indicates the correction for perfect reflectors at $T = 0$ given by $\beta'_{T=0}^{\text{PR}} = (2/3)\beta_{T=0}^{\text{PR}} \approx -0.564$ [49, 101].

For $L \lesssim 400$ nm the Drude as well as the plasma prescription violate the experimental bound, although the maximum violation for the Drude prescription at $L \approx 150$ nm corresponding to $\beta' \approx -0.46$ is significantly smaller than the violation found for the plasma prescription. Note, however, that the plasma and Drude curves get closer to each other as the distance decreases below 200 nm, as expected in the low temperature regime, with the zero frequency providing a relatively smaller contribution.

As in the discussion of the correction to the force, the results for different radii shown in Fig. 7.2b are very close to each other and to the results obtained within the derivative expansion approach [102, 149] when taking the Drude prescription. In this case, our results show that sub-leading corrections are negligible for the experimental conditions of Refs. [9, 10, 38, 42], which correspond to aspect ratios in the range $R/L \sim 10^2 - 10^3$. As a consequence, the corrections can be directly obtained within the derivative expansion approach [102, 149]. However, for the plasma prescription the derivative expansion clearly underestimates the correction, particularly for the largest radius shown in Fig. 7.2b, and the leading order correction is not proportional to $1/R$.

In order to better understand the dependence on the sphere radius, we plot in Figs. 7.3a and 7.3c the force and force gradient corrections, respectively, as function of $1/R$. For the plasma prescription, the force corrections are typically close to or above the percent level for the conditions of the experiment [42] where $1/R = 0.0242 \mu\text{m}^{-1}$. More importantly for this experiment, the corrections to the force gradient are typically below 1% for sub-micrometer distances. In Figs. 7.3b and 7.3d the corrections to the force and force gradient, respectively, are scaled by R/L . While for the Drude prescription the data follow rather closely a $1/R$ dependence, the results for the plasma prescription indicate a more singular approach to the PFA limit as $1/R \rightarrow 0$.

7.3 Comparison with experimental data

All experiments reported in the literature so far have been compared with theory using the proximity force approximation. We now compare for the first time experimental data obtained for the force gradient in Ref. [38] with numerically exact results computed using the scattering formula. The experimental data were kindly provided by Ricardo Decca.

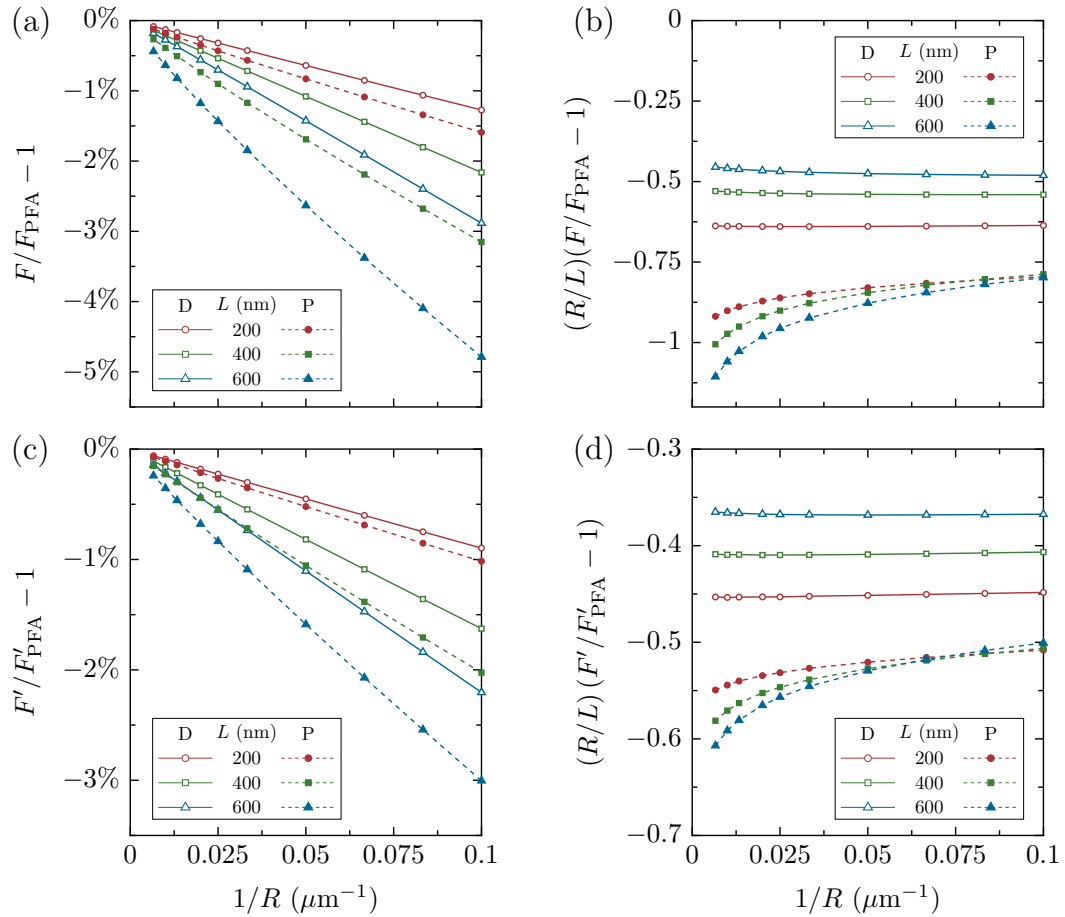


Figure 7.3: Beyond-PFA corrections to the (a,b) force and (c,d) force gradient are shown as function of the inverse sphere radius. While in panels (a) and (c) the relative corrections are displayed, the data in panels (b) and (d) have been scaled by R/L . The plane-sphere distances are $L = 200$ nm (\circ), 400 nm (\square), and 600 nm (\triangle). Solid lines with open symbols refer to the Drude prescription (D) while dashed lines with filled symbols refer to the plasma prescription (P). (From [54])

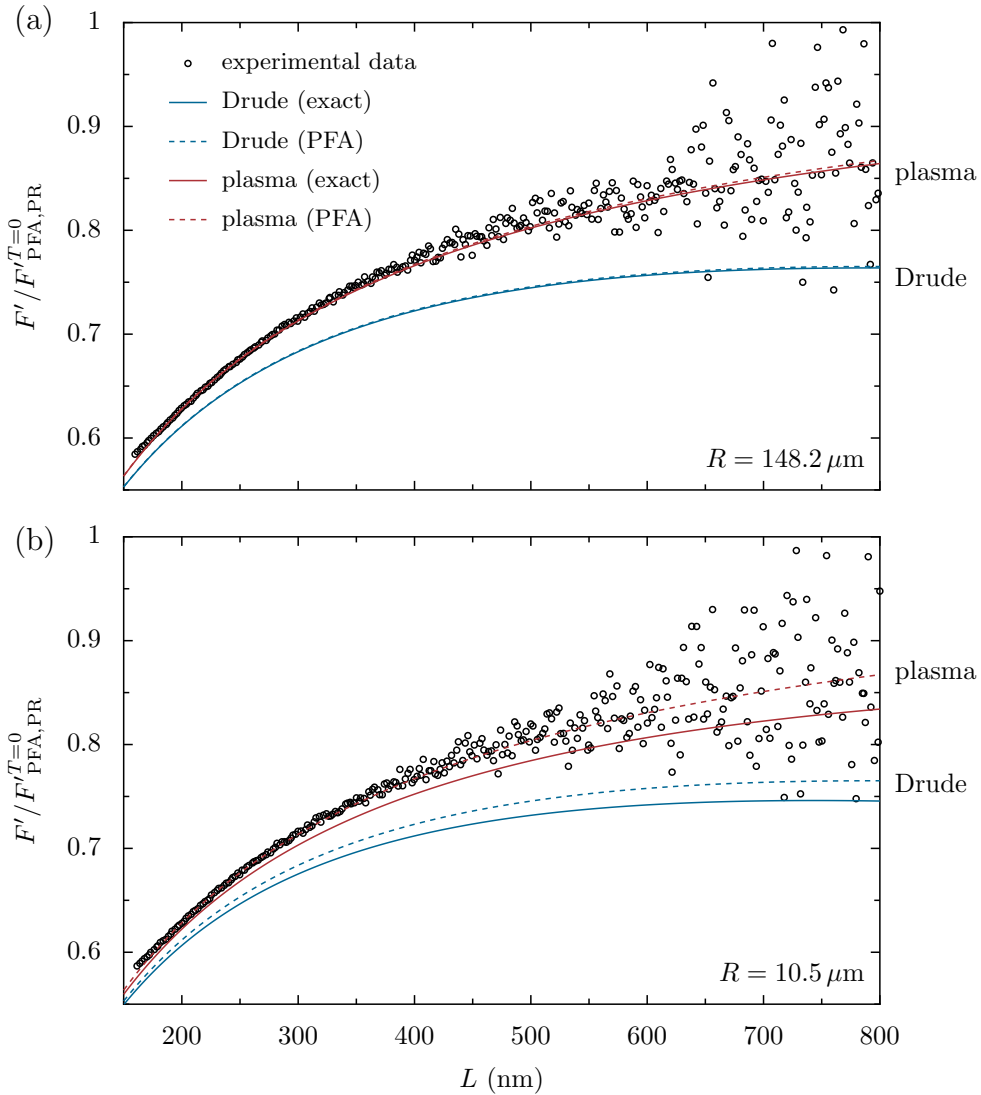


Figure 7.4: The force gradient F' for gold metals at room temperature $T = 295$ K normalized by the result of the PFA for perfect reflectors at $T = 0$ is shown as a function of the separation L for sphere radii (a) $R = 148.2 \mu\text{m}$ and (b) $R = 10.5 \mu\text{m}$. The circles correspond to experimental data obtained in Ref. [38]. The solid lines represent the exact numerical computation, the dashed lines have been obtained within the PFA. The experimental data were kindly provided by Ricardo Decca.

In Fig. 7.4, we show the force gradient for radii (a) $R = 148.2 \mu\text{m}$ and (b) $R = 10.5 \mu\text{m}$ normalized by the pressure for perfect reflectors at zero temperature using the PFA

$$F_{\text{PFA,PR}}^{T=0} = \frac{\pi^3 \hbar c R}{120 L^4} \quad (7.3)$$

as a function of the separation L . The circles correspond to the experimental data, the full lines represent our numerical results, and the dashed lines are the PFA results. At large separations the experimental error is significantly larger than at small separations, causing the dispersion of the data points seen in the figure. Unfortunately, we do not have error bars for the experimental data. For the sphere of radius $R = 148.2 \mu\text{m}$ shown in Fig. 7.4a, the results obtained using the scattering formula and within the proximity force approximation are close together. This is no surprise since the smallest aspect ratio shown in the figure is still $R/L \sim 190$. While the plasma lines show good agreement with the experimental data, the discrepancy between the experimental results and the lines corresponding to the Drude prescription is significant. We also note that there is a small discrepancy between the experimental points and the lines based on the plasma prescription at very small separations.

In Fig. 7.4b, we depict experimental data for a sphere of radius $R = 10.5 \mu\text{m}$. As this sphere is considerably smaller, the smallest aspect ratio shown in this figure is only $R/L \sim 13$. As a consequence, the dashed and solid lines computed using the scattering formula and within the PFA deviate as the separation increases. Again, the mismatch between the experimental points and the Drude lines is considerable. The situation for the plasma lines, however, is a bit more involved now. Like for the larger sphere, the PFA result using the plasma prescription is in good agreement with the experimental data, but the exact plasma line (solid red line) clearly deviates from the experimental data. The effect is most pronounced at separations $L \simeq 350 \text{ nm}$. For smaller separations the difference between the exact result and the PFA result is small, and for larger separations the experimental error makes a distinction difficult.

For the comparison, we used slightly different values for the plasma frequency and the relaxation frequency than the ones obtained experimentally, cf. section 7.1. Even though we have checked that the different parameters have a negligible influence on the force gradient within the PFA, a more thorough comparison requires a recomputation of the numerical data using the plasma frequency and the relaxation frequency obtained in the experiment. Moreover, we did not consider the experimental errors here since we do not have access to these data. Of course, a more detailed analysis must also consider the experimental error.

It is puzzling why the PFA yields a better agreement than the exact result obtained using the scattering formula. Since the experimental data are closer to the PFA result, this explains why the corrections to the PFA obtained using our numerics and in the experiment

reported in Ref. [38] disagree. The results presented in this chapter imply that there is a discrepancy between theory and experiment. This might be caused by experimental errors or because the theoretical treatment neglects some important features present in experiments.

We have ignored corrections due to the roughness of the sphere and the plate. From Refs. [9, 163] one can estimate that the roughness correction is $\lesssim 1\%$ of the Casimir pressure at $L = 160$ nm and decreases for larger separations. Also, while we assume a full gold sphere in our numerical calculations, experiments use spheres that are coated by 200 nm of gold [163]. Patch potentials and spatial nonlocality, i.e., a dielectric function that also depends on the wave vector, are negligible for this experiment [163].

In conclusion, we have shown that the Drude prescription leads to a weaker violation of the upper bound for the PFA correction derived experimentally in Ref. [38] than the dissipationless plasma prescription. The PFA combined with the Drude prescription underestimates the experimental data for nonmagnetic materials, so that the correction calculated here brings the Drude prediction even further away from the experimental results. When taking the plasma prescription, the magnitude of the correction is significantly larger than predicted experimentally. Moreover, we have shown that for the force gradient the PFA yields better agreement with the experimental data than the exact results taking the sphere curvature fully into account. This is puzzling since the PFA is only an approximation and should yield a worse agreement than the results obtained within the scattering approach. Our findings indicate that experiments probing the Casimir interaction beyond the PFA regime could provide new insight into the role of dissipation in Casimir physics.

Chapter 8

Conclusion and outlook

In this thesis, we have studied the Casimir interaction in the experimentally important geometry of a sphere and a plane. We have focused on the proximity force approximation which has been exclusively used to analyze experiments in this geometry. Our results can be divided in three parts: (i) the derivation of the proximity force approximation as the first term in an asymptotic expansion, (ii) the extension of the numerics to aspect ratios $R/L \sim 5000$ used in typical experiments, and (iii) the comparison of the PFA with numerical results and the computation of corrections to the PFA.

We have derived the proximity force approximation expression for the Casimir free energy as the leading asymptotic result in the limit of large aspect ratios R/L . To leading order, only the direct reflection term in the Debye expansion of the WKB Mie scattering amplitudes contributes. The trace over a number of round-trip matrices has been evaluated within the saddle-point approximation. The saddle point corresponds to the conservation of the wave-vector component parallel to the plane. Therefore, the leading-order contribution results from specular reflection in the vicinity of the points of closest distance between the sphere and the plane. Our derivation holds for arbitrary materials and temperatures. As an important consequence, we find that no polarization mixing contributes to leading order. From a more theoretical perspective, our results help understanding why local approaches such as the derivative expansion are capable of providing both the leading and next-to-leading-order terms in several situations of interest.

The standard approach to calculating the Casimir free energy within the scattering approach has been plagued with ill-conditioned round-trip matrices resulting in numerical difficulties. We have shown that these difficulties can be eliminated by a symmetrization of the round-trip operator. Moreover, the determinant of the symmetrized round-trip operator can be evaluated using a state-of-the-art algorithm suited for hierarchical matrices. This significantly reduces the computational time and thus allows us to perform calculations in the experimentally relevant regime with aspect ratios up to $R/L \sim 5000$, an improvement of almost two orders of magnitude compared to the largest aspect ratios treated so far [26].

With large aspect ratios being numerically accessible, we have assessed the quality of the PFA by determining its deviations from the exact result. For zero temperature, we confirm the leading-order correction to the PFA which is linear in L/R . Commonly, it is believed that the next-to-leading-order correction is either quadratic $(L/R)^2$ or of the form $(L/R)^n \log(L/R)$, where n denotes an integer [100–102]. In contrast to this expectation, we find that for perfect reflectors and metals described by the plasma and the Drude model, the next-to-leading-order correction is proportional to $(L/R)^{3/2}$. This suggests that for the next-to-leading-order correction to the PFA non-local effects and/or the far side of the sphere become important. As a consequence, the next-to-leading-order correction to the PFA cannot be obtained within the framework of the derivative expansion.

Furthermore, we have compared numerically exact results obtained using the scattering formula with the PFA for parameters corresponding to typical experiments. We have shown that the dissipationless plasma prescription leads to a violation of the upper bound for the PFA correction obtained experimentally in Ref. [38]. This could have been expected, since dissipation is present in the gold coatings used in the experiment. However, all experiments performed with coated microspheres with aspect ratios $R/L \sim 10^2 - 10^3$ agree with the plasma prescription but not with the Drude prescription [9, 10, 39, 40, 42]. When taking the Drude prescription, the correction is smaller but still in violation of the experimental bound for small distances between sphere and plane. Moreover, we have directly compared our numerical results with the experimental data of Ref. [38]. While the plasma prescription within the proximity force approximation agrees well with the experimental data, the exact results obtained within the scattering approach deviate from the experimental data when the aspect ratio is rather small. Our results suggest a discrepancy between Casimir experiments on the one hand, and the theoretical description on the other hand. The theoretical results presented here, taking the sphere curvature fully into account, indicate that experiments probing the Casimir interaction beyond the PFA regime could provide new insight into the role of dissipation in Casimir physics.

Our results leave room for future work. The derivation of the PFA using the plane-wave basis can be applied to other geometries like the plane-cylinder geometry, and it can be adapted to non-equilibrium situations like heat radiation or heat transfer [164]. In addition, our method is a starting point to calculate analytical corrections to the PFA. Moreover, the numerical evaluation of the Casimir interaction in the continuous plane-wave basis using the Nyström method [110] might be a fast alternative to the approach described here. Also, our numerical implementation can be used to compare exact results with data obtained within the derivative expansion, thereby assessing the quality of the approximation. Finally, our approach also opens the way to calculate exact results for a variety of recent experiments with similar aspect ratios and different materials like magnetic materials [40, 165] and layered surfaces [39].

Appendix A

Special functions

A.1 Spherical harmonics

The spherical harmonics [91, §14.30.3]

$$Y_\ell^m(\theta, \varphi) = (-1)^m N_\ell^m \sin^m \theta \frac{e^{im\varphi}}{\sqrt{2\pi}} \frac{d^m}{dx^m} P_\ell(x) \Big|_{x=\cos \theta} \quad (\text{A.1})$$

are functions defined on the unit sphere that satisfy Laplace's equation. Here, the factor

$$N_\ell^m = \sqrt{\frac{2\ell + 1}{2} \frac{(\ell - m)!}{(\ell + m)!}} \quad (\text{A.2})$$

is a normalization constant and P_ℓ denotes the Legendre polynomial of degree ℓ . The factor $(-1)^m$ corresponds to the Condon-Shortley phase. The spherical harmonics form a complete and orthonormal set of functions on the unit sphere.

In terms of the associated Legendre polynomials P_ℓ^m with the phase convention defined in the next section, the spherical harmonics are given by

$$Y_\ell^m(\theta, \varphi) = N_\ell^{m,i^m} P_\ell^m(\cos \theta) \frac{e^{im\varphi}}{\sqrt{2\pi}}. \quad (\text{A.3})$$

A.2 Associated Legendre polynomials

We define the associated Legendre polynomials as [138, p. 94]

$$P_\ell^m(x) = (x^2 - 1)^{m/2} \frac{d^m}{dx^m} P_\ell(x). \quad (\text{A.4})$$

Our phase convention differs from the usual choice: We omit the Condon-Shortley phase $(-1)^m$ and change the sign in the first term. This effectively introduces the phase factor

$(-i)^m$ compared to the usual definition of the associated Legendre polynomials for example employed by the NIST Digital Library of Mathematical Functions [91, §14.6.1]. The definition (A.4) is well adapted for the case $|x| \geq 1$.

The associated Legendre polynomials obey the recurrence relations [138, p. 94]

$$P_\ell^m(x) = xP_{\ell-1}^m(x) + (\ell + m - 1)\sqrt{x^2 - 1}P_{\ell-1}^{m-1}(x), \quad (\text{A.5a})$$

$$P_\ell^m(x) = -\frac{2(m-1)}{\sqrt{x^2 - 1}}xP_\ell^{m-1}(x) + (\ell + m - 1)(\ell - m + 2)P_\ell^{m-2}(x), \quad (\text{A.5b})$$

$$P_\ell^m(x) = \frac{1}{\ell - m} [(2\ell - 1)xP_{\ell-1}^m(x) - (\ell + m - 1)P_{\ell-2}^m(x)], \quad (\text{A.5c})$$

$$P_\ell^{m'}(x) = -\frac{mx}{x^2 - 1}P_\ell^m(x) + \frac{(\ell + m)(\ell - m + 1)}{\sqrt{x^2 - 1}}P_\ell^{m-1}(x), \quad (\text{A.5d})$$

$$P_\ell^{m'}(x) = \frac{1}{x^2 - 1} [\ell x P_\ell^m(x) - (\ell + m)P_{\ell-1}^m(x)]. \quad (\text{A.5e})$$

For $\ell = m$ they are given by

$$P_m^m(x) = \frac{(2m)!}{2^m m!} (x^2 - 1)^{m/2}. \quad (\text{A.6})$$

Combining (A.5b) and (A.5d) yields the recurrence relation

$$P_\ell^{m'}(x) = \frac{P_\ell^{m+1}(x)}{\sqrt{x^2 - 1}} + \frac{mx}{x^2 - 1}P_\ell^m(x). \quad (\text{A.7})$$

Combining (A.5c) and (A.5e) yields

$$P_\ell^{m'}(x) = \frac{1}{x^2 - 1} \left(\frac{\ell(\ell - m + 1)P_{\ell+1}^m(x)}{2\ell + 1} - \frac{(\ell + 1)(\ell + m)P_{\ell-1}^m(x)}{2\ell + 1} \right). \quad (\text{A.8})$$

We now briefly list some properties valid for $x \geq 1$ that we will use in different parts of the thesis:

1. The associated Legendre polynomials are real which follows from the definition (A.4).
2. There are no zeros in the interval $(1, \infty)$ [91, §14.16].
3. The functions have either even or odd parity:

$$P_\ell^m(-x) = (-1)^{\ell+m} P_\ell^m(x) \quad (\text{A.9a})$$

$$P_\ell^{m'}(-x) = (-1)^{\ell+m+1} P_\ell^{m'}(x) \quad (\text{A.9b})$$

4. For negative order [138, p. 94]:

$$P_\ell^{-m}(x) = \frac{(\ell - m)!}{(\ell + m)!} P_\ell^m(x), \quad m \geq 0 \quad (\text{A.10})$$

5. Behavior at singularities [91, §14.8]:

$$P_\ell^m(x) \stackrel{x \rightarrow \infty}{\simeq} \frac{(2\ell)!}{2^\ell \ell! (\ell - m)!} x^\ell \quad (\text{A.11a})$$

$$P_\ell^m(x) \stackrel{x \rightarrow 1^+}{\simeq} \frac{(\ell + m)!}{m! (\ell - m)!} \left(\frac{x - 1}{2} \right)^{m/2} \quad (\text{A.11b})$$

6. Because of 1, 2 and 5

$$P_\ell^m(x) \geq 0. \quad (\text{A.12})$$

7. They obey the inequality

$$P_\ell^m(x) \geq \frac{2\ell - 1}{\ell - m} x P_{\ell-1}^m(x) \quad (\text{A.13})$$

which can be seen from (A.5c).

8. The first derivative is non-negative.

For $\ell = m$:

$$(x^2 - 1)P_\ell^{\ell'}(x) \stackrel{(\text{A.5e})}{=} \ell x P_\ell^\ell(x) - (\ell + \ell)P_{\ell-1}^\ell(x) = \ell x P_\ell^\ell(x) \geq 0, \quad (\text{A.14})$$

and for $\ell > m$

$$\begin{aligned} (x^2 - 1)P_\ell^{m'}(x) &\stackrel{(\text{A.5e})}{=} \ell x P_\ell^m(x) - (\ell + m)P_{\ell-1}^m(x) \\ &\stackrel{(\text{A.13})}{\geq} P_{\ell-1}^m(x) \left[\ell x^2 \frac{2\ell - 1}{\ell - m} - (\ell + m) \right] \\ &\stackrel{x \geq 1}{\geq} P_{\ell-1}^m(x) \left[\ell \frac{2\ell - 1}{\ell - m} - (\ell + m) \right] \\ &\stackrel{\ell > m}{\geq} P_{\ell-1}^m(x) (\ell - 1 - m) \geq 0. \end{aligned} \quad (\text{A.15})$$

9. From the definition (A.4) and from (A.12) follows that all derivatives of ordinary Legendre polynomials are non-negative:

$$\frac{d^m}{dx^m} P_\ell(x) \geq 0 \quad (\text{A.16})$$

10. Derivatives at $x = 1$ for $m = 0$:

$$P_n(1) = 1 \quad (\text{A.17a})$$

$$P'_n(1) = \frac{n(n+1)}{2} \quad (\text{A.17b})$$

$$P''_n(1) = \frac{(n-1)n(n+1)(n+2)}{8} \quad (\text{A.17c})$$

$$P'''_n(1) = \frac{(n-2)(n-1)n(n+1)(n+2)(n+3)}{48} \quad (\text{A.17d})$$

Appendix B

Proofs and derivations

B.1 Signs of Mie coefficients

The Mie coefficients at imaginary frequencies are given by

$$a_\ell(ix) = (-1)^\ell \frac{\pi}{2} \frac{n^2 s_\ell^{(a)} - s_\ell^{(b)}}{n^2 s_\ell^{(c)} + s_\ell^{(d)}}, \quad (\text{B.1a})$$

$$b_\ell(ix) = (-1)^{\ell+1} \frac{\pi}{2} \frac{s_\ell^{(b)} - s_\ell^{(a)}}{s_\ell^{(c)} + s_\ell^{(d)}}, \quad (\text{B.1b})$$

where we have used the abbreviations

$$s_\ell^{(a)}(x) = I_{\ell+1/2}(nx) I_{\ell+1/2}(x) [g_{\ell-1/2}(x) - \ell], \quad (\text{B.2a})$$

$$s_\ell^{(b)}(x) = I_{\ell+1/2}(nx) I_{\ell+1/2}(x) [g_{\ell-1/2}(nx) - \ell], \quad (\text{B.2b})$$

$$s_\ell^{(c)}(x) = I_{\ell+1/2}(nx) [x K_{\ell-1/2}(x) + \ell K_{\ell+1/2}(x)], \quad (\text{B.2c})$$

$$s_\ell^{(d)}(x) = I_{\ell+1/2}(nx) K_{\ell+1/2}(x) [g_{\ell-1/2}(nx) - \ell]. \quad (\text{B.2d})$$

The Mie coefficients are evaluated at $x = \xi R/c > 0$, $n = \sqrt{\varepsilon(i\xi)} \geq 1$ denotes the refractive index at imaginary frequency, and the function $g_\nu(x)$ is defined as

$$g_\nu(x) = x \frac{I_\nu(x)}{I_{\nu+1}(x)}. \quad (\text{B.3})$$

We will show that the coefficients $s_\ell^{(a)}$, $s_\ell^{(b)}$, $s_\ell^{(c)}$, $s_\ell^{(d)}$ are positive, and that the signs of the Mie coefficients are given by

$$\text{sign}(a_\ell) = (-1)^\ell, \quad \text{sign}(b_\ell) = (-1)^{\ell+1}. \quad (\text{B.4})$$

The modified Bessel functions of the first kind $I_\nu(x)$ and of the second kind $K_\nu(x)$ are positive for $x > 0$. Therefore, $s_\ell^{(c)}$ is positive. Using the Mittag-Leffler expansion [166] the

inverse of $g_\nu(x)$ can be expressed as a series

$$g_\nu^{-1}(x) = \frac{1}{x} \frac{I_{\nu+1}(x)}{I_\nu(x)} = \sum_{k=1}^{\infty} \frac{2}{J_{\nu,k}^2 + x^2}. \quad (\text{B.5})$$

Here, $J_{\nu,k}$ denotes the k th zero of the ordinary Bessel function $J_\nu(x)$. The derivative of (B.5) is given by

$$\frac{d}{dx} g_\nu^{-1}(x) = -\frac{1}{g_\nu^2(x)} \frac{d}{dx} g_\nu(x) = \sum_{k=1}^{\infty} \frac{-4x}{(J_{\nu,k}^2 + x^2)^2}. \quad (\text{B.6})$$

After reorganization, we find that $g_\nu(x)$ is a strictly monotonically increasing function

$$\frac{d}{dx} g_\nu(x) = g_\nu^2(x) \sum_{k=1}^{\infty} \frac{4x}{(J_{\nu,k}^2 + x^2)^2} > 0. \quad (\text{B.7})$$

The function $g_\nu(x)$ obtains its minimum at $x = 0$. From the limiting form when ν is fixed and $x \rightarrow 0$ [91, §10.30.1]

$$I_\nu(x) \sim \frac{1}{\Gamma(\nu + 1)} \left(\frac{x}{2}\right)^\nu \quad (\text{B.8})$$

we find

$$\lim_{x \rightarrow 0} g_\nu(x) = 2(\nu + 1). \quad (\text{B.9})$$

Therefore, $g_\nu(x)$ is bounded from below by

$$g_\nu(x) \geq 2(\nu + 1), \quad (\text{B.10})$$

and consequently $s_\ell^{(a)}$, $s_\ell^{(b)}$, $s_\ell^{(d)}$ are positive.

We will now show that the numerators in (B.1) are positive. The numerator of b_ℓ

$$s_\ell^{(b)} - s_\ell^{(a)} = I_{\ell+1/2}(nx) I_{\ell+1/2}(x) [g_{\ell-1/2}(nx) - g_{\ell-1/2}(x)] \geq 0 \quad (\text{B.11})$$

is positive, as $g_\nu(nx) \geq g_\nu(x)$ for $n \geq 1$. The ratio $g_\nu(nx)/g_\nu(x)$ is also a strictly monotonically increasing function of n with the maximum obtained as $n \rightarrow \infty$

$$\frac{g_\nu(nx)}{g_\nu(x)} = n \frac{I_\nu(nx)}{I_{\nu+1}(nx)} \frac{I_{\nu+1}(x)}{I_\nu(x)} \stackrel{n \gg 1}{\cong} n \frac{I_{\nu+1}(x)}{I_\nu(x)} < n. \quad (\text{B.12})$$

This gives the estimate

$$ng_\nu(x) \geq g_\nu(nx). \quad (\text{B.13})$$

which can be used to prove that the numerator of a_ℓ is also positive:

$$\begin{aligned}
 n^2 s_\ell^{(a)} - s_\ell^{(b)} &= I_{\ell+1/2}(nx)I_{\ell+1/2}(x) [n^2 g_{\ell-1/2}(x) - g_{\ell-1/2}(nx) - \ell(n^2 - 1)] \\
 &\stackrel{(B.13)}{\geq} I_{\ell+1/2}(nx)I_{\ell+1/2}(x) [n(n-1)g_{\ell-1/2}(x) - \ell(n+1)(n-1)] \\
 &= I_{\ell+1/2}(nx)I_{\ell+1/2}(x)(n-1) [ng_{\ell-1/2}(x) - \ell(n+1)] \\
 &\stackrel{(B.10)}{\geq} I_{\ell+1/2}(nx)I_{\ell+1/2}(x)(n-1) [n(2\ell+1) - \ell(n+1)] \\
 &= I_{\ell+1/2}(nx)I_{\ell+1/2}(x)(n-1)(\ell n + n - \ell) \\
 &\geq I_{\ell+1/2}(nx)I_{\ell+1/2}(x)(n-1)^2 \ell \geq 0
 \end{aligned} \tag{B.14}$$

In both cases, the numerator vanishes for $n = 1$ as expected.

B.2 Inequality for associated Legendre polynomials of the Turán type

For $x \geq 1$ and $\ell \geq m > 0$ the associated Legendre polynomials satisfy the inequality

$$[P_\ell^m(x)]^2 - P_\ell^{m+1}(x)P_\ell^{m-1}(x) \geq 0. \tag{B.15}$$

Proof:

The ratio of two associated Legendre polynomials of the same degree and order m and $m + 1$ can be computed using the continued fraction [91, §14.14]

$$q_m(x) = \frac{1}{2} \sqrt{x^2 - 1} \frac{P_\ell^m(x)}{P_\ell^{m-1}(x)} = \frac{x_0}{y_0 + \frac{x_1}{y_1 + \frac{x_2}{y_2 + \frac{x_3}{y_3 + \dots}}}} \tag{B.16}$$

where

$$\begin{aligned}
 x_k &= \frac{x^2 - 1}{4} (\ell - m - k + 1)(\ell + m + k), \\
 y_k &= (m + k)x.
 \end{aligned} \tag{B.17}$$

For any sequence of non-zero $\{c_n\}$ the continued fraction is equivalent to

$$q_m(x) = \frac{c_0 x_0}{c_0 y_0 + \frac{c_1 c_1 x_1}{c_1 y_1 + \frac{c_2 c_2 x_2}{c_2 y_2 + \frac{c_3 c_3 x_3}{c_3 y_3 + \dots}}}}. \tag{B.18}$$

With the choice $c_0 = 1/x_0$, $c_1 = 1/(c_0 x_1)$, $c_2 = 1/(c_1 x_2)$, $c_3 = 1/(c_2 x_3)$, \dots , the continued fraction $q_m(x)$ becomes a regular continued fraction

$$q_m(x) = [a_0^m, a_1^m, a_2^m, a_3^m, a_4^m, \dots] \tag{B.19}$$

where $a_0^m = 0$ and $a_n^m = c_{n-1}y_{n-1}$. The continued fractions $q_m(x)$ and $q_{m+1}(x)$ differ at index $n = 1$:

$$a_1^m = c_0 y_0 = \frac{y_0}{x_0} = \frac{4x}{x^2 - 1} \frac{m}{(\ell - m + 1)(\ell + m)} < a_1^{m+1} \quad (\text{B.20})$$

As the continued fractions differ at an odd index, $q_m(x) > q_{m+1}(x)$. Then it follows

$$\frac{P_\ell^m(x)}{P_\ell^{m-1}(x)} > \frac{P_\ell^{m+1}(x)}{P_\ell^m(x)}. \quad (\text{B.21})$$

After rearrangement the conjecture follows.

B.3 Determinant of block matrices

Let $A, B, C, D \in \mathbb{R}^{n \times n}$, $\lambda \in \mathbb{R}$. Then:

$$\det \begin{pmatrix} A & \lambda B \\ \lambda^{-1} C & D \end{pmatrix} = \frac{1}{\lambda^n} \det \begin{pmatrix} \lambda A & \lambda B \\ C & D \end{pmatrix} = \frac{\lambda^n}{\lambda^n} \det \begin{pmatrix} A & B \\ C & D \end{pmatrix} = \det \begin{pmatrix} A & B \\ C & D \end{pmatrix} \quad (\text{B.22})$$

In particular, for $\lambda = -1$ this gives:

$$\det \begin{pmatrix} A & -B \\ -C & D \end{pmatrix} = \det \begin{pmatrix} A & B \\ C & D \end{pmatrix} \quad (\text{B.23})$$

B.4 Derivatives of addition theorems for spherical harmonics

Here, we derive some addition theorems for the derivatives of spherical harmonics. These addition theorems are needed to derive the matrix elements of the reflection operator \mathcal{R}_S at the sphere in the plane-wave basis in appendix C.

We start from the addition theorem for Legendre polynomials

$$P_\ell(z) = \sum_{m=-\ell}^{\ell} (-1)^m \frac{(\ell - m)!}{(\ell + m)!} P_\ell^m(z_1) P_\ell^m(z_2) \cos(m\varphi) \quad (\text{B.24})$$

with

$$z = z_1 z_2 - \sqrt{z_1^2 - 1} \sqrt{z_2^2 - 1} \cos \varphi \quad (\text{B.25})$$

where we use the phase convention defined in appendix A.2 for the associated Legendre polynomials. With $z_1 = \cos \vartheta_1$, $z_2 = \cos \vartheta_2$, $z = \cos \Theta$, and $\varphi = \varphi_2 - \varphi_1$, the addition theorem can be expressed in terms of spherical harmonics

$$P_\ell(z) = \frac{4\pi}{2\ell + 1} \sum_{m=-\ell}^{\ell} Y_\ell^{m*}(\vartheta_1, \varphi_1) Y_\ell^m(\vartheta_2, \varphi_2). \quad (\text{B.26})$$

It is convenient to express the derivatives of the Legendre polynomials in terms of the functions

$$\pi_\ell(z) = P'_\ell(z), \quad (\text{B.27a})$$

$$\tau_\ell(z) = (z^2 - 1)P''_\ell(z) + zP'_\ell(z), \quad (\text{B.27b})$$

familiar from the theory of Mie scattering. The definition of the angle functions π_ℓ and τ_ℓ is identical to the definition of Bohren, Huffman [111]. With (B.27), the derivatives of the Legendre polynomials can be expressed as

$$P'_\ell(z) = \pi_\ell(z), \quad (\text{B.28a})$$

$$P''_\ell(z) = \frac{\tau_\ell(z) - z\pi_\ell(z)}{z^2 - 1}. \quad (\text{B.28b})$$

By taking appropriate derivatives of (B.26), we obtain the following relations:

$$\begin{aligned} \frac{4\pi}{2\ell + 1} \sum_{m=-\ell}^{\ell} \frac{dY_\ell^{m*}(\vartheta_1, \varphi_1)}{d\vartheta_1} \frac{dY_\ell^m(\vartheta_2, \varphi_2)}{d\vartheta_2} &= \sqrt{1 - z_1^2} \sqrt{1 - z_2^2} \frac{d^2 P_\ell(z)}{dz_1 dz_2} \\ &= A\tau_\ell(z) + B\pi_\ell(z) \end{aligned} \quad (\text{B.29a})$$

$$\begin{aligned} \frac{4\pi}{2\ell + 1} \sum_{m=-\ell}^{\ell} m^2 \frac{Y_\ell^{m*}(\vartheta_1, \varphi_1)}{\sin \vartheta_1} \frac{Y_\ell^m(\vartheta_2, \varphi_2)}{\sin \vartheta_2} &= \frac{1}{\sqrt{z_1^2 - 1} \sqrt{z_2^2 - 1}} \frac{d^2 P_\ell(z)}{d\varphi_1 d\varphi_2} \\ &= B\tau_\ell(z) + A\pi_\ell(z) \end{aligned} \quad (\text{B.29b})$$

$$\frac{4\pi}{2\ell + 1} \sum_{m=-\ell}^{\ell} \frac{dY_\ell^{m*}(\vartheta_1, \varphi_1)}{d\vartheta_1} \frac{imY_\ell^m(\vartheta_2, \varphi_2)}{\sin \vartheta_2} = \frac{\sqrt{1 - z_1^2}}{\sqrt{1 - z_2^2}} \frac{d^2 P_\ell(z)}{dz_1 d\varphi_2} = C\tau_\ell(z) + D\pi_\ell(z) \quad (\text{B.29c})$$

$$\frac{4\pi}{2\ell + 1} \sum_{m=-\ell}^{\ell} \frac{imY_\ell^{m*}(\vartheta_1, \varphi_1)}{\sin \vartheta_1} \frac{dY_\ell^m(\vartheta_2, \varphi_2)}{d\vartheta_2} = D\tau_\ell(z) + C\pi_\ell(z) \quad (\text{B.29d})$$

Here, we have introduced the abbreviations

$$A = \cos \varphi - z \frac{\sqrt{z_1^2 - 1} \sqrt{z_2^2 - 1}}{z^2 - 1} \sin^2 \varphi, \quad (\text{B.30a})$$

$$B = \frac{\sqrt{z_1^2 - 1} \sqrt{z_2^2 - 1}}{z^2 - 1} \sin^2 \varphi, \quad (\text{B.30b})$$

$$C = \frac{z_1 z - z_2}{z^2 - 1} \sin \varphi, \quad (\text{B.30c})$$

$$D = \frac{z_2 z - z_1}{z^2 - 1} \sin \varphi. \quad (\text{B.30d})$$

The addition theorems (B.29) coincide with a derivation by Winch and Roberts [167] for real angles. The derivation given here is more general and also holds for imaginary angles ϑ_1 and ϑ_2 .

Appendix C

Matrix elements of \mathcal{R}_S in the plane-wave basis

Here, we derive the matrix elements of the reflection operator \mathcal{R}_S at the sphere in the plane-wave basis. In the plane-sphere geometry, due to rotational symmetry, the z -axis is distinguished. Consequently, we chose the polarization vectors $\{\hat{\mathbf{e}}_{\text{TE}}, \hat{\mathbf{e}}_{\text{TM}}\}$ in (2.27) such that the z -component of the electric field vanishes for TE polarization and the z -component of the magnetic field vanishes for TM polarization, respectively. Another distinguished polarization basis is defined by the scattering plane spanned by the incident and reflected wave vectors. Using this polarization basis, the reflection at the sphere simplifies. Then, the matrix elements of \mathcal{R}_S can be obtained by exploiting relations between the two polarization bases as carried out in appendix A of Ref. [108]. Here, we use a different approach: We derive the matrix elements of \mathcal{R}_S using the change of matrix elements (D.1).

The reflection operator \mathcal{R}_S is diagonal in the multipole basis (cf. section 4.1)

$$\langle \ell, m, P, s | \mathcal{R}_S | \ell', m', P', s' \rangle = \delta_{\ell\ell'} \delta_{mm'} \delta_{PP'} \delta_{s,\text{out}} \delta_{s',\text{reg}} r_{\ell,P}^{(S)}, \quad (\text{C.1})$$

where the scattering amplitudes $r_{\ell,P}^{(S)}$ are related to the Mie coefficients by $a_\ell = -r_{\ell,E}^{(S)}$ and $b_\ell = -r_{\ell,M}^{(S)}$ [111]. We consider an incident plane wave $|\mathbf{k}_i, p_i, +\rangle$ propagating in $+z$ -direction. Projecting the plane wave on spherical waves, evaluating the scattering operator \mathcal{R}_S in the multipole basis, and then projecting the spherical waves back to a plane wave propagating in $-z$ -direction yields

$$\begin{aligned} \langle \mathbf{k}_j, p_j, - | \mathcal{R}_S | \mathbf{k}_i, p_i, + \rangle &= \sum_{P=\text{E,M}} \sum_{\ell=1}^{\infty} \sum_{m=-\ell}^{\ell} r_{\ell,P} \langle \mathbf{k}_j, p_j, - | \ell, m, P, \text{out} \rangle \langle \ell, m, P, \text{reg} | \mathbf{k}_i, p_i, + \rangle \\ &= - \sum_{\ell=1}^{\infty} \sum_{m=-\ell}^{\ell} \left[a_\ell \langle \mathbf{k}_j, p_j, - | \ell, m, \text{E}, \text{out} \rangle \langle \ell, m, \text{E}, \text{reg} | \mathbf{k}_i, p_i, + \rangle \right. \\ &\quad \left. + b_\ell \langle \mathbf{k}_j, p_j, - | \ell, m, \text{M}, \text{out} \rangle \langle \ell, m, \text{M}, \text{reg} | \mathbf{k}_i, p_i, + \rangle \right]. \end{aligned} \quad (\text{C.2})$$

Inserting the matrix elements (D.1) implementing the change between multipole and plane-wave basis yields:

$$\begin{aligned} \langle \mathbf{k}_j, p_j, - | \mathcal{R}_S | \mathbf{k}_i, p_i, + \rangle &= 8\pi^2 \frac{c}{\xi \kappa_j} \sum_{\ell=1}^{\infty} \sum_{m=-\ell}^{\ell} \frac{i^{p_i-p_j}}{\ell(\ell+1)} \left[\right. \\ &a_{\ell} \left(\frac{m}{\sin \theta_{\mathbf{k}_j}^-} \right)^{\delta_{p_j,1}} \left(\frac{\partial}{\partial \theta_{\mathbf{k}_j}^-} \right)^{1-\delta_{p_j,1}} \left(\frac{m}{\sin \theta_{\mathbf{k}_i}^+} \right)^{\delta_{p_i,1}} \left(\frac{\partial}{\partial \theta_{\mathbf{k}_i}^+} \right)^{1-\delta_{p_i,1}} \\ &+ b_{\ell} \left(\frac{m}{\sin \theta_{\mathbf{k}_j}^-} \right)^{\delta_{p_j,2}} \left(\frac{\partial}{\partial \theta_{\mathbf{k}_j}^-} \right)^{1-\delta_{p_j,2}} \left(\frac{m}{\sin \theta_{\mathbf{k}_i}^+} \right)^{\delta_{p_i,2}} \left(\frac{\partial}{\partial \theta_{\mathbf{k}_i}^+} \right)^{1-\delta_{p_i,2}} \left. \right] Y_{\ell}^m(\theta_{\mathbf{k}_j}^-, \varphi_j) Y_{\ell}^{m*}(\theta_{\mathbf{k}_i}^+, \varphi_i) \end{aligned} \quad (\text{C.3})$$

The summation over m can be evaluated using the addition theorems (B.29) for spherical harmonics. Then, the matrix elements of the reflection operator at the sphere in the plane-wave basis read

$$\langle \mathbf{k}_j, \text{TM}, - | \mathcal{R}_S | \mathbf{k}_i, \text{TM}, + \rangle = +2\pi \frac{c}{\xi \kappa_j} (AS_2 + BS_1), \quad (\text{C.4a})$$

$$\langle \mathbf{k}_j, \text{TE}, - | \mathcal{R}_S | \mathbf{k}_i, \text{TE}, + \rangle = +2\pi \frac{c}{\xi \kappa_j} (AS_1 + BS_2), \quad (\text{C.4b})$$

$$\langle \mathbf{k}_j, \text{TM}, - | \mathcal{R}_S | \mathbf{k}_i, \text{TE}, + \rangle = -2\pi \frac{c}{\xi \kappa_j} (CS_1 + DS_2), \quad (\text{C.4c})$$

$$\langle \mathbf{k}_j, \text{TE}, - | \mathcal{R}_S | \mathbf{k}_i, \text{TM}, + \rangle = +2\pi \frac{c}{\xi \kappa_j} (CS_2 + DS_1), \quad (\text{C.4d})$$

with A, B, C, D given by

$$A = \frac{\xi^4 \cos \varphi - c^4 (\kappa_i \kappa_j + k_i k_j \cos \varphi) (k_i k_j + \kappa_i \kappa_j \cos \varphi)}{\xi^4 - c^4 (\kappa_i \kappa_j + k_i k_j \cos \varphi)^2}, \quad (\text{C.5a})$$

$$B = -\frac{\xi^2 c^2 k_i k_j \sin^2 \varphi}{\xi^4 - c^4 (\kappa_i \kappa_j + k_i k_j \cos \varphi)^2}, \quad (\text{C.5b})$$

$$C = +\xi \frac{c^3 \kappa_j k_i^2 + c^3 \kappa_i k_i k_j \cos \varphi}{\xi^4 - c^4 (\kappa_i \kappa_j + k_i k_j \cos \varphi)^2} \sin \varphi, \quad (\text{C.5c})$$

$$D = -\xi \frac{c^3 \kappa_i k_j^2 + c^3 \kappa_j k_i k_j \cos \varphi}{\xi^4 - c^4 (\kappa_i \kappa_j + k_i k_j \cos \varphi)^2} \sin \varphi. \quad (\text{C.5d})$$

The Mie scattering amplitudes S_1 and S_2 are defined in (3.13). The angle functions π_{ℓ} and τ_{ℓ} defined in (3.15) are evaluated at

$$z = -\frac{c^2}{\xi^2} (\kappa_1 \kappa_2 + k_1 k_2 \cos \varphi). \quad (\text{C.6})$$

For incident plane waves propagating in $-z$ -direction, the matrix elements read

$$\langle \mathbf{k}_j, \text{TM}, + | \mathcal{R}_S | \mathbf{k}_i, \text{TM}, - \rangle = \langle \mathbf{k}_j, \text{TM}, - | \mathcal{R}_S | \mathbf{k}_i, \text{TM}, + \rangle, \quad (\text{C.7a})$$

$$\langle \mathbf{k}_j, \text{TE}, + | \mathcal{R}_S | \mathbf{k}_i, \text{TE}, - \rangle = \langle \mathbf{k}_j, \text{TE}, - | \mathcal{R}_S | \mathbf{k}_i, \text{TE}, + \rangle, \quad (\text{C.7b})$$

$$\langle \mathbf{k}_j, \text{TM}, + | \mathcal{R}_S | \mathbf{k}_i, \text{TE}, - \rangle = - \langle \mathbf{k}_j, \text{TM}, - | \mathcal{R}_S | \mathbf{k}_i, \text{TE}, + \rangle, \quad (\text{C.7c})$$

$$\langle \mathbf{k}_j, \text{TE}, + | \mathcal{R}_S | \mathbf{k}_i, \text{TM}, - \rangle = - \langle \mathbf{k}_j, \text{TE}, - | \mathcal{R}_S | \mathbf{k}_i, \text{TM}, + \rangle. \quad (\text{C.7d})$$

Appendix D

Change of basis matrix elements

The matrix elements implementing the change from the plane-wave basis to the multipole basis and vice versa are given by Eqs. (A.29) and (A.38) in Ref. [115]

$$\langle \mathbf{k}, p, \pm | \ell, m, P, \text{out} \rangle = 2\pi \frac{i^{1-p}}{\sqrt{\ell(\ell+1)}} \frac{c}{\xi \kappa} \left(\frac{m}{\sin \theta_{\mathbf{k}}^{\pm}} \right)^{\delta_{pP}} \left(\frac{\partial}{\partial \theta_{\mathbf{k}}^{\pm}} \right)^{1-\delta_{pP}} Y_{\ell}^m(\theta_{\mathbf{k}}^{\pm}, \varphi), \quad (\text{D.1a})$$

$$\langle \ell, m, P, \text{reg} | \mathbf{k}, p, \pm \rangle = -4\pi \frac{i^{p-1}}{\sqrt{\ell(\ell+1)}} \left(\frac{m}{\sin \theta_{\mathbf{k}}^{\pm}} \right)^{\delta_{pP}} \left(\frac{\partial}{\partial \theta_{\mathbf{k}}^{\pm}} \right)^{1-\delta_{pP}} Y_{\ell}^m(\theta_{\mathbf{k}}^{\pm}, -\varphi). \quad (\text{D.1b})$$

Here, we associate $p = 1$ ($p = 2$) to TE (TM) and $P = 1$ ($P = 2$) to E (M). The label reg denotes regular modes, and out denotes outgoing waves.

Explicit expressions for the change from the plane-wave basis to the multipole basis at imaginary frequency are given by

$$\langle \mathbf{k}, \text{TE}, \pm | \ell, m, \text{M}, \text{out} \rangle = i \frac{c^2 k}{\xi^2 \kappa} \sqrt{2\pi} \frac{N_{\ell}^m e^{im\varphi}}{\sqrt{\ell(\ell+1)}} i^m P_{\ell}^{m'} \left(\pm \frac{c\kappa}{\xi} \right), \quad (\text{D.2a})$$

$$\langle \mathbf{k}, \text{TM}, \pm | \ell, m, \text{M}, \text{out} \rangle = \frac{m}{k\kappa} \sqrt{2\pi} \frac{N_{\ell}^m e^{im\varphi}}{\sqrt{\ell(\ell+1)}} i^m P_{\ell}^m \left(\pm \frac{c\kappa}{\xi} \right), \quad (\text{D.2b})$$

$$\langle \mathbf{k}, \text{TE}, \pm | \ell, m, \text{E}, \text{out} \rangle = i \langle \mathbf{k}, \text{TM}, \pm | \ell, m, \text{M} \rangle, \quad (\text{D.2c})$$

$$\langle \mathbf{k}, \text{TM}, \pm | \ell, m, \text{E}, \text{out} \rangle = -i \langle \mathbf{k}, \text{TE}, \pm | \ell, m, \text{M} \rangle, \quad (\text{D.2d})$$

and for the change from the multipole basis to the plane-wave basis by

$$\langle \ell, m, \text{M}, \text{reg} | \mathbf{k}, \text{TE}, \pm \rangle = -i \frac{ck}{\xi} \sqrt{2\pi} \frac{2N_{\ell}^m e^{-im\varphi}}{\sqrt{\ell(\ell+1)}} i^m P_{\ell}^{m'} \left(\pm \frac{c\kappa}{\xi} \right), \quad (\text{D.3a})$$

$$\langle \ell, m, \text{M}, \text{reg} | \mathbf{k}, \text{TM}, \pm \rangle = m \frac{\xi}{ck} \sqrt{2\pi} \frac{2N_{\ell}^m e^{-im\varphi}}{\sqrt{\ell(\ell+1)}} i^m P_{\ell}^m \left(\pm \frac{c\kappa}{\xi} \right), \quad (\text{D.3b})$$

$$\langle \ell, m, \text{E}, \text{reg} | \mathbf{k}, \text{TE}, \pm \rangle = -i \langle \ell, m, \text{M} | \mathbf{k}, \text{TM}, \pm \rangle, \quad (\text{D.3c})$$

$$\langle \ell, m, \text{E}, \text{reg} | \mathbf{k}, \text{TM}, \pm \rangle = i \langle \ell, m, \text{M} | \mathbf{k}, \text{TE}, \pm \rangle. \quad (\text{D.3d})$$

Here, we have used once more the phase convention described in appendix A.2 for the associated Legendre polynomials. The coefficients N_ℓ^m are defined in (A.2).

Bibliography

- [1] H. B. G. Casimir, "On the attraction between two perfectly conducting plates", Proc. K. Ned. Akad. Wet. **51** (1948).
- [2] V. A. Parsegian, *Van der Waals Forces – A Handbook for Biologists, Chemists, Engineers, and Physicists* (Cambridge University Press, 2006), ISBN 978-0-521839-068.
- [3] F. London, "Zur Theorie und Systematik der Molekularkräfte", Z. Phys. **63**, 245 (1930), DOI 10.1007/BF01421741.
- [4] E. J. W. Verwey, "Theory of the Stability of Lyophobic Colloids", J. Phys. Chem. **51**, 631 (1947), DOI 10.1021/j150453a001.
- [5] H. B. G. Casimir and D. Polder, "The Influence of Retardation on the London-van der Waals Forces", Phys. Rev. **73**, 360 (1948), DOI 10.1103/PhysRev.73.360.
- [6] H. B. G. Casimir, in *The Casimir Effect 50 Years Later*, edited by M. Bordag (World Scientific Pub Co Inc, 1999), pp. 3–9, ISBN 978-9-810238-209.
- [7] R. S. Decca, D. López, E. Fischbach, and D. E. Krause, "Measurement of the Casimir Force between Dissimilar Metals", Phys. Rev. Lett. **91**, 050402 (2003), DOI 10.1103/PhysRevLett.91.050402.
- [8] R. Onofrio, "Casimir forces and non-Newtonian gravitation", New J. Phys. **8**, 237 (2006), DOI 10.1088/1367-2630/8/10/237.
- [9] R. S. Decca, D. López, E. Fischbach, G. L. Klimchitskaya, D. E. Krause, and V. M. Mostepanenko, "Tests of new physics from precise measurements of the Casimir pressure between two gold-coated plates", Phys. Rev. D **75**, 077101 (2007), DOI 10.1103/PhysRevD.75.077101.
- [10] R. S. Decca, D. López, E. Fischbach, G. Klimchitskaya, D. Krause, and V. Mostepanenko, "Novel constraints on light elementary particles and extra-dimensional physics from the Casimir effect", Eur. Phys. J. C **51**, 963 (2007), DOI 10.1140/epjc/s10052-007-0346-z.
- [11] M. Masuda and M. Sasaki, "Limits on Nonstandard Forces in the Submicrometer Range", Phys. Rev. Lett. **102**, 171101 (2009), DOI 10.1103/PhysRevLett.102.171101.

- [12] E. Fischbach and C. Talmadge, "Six years of the fifth force", *Nature* **356**, 207 (1992), DOI 10.1038/356207a0.
- [13] I. Antoniadis, S. Baessler, M. Büchner, V. Fedorov, S. Hoedl, A. Lambrecht, V. Nesvizhevsky, G. Pignol, K. Protasov, S. Reynaud, et al., "Short-range fundamental forces", *C. R. Phys.* **12**, 755 (2011), DOI 10.1016/j.crhy.2011.05.004.
- [14] A. G. Riess, A. V. Filippenko, P. Challis, A. Clocchiatti, A. Diercks, P. M. Garnavich, R. L. Gilliland, C. J. Hogan, S. Jha, R. P. Kirshner, et al., "Observational Evidence from Supernovae for an Accelerating Universe and a Cosmological Constant", *Astron. J.* **116**, 1009 (1998), DOI 10.1086/300499.
- [15] S. Perlmutter, G. Aldering, G. Goldhaber, R. A. Knop, P. Nugent, P. G. Castro, S. Deustua, S. Fabbro, A. Goobar, D. E. Groom, et al., "Measurements of Ω and Λ from 42 High-Redshift Supernovae", *Astron. J.* **517**, 565 (1999), DOI 10.1086/307221.
- [16] J. Martin, "Everything you always wanted to know about the cosmological constant problem (but were afraid to ask)", *C. R. Phys.* **13**, 566 (2012), DOI 10.1016/j.crhy.2012.04.008.
- [17] H. B. Chan, V. A. Aksyuk, R. N. Kleiman, D. J. Bishop, and F. Capasso, "Quantum Mechanical Actuation of Microelectromechanical Systems by the Casimir Force", *Science* **291**, 1941 (2001), DOI 10.1126/science.1057984.
- [18] H. B. Chan, V. A. Aksyuk, R. N. Kleiman, D. J. Bishop, and F. Capasso, "Nonlinear Micromechanical Casimir Oscillator", *Phys. Rev. Lett.* **87**, 211801 (2001), DOI 10.1103/PhysRevLett.87.211801.
- [19] E. Buks and M. L. Roukes, "Stiction, adhesion energy, and the Casimir effect in micromechanical systems", *Phys. Rev. B* **63**, 033402 (2001), DOI 10.1103/PhysRevB.63.033402.
- [20] M. Bordag, G. L. Klimchitskaya, U. Mohideen, and V. M. Mostepanenko, *Advances in the Casimir Effect* (Oxford University Press, 2009), ISBN 978-0-199238-743, DOI 10.1093/acprof:oso/9780199238743.001.0001.
- [21] S. K. Lamoreaux, "Demonstration of the Casimir Force in the 0.6 to $6\mu\text{m}$ Range", *Phys. Rev. Lett.* **78**, 5 (1997), DOI 10.1103/PhysRevLett.78.5.
- [22] U. Mohideen and A. Roy, "Precision Measurement of the Casimir Force from 0.1 to $0.9\mu\text{m}$ ", *Phys. Rev. Lett.* **81**, 4549 (1998), DOI 10.1103/PhysRevLett.81.4549.
- [23] A. Lambrecht, P. A. Maia Neto, and S. Reynaud, "The Casimir effect within scattering theory", *New J. Phys.* **8**, 243 (2006), DOI 10.1088/1367-2630/8/10/243.

- [24] T. Emig, N. Graham, R. L. Jaffe, and M. Kardar, "Casimir Forces between Arbitrary Compact Objects", *Phys. Rev. Lett.* **99**, 170403 (2007), DOI 10.1103/PhysRevLett.99.170403.
- [25] S. J. Rahi, T. Emig, N. Graham, R. L. Jaffe, and M. Kardar, "Scattering theory approach to electrodynamic Casimir forces", *Phys. Rev. D* **80**, 085021 (2009), DOI 10.1103/PhysRevD.80.085021.
- [26] A. Canaguier-Durand, Ph.D. thesis, Université Pierre et Marie Curie (2011), URL <https://tel.archives-ouvertes.fr/tel-00805047>.
- [27] B. Derjaguin, "Untersuchungen über die Reibung und Adhäsion, IV", *Kolloid-Zeitschrift* **69**, 155 (1934), DOI 10.1007/BF01433225.
- [28] F. Impens, C. C. Ttira, and P. A. Maia Neto, "Non-additive dynamical Casimir atomic phases", *J. Phys. B* **46** (2013), DOI 10.1088/0953-4075/46/24/245503.
- [29] M. Hartmann, G.-L. Ingold, and P. A. Maia Neto, "Advancing numerics for the Casimir effect to experimentally relevant aspect ratios", *Phys. Scr.* **93**, 114003 (2018), DOI 10.1088/1402-4896/aae34e.
- [30] A. O. Sushkov, W. J. Kim, D. A. R. Dalvit, and S. K. Lamoreaux, "Observation of the thermal Casimir force", *Nat. Phys.* **7**, 230 (2011), DOI 10.1038/nphys1909.
- [31] D. Garcia-Sanchez, K. Y. Fong, H. Bhaskaran, S. Lamoreaux, and H. X. Tang, "Casimir Force and In Situ Surface Potential Measurements on Nanomembranes", *Phys. Rev. Lett.* **109**, 027202 (2012), DOI 10.1103/PhysRevLett.109.027202.
- [32] P. J. van Zwol, G. Palasantzas, and J. T. M. De Hosson, "Influence of random roughness on the Casimir force at small separations", *Phys. Rev. B* **77**, 075412 (2008), DOI 10.1103/PhysRevB.77.075412.
- [33] P. J. van Zwol, G. Palasantzas, M. van de Schootbrugge, and J. T. M. De Hosson, "Measurement of dispersive forces between evaporated metal surfaces in the range below 100nm", *Appl. Phys. Lett.* **92**, 054101 (2008), DOI 10.1063/1.2832664.
- [34] S. de Man, K. Heeck, R. J. Wijngaarden, and D. Iannuzzi, "Halving the Casimir force with Conductive Oxides", *Phys. Rev. Lett.* **103**, 040402 (2009), DOI 10.1103/PhysRevLett.103.040402.
- [35] J. L. Garrett, D. A. T. Somers, and J. N. Munday, "Measurement of the Casimir Force between Two Spheres", *Phys. Rev. Lett.* **120**, 040401 (2018), DOI 10.1103/PhysRevLett.120.040401.
- [36] J. N. Munday, F. Capasso, V. A. Parsegian, and S. M. Bezrukov, "Measurements of the Casimir-Lifshitz force in fluids: The effect of electrostatic forces and Debye screening", *Phys. Rev. A* **78**, 032109 (2008), DOI 10.1103/PhysRevA.78.032109.

- [37] J. N. Munday, F. Capasso, and V. A. Parsegian, "Measured long-range repulsive Casimir–Lifshitz forces", *Nature* **457**, 170 (2008), DOI 10.1038/nature07610.
- [38] D. E. Krause, R. S. Decca, D. López, and E. Fischbach, "Experimental Investigation of the Casimir Force beyond the Proximity-Force Approximation", *Phys. Rev. Lett.* **98**, 050403 (2007), DOI 10.1103/PhysRevLett.98.050403.
- [39] G. Bimonte, D. López, and R. S. Decca, "Isoelectronic determination of the thermal Casimir force", *Phys. Rev. B* **93**, 184434 (2016), DOI 10.1103/PhysRevB.93.184434.
- [40] A. A. Banishev, G. L. Klimchitskaya, V. M. Mostepanenko, and U. Mohideen, "Demonstration of the Casimir Force between Ferromagnetic Surfaces of a Ni-Coated Sphere and a Ni-Coated Plate", *Phys. Rev. Lett.* **110**, 137401 (2013), DOI 10.1103/PhysRevLett.110.137401.
- [41] G. Jourdan, A. Lambrecht, F. Comin, and J. Chevrier, "Quantitative non-contact dynamic Casimir force measurements", *EPL* **85**, 31001 (2009), DOI 10.1209/0295-5075/85/31001.
- [42] C.-C. Chang, A. A. Banishev, R. Castillo-Garza, G. L. Klimchitskaya, V. M. Mostepanenko, and U. Mohideen, "Gradient of the Casimir force between Au surfaces of a sphere and a plate measured using an atomic force microscope in a frequency-shift technique", *Phys. Rev. B* **85**, 165443 (2012), DOI 10.1103/PhysRevB.85.165443.
- [43] G. Torricelli, I. Pirozhenko, S. Thornton, A. Lambrecht, and C. Binns, "Casimir force between a metal and a semimetal", *EPL* **93**, 51001 (2011), DOI 10.1209/0295-5075/93/51001.
- [44] D. S. Ether jr., L. B. Pires, S. Umrath, D. Martinez, Y. Ayala, B. Pontes, G. R. de S. Araújo, S. Frases, G.-L. Ingold, F. S. S. Rosa, et al., "Probing the Casimir force with optical tweezers", *EPL* **112**, 44001 (2015), DOI 10.1209/0295-5075/112/44001.
- [45] G. L. Klimchitskaya, U. Mohideen, and V. M. Mostepanenko, "The Casimir force between real materials: Experiment and theory", *Rev. Mod. Phys.* **81**, 1827 (2009), DOI 10.1103/RevModPhys.81.1827.
- [46] G. L. Klimchitskaya, M. Bordag, E. Fischbach, D. E. Krause, and V. M. Mostepanenko, "Observation of the thermal Casimir force is open to question", *Int. J. Mod. Phys. Conf. Ser.* **3**, 515 (2011), DOI 10.1142/S2010194511001036.
- [47] M. Bordag, G. L. Klimchitskaya, and V. M. Mostepanenko, "Comment on "Casimir Force and In Situ Surface Potential Measurements on Nanomembranes"", *Phys. Rev. Lett.* **109**, 199701 (2012), DOI 10.1103/PhysRevLett.109.199701.
- [48] M. Bordag and V. Nikolaev, "First analytic correction beyond the proximity force approximation in the Casimir effect for the electromagnetic field in sphere-plane geometry", *Phys. Rev. D* **81**, 065011 (2010), DOI 10.1103/PhysRevD.81.065011.

- [49] L. P. Teo, M. Bordag, and V. Nikolaev, "Corrections beyond the proximity force approximation", *Phys. Rev. D* **84**, 125037 (2011), DOI 10.1103/PhysRevD.84.125037.
- [50] L. P. Teo, "Material dependence of Casimir interaction between a sphere and a plate: First analytic correction beyond proximity force approximation", *Phys. Rev. D* **88**, 045019 (2013), DOI 10.1103/PhysRevD.88.045019.
- [51] G. Bimonte and T. Emig, "Exact Results for Classical Casimir Interactions: Dirichlet and Drude Model in the Sphere-Sphere and Sphere-Plane Geometry", *Phys. Rev. Lett.* **109**, 160403 (2012), DOI 10.1103/PhysRevLett.109.160403.
- [52] G. Bimonte, "Classical Casimir interaction of a perfectly conducting sphere and plate", *Phys. Rev. D* **95**, 065004 (2017), DOI 10.1103/PhysRevD.95.065004.
- [53] C. D. Fosco, F. C. Lombardo, and F. D. Mazzitelli, "Derivative-expansion approach to the interaction between close surfaces", *Phys. Rev. A* **89**, 062120 (2014), DOI 10.1103/PhysRevA.89.062120.
- [54] M. Hartmann, G.-L. Ingold, and P. A. Maia Neto, "Plasma versus Drude Modeling of the Casimir Force: Beyond the Proximity Force Approximation", *Phys. Rev. Lett.* **119**, 043901 (2017), DOI 10.1103/PhysRevLett.119.043901.
- [55] J. D. Jackson, *Classical electrodynamics* (Wiley, New York, NY, 1999), 3rd ed., ISBN 978-0-47130-932-1.
- [56] C. Cohen-Tannoudji, J. Dupont-Roc, and G. Grynberg, *Photons and Atoms: Introduction to Quantum Electrodynamics* (Wiley, 1997), ISBN 978-0-47118-433-1.
- [57] P. W. Milonni, R. J. Cook, and M. E. Goggin, "Radiation pressure from the vacuum: Physical interpretation of the Casimir force", *Phys. Rev. A* **38**, 1621 (1988), DOI 10.1103/PhysRevA.38.1621.
- [58] M. Planck, "Über die Begründung des Gesetzes der schwarzen Strahlung", *Ann. Phys.* **342**, 642 (1912), DOI 10.1002/andp.19123420403.
- [59] D. Dalvit, P. Milonni, D. Roberts, and F. da Rosa, *Casimir Physics*, Lecture Notes in Physics (Springer Berlin Heidelberg, 2011), ISBN 978-3-64220-287-2, DOI 10.1007/978-3-642-20288-9.
- [60] C. Genet, A. Lambrecht, and S. Reynaud, in *18th IAP Colloquium on the Nature of Dark Energy: Observational and Theoretical Results on the Accelerating Universe Paris, France, July 1-5, 2002* (2002), quant-ph/0210173, URL <https://arxiv.org/abs/quant-ph/0210173>.
- [61] P. W. Milonni, in *The Quantum Vacuum*, edited by P. W. Milonni (Academic Press, San Diego, 1994), pp. 1–33, ISBN 978-0-08057-149-2.

- [62] A. Einstein and O. Stern, "Einige Argumente für die Annahme einer molekularen Agitation beim absoluten Nullpunkt", *Ann. Phys.* **40**, 551 (1913), DOI 10.1002/andp.200590041.
- [63] W. Pauli, "Nobel Lecture: Exclusion Principle and Quantum Mechanics", (1946), URL http://www.nobelprize.org/nobel_prizes/physics/laureates/1945/pauli-lecture.html.
- [64] F. Simon, "Behaviour of Condensed Helium near Absolute Zero", *Nature* **133**, 529 (1934), DOI 10.1038/133529a0.
- [65] J. S. Dugdale and F. E. Simon, "Thermodynamic properties and melting of solid helium", *Proc. Royal Soc. A* **218**, 291 (1953), DOI 10.1098/rspa.1953.0105.
- [66] R. S. Mulliken, "The Band Spectrum of Boron Monoxide", *Nature* **114**, 349 (1924), DOI 10.1038/114349a0.
- [67] W. E. Lamb and R. C. Retherford, "Fine Structure of the Hydrogen Atom by a Microwave Method", *Phys. Rev.* **72**, 241 (1947), DOI 10.1103/PhysRev.72.241.
- [68] R. L. Jaffe, "Casimir effect and the quantum vacuum", *Phys. Rev. D* **72**, 021301 (2005), DOI 10.1103/PhysRevD.72.021301.
- [69] E. G. Adelberger, J. H. Gundlach, B. R. Heckel, S. Hoedl, and S. Schlamminger, "Torsion balance experiments: A low-energy frontier of particle physics", *Prog. Part. Nucl. Phys.* **62**, 102 (2009), DOI 10.1016/j.pnpnp.2008.08.002.
- [70] C. Genet, A. Lambrecht, and S. Reynaud, "Casimir force and the quantum theory of lossy optical cavities", *Phys. Rev. A* **67**, 043811 (2003), DOI 10.1103/PhysRevA.67.043811.
- [71] M. N. Vesperinas, *Scattering And Diffraction In Physical Optics* (Wspc, 2006), 2nd ed., ISBN 978-9-81256-340-8.
- [72] A. Lambrecht and S. Reynaud, "Casimir force between metallic mirrors", *Eur. Phys. J. D* **8**, 309 (2000), DOI 10.1007/s100530050041.
- [73] M. Boström and B. E. Sernelius, "Thermal Effects on the Casimir Force in the 0.1–0.5 μm Range", *Phys. Rev. Lett.* **84**, 4757 (2000), DOI 10.1103/PhysRevLett.84.4757.
- [74] G.-L. Ingold, A. Lambrecht, and S. Reynaud, "Quantum dissipative Brownian motion and the Casimir effect", *Phys. Rev. E* **80**, 041113 (2009), DOI 10.1103/PhysRevE.80.041113.
- [75] J. S. Høye, I. Brevik, J. B. Aarseth, and K. A. Milton, "Does the transverse electric zero mode contribute to the Casimir effect for a metal?", *Phys. Rev. E* **67**, 056116 (2003), DOI 10.1103/PhysRevE.67.056116.

- [76] R. Guérout, A. Lambrecht, K. A. Milton, and S. Reynaud, "Derivation of the Lifshitz-Matsubara sum formula for the Casimir pressure between metallic plane mirrors", *Phys. Rev. E* **90**, 042125 (2014), DOI 10.1103/PhysRevE.90.042125.
- [77] K. A. Milton, "Feeling the heat", *Nat. Phys.* **7**, 190 (2011), DOI 10.1038/nphys1931.
- [78] I. Pirozhenko, A. Lambrecht, and V. B. Svetovoy, "Sample dependence of the Casimir force", *New J. Phys.* **8**, 238 (2006), DOI 10.1088/1367-2630/8/10/238.
- [79] E. D. Palik, *Handbook of Optical Constants of Solids*, Academic Press handbook series (Academic Press, 1998), ISBN 978-0-080533-780.
- [80] R. L. Olmon, B. Slovick, T. W. Johnson, D. Shelton, S.-H. Oh, G. D. Boreman, and M. B. Raschke, "Optical dielectric function of gold", *Phys. Rev. B* **86**, 235147 (2012), DOI 10.1103/PhysRevB.86.235147.
- [81] G. Brändli and A. J. Sievers, "Absolute Measurement of the Far-Infrared Surface Resistance of Pb", *Phys. Rev. B* **5**, 3550 (1972), DOI 10.1103/PhysRevB.5.3550.
- [82] W. S. M. Werner, K. Glantschnig, and C. Ambrosch-Draxl, "Optical Constants and Inelastic Electron-Scattering Data for 17 Elemental Metals", *J. Phys. Chem. Ref. Data* **38**, 1013 (2009), DOI 10.1063/1.3243762.
- [83] V. B. Svetovoy, P. J. van Zwol, G. Palasantzas, and J. T. M. De Hosson, "Optical properties of gold films and the Casimir force", *Phys. Rev. B* **77**, 035439 (2008), DOI 10.1103/PhysRevB.77.035439.
- [84] G. Bimonte, "Generalized Kramers-Kronig transform for Casimir effect computations", *Phys. Rev. A* **81**, 062501 (2010), DOI 10.1103/PhysRevA.81.062501.
- [85] G. Bimonte, "Making precise predictions of the Casimir force between metallic plates via a weighted Kramers-Kronig transform", *Phys. Rev. A* **83**, 042109 (2011), DOI 10.1103/PhysRevA.83.042109.
- [86] O. Shpak and G. Palasantzas, "Analysis of Casimir forces with window functions: Kramers-Kronig general approach for real measured dielectric data", *Phys. Rev. A* **84**, 044501 (2011), DOI 10.1103/PhysRevA.84.044501.
- [87] E. M. Lifshitz, "The Theory of Molecular Attractive Forces between Solids", *Sov. Phys. JETP* **29**, 73 (1956).
- [88] M. J. Sparnaay, "Measurements of attractive forces between flat plates", *Physica* **24**, 751 (1958), DOI 10.1016/S0031-8914(58)80090-7.
- [89] G. Bressi, G. Carugno, R. Onofrio, and G. Ruoso, "Measurement of the Casimir Force between Parallel Metallic Surfaces", *Phys. Rev. Lett.* **88**, 041804 (2002), DOI 10.1103/PhysRevLett.88.041804.

- [90] M. T. Jaekel and S. Reynaud, "Casimir force between partially transmitting mirrors", *J. Phys. I France* **1**, 1395 (1991), DOI 10.1051/jp1:1991216.
- [91] F. W. J. Olver, A. B. Olde Daalhuis, D. W. Lozier, B. I. Schneider, R. F. Boisvert, C. W. Clark, M. B. R., and B. V. Saunders, "NIST Digital Library of Mathematical Functions", (2017), release 1.0.16, URL <https://dlmf.nist.gov>.
- [92] R. Guérout, G.-L. Ingold, A. Lambrecht, and S. Reynaud, "Accounting for Dissipation in the Scattering Approach to the Casimir Energy", *Symmetry* **10** (2018), DOI 10.3390/sym10020037.
- [93] H.-J. Butt and M. Kappl, *Surface and Interfacial Forces* (Wiley-VCH Verlag GmbH & Co. KGaA, 2010), ISBN 978-3-52762-941-1, DOI 10.1002/9783527629411.
- [94] M. Borkovec, I. Szilagyi, I. Popa, M. Finessi, P. Sinha, P. Maroni, and G. Papastavrou, "Investigating forces between charged particles in the presence of oppositely charged polyelectrolytes with the multi-particle colloidal probe technique", *Adv. Colloid Interface Sci.* **179-182**, 85 (2012), interfaces, Wettability, Surface Forces and Applications: Special Issue in honour of the 65th Birthday of John Ralston, DOI 10.1016/j.cis.2012.06.005.
- [95] M. Elzbienciak-Wodka, M. N. Popescu, F. J. M. Ruiz-Cabello, G. Trefalt, P. Maroni, and M. Borkovec, "Measurements of dispersion forces between colloidal latex particles with the atomic force microscope and comparison with Lifshitz theory", *J. Chem. Phys.* **140**, 104906 (2014), DOI 10.1063/1.4867541.
- [96] J. Błocki, J. Randrup, W. J. Świątecki, and C. Tsang, "Proximity forces", *Ann. Phys. (N. Y.)* **105**, 427 (1977), DOI 10.1016/0003-4916(77)90249-4.
- [97] A. Bulgac, P. Magierski, and A. Wirzba, "Scalar Casimir effect between Dirichlet spheres or a plate and a sphere", *Phys. Rev. D* **73**, 025007 (2006), DOI 10.1103/PhysRevD.73.025007.
- [98] M. Bordag and V. Nikolaev, "Casimir force for a sphere in front of a plane beyond proximity force approximation", *J. Phys. A* **41**, 164002 (2008), DOI 10.1088/1751-8113/41/16/164002.
- [99] P. A. Maia Neto, A. Lambrecht, and S. Reynaud, "Casimir effect with rough metallic mirrors", *Phys. Rev. A* **72**, 012115 (2005), DOI 10.1103/PhysRevA.72.012115.
- [100] C. D. Fosco, F. C. Lombardo, and F. D. Mazzitelli, "Proximity force approximation for the Casimir energy as a derivative expansion", *Phys. Rev. D* **84**, 105031 (2011), DOI 10.1103/PhysRevD.84.105031.
- [101] G. Bimonte, T. Emig, R. L. Jaffe, and M. Kardar, "Casimir forces beyond the proximity approximation", *EPL* **97**, 50001 (2012), DOI 10.1209/0295-5075/97/50001.

- [102] G. Bimonte, T. Emig, and M. Kardar, "Material dependence of Casimir forces: Gradient expansion beyond proximity", *Appl. Phys. Lett.* **100**, 074110 (2012), DOI 10.1063/1.3686903.
- [103] H. M. Nussenzveig, "High-Frequency Scattering by a Transparent Sphere. I. Direct Reflection and Transmission", *J. Math. Phys.* **10**, 82 (1969), DOI 10.1063/1.1664764.
- [104] H. M. Nussenzveig, *Diffraction effects in semiclassical scattering* (Cambridge University Press, 1992), ISBN 978-0-511599-903, DOI 10.1017/CBO9780511599903.
- [105] M. Schaden and L. Spruch, "Infinity-free semiclassical evaluation of Casimir effects", *Phys. Rev. A* **58**, 935 (1998), DOI 10.1103/PhysRevA.58.935.
- [106] R. L. Jaffe and A. Scardicchio, "Casimir Effect and Geometric Optics", *Phys. Rev. Lett.* **92**, 070402 (2004), DOI 10.1103/PhysRevLett.92.070402.
- [107] A. Scardicchio and R. L. Jaffe, "Casimir effects: an optical approach I. Foundations and examples", *Nucl. Phys. B* **704**, 552 (2005), DOI 10.1016/j.nuclphysb.2004.10.017.
- [108] B. Spreng, M. Hartmann, V. Henning, P. A. Maia Neto, and G.-L. Ingold, "Proximity force approximation and specular reflection: Application of the WKB limit of Mie scattering to the Casimir effect", *Phys. Rev. A* **97**, 062504 (2018), DOI 10.1103/PhysRevA.97.062504.
- [109] B. M. Axilrod and E. Teller, "Interaction of the van der Waals Type Between Three Atoms", *J. Chem. Phys.* **11**, 299 (1943), DOI 10.1063/1.1723844.
- [110] F. Bornemann, "On the numerical evaluation of Fredholm determinants", *Math. Comp.* **79**, 871 (2010), DOI 10.1090/S0025-5718-09-02280-7.
- [111] C. Bohren and D. R. Huffman, *Absorption and Scattering of Light by Small Particles* (Wiley Science Paperback Series, 2007), ISBN 978-0-471293-408, DOI 10.1002/9783527618156.
- [112] H. M. Nussenzveig, "High-frequency scattering by an impenetrable sphere", *Ann. Phys. (N. Y.)* **34**, 23 (1965), DOI 10.1016/0003-4916(65)90041-2.
- [113] P. Davis, *Circulant matrices* (Wiley, 1979), ISBN 978-0-471057-710.
- [114] W. J. Kim, A. O. Sushkov, D. A. R. Dalvit, and S. K. Lamoreaux, "Surface contact potential patches and Casimir force measurements", *Phys. Rev. A* **81**, 022505 (2010), DOI 10.1103/PhysRevA.81.022505.
- [115] R. Messina, P. A. Maia Neto, B. Guizal, and M. Antezza, "Casimir interaction between a sphere and a grating", *Phys. Rev. A* **92**, 062504 (2015), DOI 10.1103/PhysRevA.92.062504.

- [116] A. Canaguier-Durand, P. A. Maia Neto, A. Lambrecht, and S. Reynaud, "Thermal Casimir effect for Drude metals in the plane-sphere geometry", *Phys. Rev. A* **82**, 012511 (2010), DOI 10.1103/PhysRevA.82.012511.
- [117] A. Canaguier-Durand, P. A. Maia Neto, A. Lambrecht, and S. Reynaud, "Erratum: Thermal Casimir effect for Drude metals in the plane-sphere geometry [Phys. Rev. A 82, 012511 (2010)]", *Phys. Rev. A* **83**, 039905 (2011), DOI 10.1103/PhysRevA.83.039905.
- [118] IEEE Standards Association, "IEEE Standard for Floating-Point Arithmetic", IEEE Std 754-2008 pp. 1–70 (2008), DOI 10.1109/IEEESTD.2008.4610935.
- [119] A. Canaguier-Durand, P. A. Maia Neto, I. Cavero-Pelaez, A. Lambrecht, and S. Reynaud, "Casimir Interaction between Plane and Spherical Metallic Surfaces", *Phys. Rev. Lett.* **102**, 230404 (2009), DOI 10.1103/PhysRevLett.102.230404.
- [120] A. Canaguier-Durand, P. A. Maia Neto, A. Lambrecht, and S. Reynaud, "Thermal Casimir Effect in the Plane-Sphere Geometry", *Phys. Rev. Lett.* **104**, 040403 (2010), DOI 10.1103/PhysRevLett.104.040403.
- [121] A. Canaguier-Durand, A. Gérardin, R. Guérout, P. A. Maia Neto, V. V. Nesvizhevsky, A. Y. Voronin, A. Lambrecht, and S. Reynaud, "Casimir interaction between a dielectric nanosphere and a metallic plane", *Phys. Rev. A* **83**, 032508 (2011), DOI 10.1103/PhysRevA.83.032508.
- [122] A. Canaguier-Durand, G.-L. Ingold, M.-T. Jaekel, A. Lambrecht, P. A. Maia Neto, and S. Reynaud, "Classical Casimir interaction in the plane-sphere geometry", *Phys. Rev. A* **85**, 052501 (2012), DOI 10.1103/PhysRevA.85.052501.
- [123] A. Canaguier-Durand, R. Guérout, P. A. Maia Neto, A. Lambrecht, and S. Reynaud, "The Casimir effect in the sphere-plane geometry", *Int. J. Mod. Phys. Conf. Ser.* **14**, 250 (2012), DOI 10.1142/S2010194512007374.
- [124] M. Dailey, F. M. Dopico, and Q. Ye, "Relative Perturbation Theory for Diagonally Dominant Matrices", *SIAM J. Matrix Anal. Appl.* **35**, 1303 (2014), DOI 10.1137/130943613.
- [125] S. Ambikasaran and E. Darve, "An $\mathcal{O}(N \log N)$ Fast Direct Solver for Partial Hierarchically Semi-Separable Matrices", *J. Sci. Comput.* **57**, 477 (2013), DOI 10.1007/s10915-013-9714-z.
- [126] A. Aminfar, S. Ambikasaran, and E. Darve, "A fast block low-rank dense solver with applications to finite-element matrices", *J. Comput. Phys.* **304**, 170 (2016), DOI 10.1016/j.jcp.2015.10.012.

- [127] S. Ambikasaran, D. Foreman-Mackey, L. Greengard, D. W. Hogg, and M. O’Neil, “Fast Direct Methods for Gaussian Processes”, *IEEE Trans. Pattern Anal. Mach. Intell.* **38**, 252 (2016), DOI 10.1109/TPAMI.2015.2448083.
- [128] S. Ambikasaran, M. O’Neil, and K. R. Singh, “Fast symmetric factorization of hierarchical matrices with applications”, *ArXiv e-prints* (2016), 1405.0223, URL <https://arxiv.org/abs/1405.0223>.
- [129] C. Eckart and G. Young, “The approximation of one matrix by another of lower rank”, *Psychometrika* **1**, 211 (1936), DOI 10.1007/BF02288367.
- [130] S. Ambikasaran, “A fast direct solver for dense linear systems”, (2013), version 3.14, URL <https://github.com/sivaramambikasaran/HODLR>.
- [131] E. Anderson, Z. Bai, C. Bischof, S. Blackford, J. Demmel, J. Dongarra, J. Du Croz, A. Greenbaum, S. Hammarling, A. McKenney, et al., *LAPACK Users’ Guide* (Society for Industrial and Applied Mathematics, Philadelphia, PA, 1999), 3rd ed., ISBN 0-89871-447-8, DOI 10.1137/1.9780898719604.
- [132] R. C. Whaley and A. Petitet, “Minimizing development and maintenance costs in supporting persistently optimized BLAS”, *Softw. Pract. Exp.* **35**, 101 (2005), DOI 10.1002/spe.626.
- [133] ATLAS developer team, “Automatically Tuned Linear Algebra Software (ATLAS)”, (2016), version 3.10.3, URL <http://math-atlas.sourceforge.net>.
- [134] R. Morris, “The Dilogarithm Function of a Real Argument”, *Math. Comput.* **33**, 778 (1979), DOI 10.2307/2006312.
- [135] S. L. Moshier, “Cephes Math Library Release 2.8”, (2000), URL <http://www.netlib.org/cephes>.
- [136] W. H. Press, B. P. Flannery, S. A. Teukolsky, and W. T. Vetterling, *Numerical Recipes in C: The Art of Scientific Computing, Second Edition* (Cambridge University Press, 1992), ISBN 978-0-521431-088.
- [137] I. Bogaert, B. Michiels, and J. Fostier, “ $\mathcal{O}(1)$ Computation of Legendre Polynomials and Gauss–Legendre Nodes and Weights for Parallel Computing”, *SIAM J. Sci. Comput.* **34**, C83 (2012), DOI 10.1137/110855442.
- [138] S. Zhang and J. Jin, *Computation of Special Functions* (Wiley-Interscience, 1996), ISBN 978-0-471119-630.
- [139] H. Skovgaard, “On Inequalities of the Turán Type”, *Math. Scand.* **2**, 65 (1954), DOI 10.7146/math.scand.a-10396.
- [140] Y.-I. Xi, “Fast evaluation of Gaunt coefficients: recursive approach”, *J. Comput. Appl. Math.* **85**, 53 (1997), DOI 10.1016/S0377-0427(97)00128-3.

- [141] H. S. Cohl and H. Volkmer, "Definite Integrals using Orthogonality and Integral Transforms", *SIGMA* **8** (2012), DOI 10.3842/SIGMA.2012.077.
- [142] E. G. Muenz, T. Manoel, and M. Hartmann, "A C port of the QUADPACK software for solving integrals", (2013), URL <https://github.com/ESSS/cquadpack>.
- [143] R. Piessens, E. Doncker-Kapenga, C. W. Überhuber, and D. Kahaner, *Quadpack: A Subroutine Package for Automatic Integration* (Springer-Verlag, 1983), ISBN 978-0-387125-534, DOI 10.1007/978-3-642-61786-7.
- [144] I. S. Gradshteyn and I. M. Ryzhik, *Table of integrals, series, and products* (Elsevier/Academic Press, Amsterdam, 2007), 7th ed., ISBN 978-0-123736-376.
- [145] S. Ambikasaran and K. R. Singh, "HODLR: Fast direct solver, symmetric factorization and determinant computation for dense linear systems", (2016), version 3.141, URL <https://gitlab.com/SAFRAN/HODLR>.
- [146] B. Fornberg, "Generation of Finite Difference Formulas on Arbitrarily Spaced Grids", *Math. Comp.* **51**, 699 (1988), DOI 10.1090/S0025-5718-1988-0935077-0.
- [147] Wolfram Research, Inc., "Mathematica", (2017), version 11.1.
- [148] R. Zandi, T. Emig, and U. Mohideen, "Quantum and thermal Casimir interaction between a sphere and a plate: Comparison of Drude and plasma models", *Phys. Rev. B* **81**, 195423 (2010), DOI 10.1103/PhysRevB.81.195423.
- [149] G. Bimonte, "Going beyond PFA: A precise formula for the sphere-plate Casimir force", *EPL* **118**, 20002 (2017), DOI 10.1209/0295-5075/118/20002.
- [150] F. Johansson et al., *mpmath: a Python library for arbitrary-precision floating-point arithmetic* (2013), version 0.18, URL <http://mpmath.org>.
- [151] J. S. Høye, I. Brevik, S. A. Ellingsen, and J. B. Aarseth, "Analytical and numerical verification of the Nernst theorem for metals", *Phys. Rev. E* **75**, 051127 (2007), DOI 10.1103/PhysRevE.75.051127.
- [152] G. L. Klimchitskaya and V. M. Mostepanenko, "Comment on "Analytical and numerical verification of the Nernst theorem for metals"", *Phys. Rev. E* **77**, 023101 (2008), DOI 10.1103/PhysRevE.77.023101.
- [153] C. D. Fosco, F. C. Lombardo, and F. D. Mazzitelli, "Derivative expansion for the electromagnetic Casimir free energy at high temperatures", *Phys. Rev. D* **92**, 125007 (2015), DOI 10.1103/PhysRevD.92.125007.
- [154] S. Umrath, M. Hartmann, G.-L. Ingold, and P. A. Maia Neto, "Disentangling geometric and dissipative origins of negative Casimir entropies", *Phys. Rev. E* **92**, 042125 (2015), DOI 10.1103/PhysRevE.92.042125.

- [155] V. B. Bezerra, G. L. Klimchitskaya, and V. M. Mostepanenko, “Thermodynamical aspects of the Casimir force between real metals at nonzero temperature”, *Phys. Rev. A* **65**, 052113 (2002), DOI 10.1103/PhysRevA.65.052113.
- [156] V. B. Bezerra, G. L. Klimchitskaya, and V. M. Mostepanenko, “Correlation of energy and free energy for the thermal Casimir force between real metals”, *Phys. Rev. A* **66**, 062112 (2002), DOI 10.1103/PhysRevA.66.062112.
- [157] V. B. Bezerra, G. L. Klimchitskaya, V. M. Mostepanenko, and C. Romero, “Violation of the Nernst heat theorem in the theory of the thermal Casimir force between Drude metals”, *Phys. Rev. A* **69**, 022119 (2004), DOI 10.1103/PhysRevA.69.022119.
- [158] G.-L. Ingold, S. Umrath, M. Hartmann, R. Guérout, A. Lambrecht, S. Reynaud, and K. A. Milton, “Geometric origin of negative Casimir entropies: A scattering-channel analysis”, *Phys. Rev. E* **91**, 033203 (2015), DOI 10.1103/PhysRevE.91.033203.
- [159] P. Rodriguez-Lopez, “Casimir energy and entropy in the sphere-sphere geometry”, *Phys. Rev. B* **84**, 075431 (2011), DOI 10.1103/PhysRevB.84.075431.
- [160] M. Boström and B. E. Sernelius, “Entropy of the Casimir effect between real metal plates”, *Physica A* **339**, 53 (2004), DOI 10.1016/j.physa.2004.03.037.
- [161] M. Bordag, “Drude model and Lifshitz formula”, *Eur. Phys. J. C* **71**, 1788 (2011), DOI 10.1140/epjc/s10052-011-1788-x.
- [162] G. Bimonte, “Beyond-proximity-force-approximation Casimir force between two spheres at finite temperature”, *Phys. Rev. D* **97**, 085011 (2018), DOI 10.1103/PhysRevD.97.085011.
- [163] R. Decca, D. López, E. Fischbach, G. L. Klimchitskaya, D. E. Krause, and V. M. Mostepanenko, “Precise comparison of theory and new experiment for the Casimir force leads to stronger constraints on thermal quantum effects and long-range interactions”, *Ann. Phys. (N. Y.)* **318**, 37 (2005), special Issue, DOI 10.1016/j.aop.2005.03.007.
- [164] G. Bimonte, T. Emig, M. Kardar, and M. Krüger, “Nonequilibrium Fluctuational Quantum Electrodynamics: Heat Radiation, Heat Transfer, and Force”, *Annu. Rev. Condens. Matter Phys.* **8**, 119 (2017), DOI 10.1146/annurev-conmatphys-031016-025203.
- [165] A. A. Banishev, C.-C. Chang, G. L. Klimchitskaya, V. M. Mostepanenko, and U. Mohideen, “Measurement of the gradient of the Casimir force between a nonmagnetic gold sphere and a magnetic nickel plate”, *Phys. Rev. B* **85**, 195422 (2012), DOI 10.1103/PhysRevB.85.195422.
- [166] E. K. Ifantis and P. D. Siafarikas, “Bounds for modified Bessel functions”, *Rend. Circ. Mat. Palermo Ser. 2* **40**, 347 (1991), DOI 10.1007/BF02845073.

- [167] D. E. Winch and P. H. Roberts, "Derivatives of addition theorems for Legendre functions", *J. Austral. Math. Soc.* **37**, 212 (1995), DOI 10.1017/S0334270000007670.
- [168] M. Hartmann, D. Poletti, M. Ivanchenko, S. Denisov, and P. Hänggi, "Asymptotic Floquet states of open quantum systems: the role of interaction", *New J. Phys.* **19**, 083011 (2017), DOI 10.1088/1367-2630/aa7ceb.
- [169] V. Volokitin, A. Liniov, I. Meyerov, M. Hartmann, M. Ivanchenko, P. Hänggi, and S. Denisov, "Computation of the asymptotic states of modulated open quantum systems with a numerically exact realization of the quantum trajectory method", *Phys. Rev. E* **96**, 053313 (2017), DOI 10.1103/PhysRevE.96.053313.

List of Symbols

Physical constants

c	speed of light in vacuum	299 792 458 m/s
\hbar	reduced Planck constant	$1.054571800 \times 10^{-34}$ Js = $6.582119514 \times 10^{-16}$ eVs/rad
k_B	Boltzmann constant	$1.38064852 \times 10^{-23}$ J/K
ϵ_0	vacuum permittivity	$(\mu_0 c^2)^{-1} = 8.854187817620 \times 10^{-12}$ F/m
μ_0	vacuum permeability	$4\pi \times 10^{-7}$ H/m = $1.25663706 \times 10^{-6}$ H/m

Special functions

$I_\nu(x)$	modified Bessel function of the first kind [91, §10.25]
$K_\nu(x)$	modified Bessel function of the second kind [91, §10.25]
$\text{Li}_s(x)$	polylogarithm of order s [91, §25.12]
$P_\ell(x)$	ordinary Legendre polynomial, see appendix A.2
$P_\ell^m(x)$	associated Legendre polynomial, see appendix A.2
$Y_\ell^m(\theta, \varphi)$	spherical harmonics, see appendix A.1
$\Gamma(z)$	Gamma function, $\Gamma(n) = (n - 1)!$ [91, §5.2]
$\zeta(s)$	Riemann zeta function [91, §25.2]

Calligraphic symbols

\mathcal{F}	Casimir free energy, see section 2.8
\mathcal{L}	center-to-plate separation in the plane-sphere geometry, $\mathcal{L} = L + R$, cf. Fig 3.1
\mathcal{M}	round-trip operator, see section 2.8
$\widehat{\mathcal{M}}$	symmetrized round-trip operator in the plane-sphere geometry, see section 4.2
\mathcal{R}_P	reflection operator at the plane, see section 2.4
\mathcal{R}_S	reflection operator at the sphere, see sections 3.3 and 4.1
\mathcal{T}	translation operator, see section 2.3

Greek symbols

γ	relaxation frequency in the Drude model, see section 2.5
$\epsilon(\omega)$	dielectric function, see sections 2.5 and 2.6
$\hat{\epsilon}_p$	polarization vector in the plane-wave basis, see section 2.2
η	accuracy due to the truncation of the vector space, see section 5.5
κ	$\kappa = (\xi^2/c^2 + k^2)^{1/2}$, see section 2.2
$\Lambda_{\ell_1 \ell_2}^m$	normalization coefficient, see (4.18)
λ_P	plasma wavelength, $\lambda_P = 2\pi c/\omega_P$
λ_T	thermal wavelength, $\lambda_T = \hbar c/(k_B T)$
ξ	imaginary frequency
ξ_n	n th Matsubara frequency, $\xi_n = 2\pi n k_B T/\hbar$
π_ℓ, τ_ℓ	angular functions, see section 3.3
ϕ	direction of propagation in the z -direction, see section 2.2
ω	(angular) frequency
ω_P	plasma frequency, see section 2.5

Latin symbols

a_ℓ, b_ℓ	Mie coefficients, see sections 3.3 and 4.1
E	Casimir energy, $E = \mathcal{F}(T = 0)$
F, F'	Casimir force, $F = -\partial\mathcal{F}/\partial L$, and force gradient, $F' = -\partial^2\mathcal{F}/\partial L^2$
\mathbf{K}	wave vector, $\mathbf{K} = (K_x, K_y, K_z)$
K	length of the wave vector \mathbf{K} , $K = \mathbf{K} $
\mathbf{k}	projection of the wave vector \mathbf{K} onto x - y plane, $\mathbf{k} = (K_x, K_y, 0)$
k	length of vector \mathbf{k} , $k = \mathbf{k} $
k_z	modulus of the wave vector's z -component, $k_z = K_z $
L	separation between plane and sphere, cf. Fig 3.1
ℓ	azimuthal quantum number, see section 4.1
E, M	electric and magnetic multipole waves, see section 4.1
m	magnetic quantum number, see section 4.1
N_ℓ^m	normalization coefficient for spherical harmonics, see (A.2)
P	polarization in the multipole basis, see section 4.1
p	polarization in the plane-wave basis, see section 2.2
R	radius of the sphere, cf. Fig 3.1
r_p	Fresnel coefficient, see section 2.4
S_1, S_2	Mie scattering amplitude, see (3.13)
T	temperature
TE, TM	transverse electric and transverse magnetic polarization, see section 2.2

List of publications

Casimir effect

- [158] G.-L. Ingold, S. Umrath, M. Hartmann, R. Gu erout, A. Lambrecht, S. Reynaud, K. A. Milton, "Geometric origin of negative Casimir entropies: A scattering-channel analysis", *Phys. Rev. E* **91**, 033203 (2015)
- [154] S. Umrath, M. Hartmann, G.-L. Ingold, P. A. Maia Neto, "Disentangling geometric and dissipative origins of negative Casimir entropies", *Phys. Rev. E* **92**, 042125 (2015)
- [54] M. Hartmann, G.-L. Ingold, P. A. Maia Neto "Plasma vs Drude modelling of the Casimir force: Beyond the proximity force approximation", *Phys. Rev. Lett.* **119**, 043901 (2017)
- [108] B. Spreng, M. Hartmann, V. Henning, P. A. Maia Neto, G.-L. Ingold, "Proximity force approximation and specular reflection: Application of the WKB limit of Mie scattering to the Casimir effect", *Phys. Rev. A* **97**, 062504 (2018)
- [29] M. Hartmann, G.-L. Ingold, P. A. Maia Neto, "Advancing numerics for the Casimir effect to experimentally relevant aspect ratios", *Phys. Scr.* **93**, 114003 (2018)

Open Quantum Systems

- [168] M. Hartmann, D. Poletti, M. Ivanchenko, S. Denisov, P. H anggi, "Asymptotic Floquet states of open quantum systems: a role of interaction", *New J. Phys.* **19**, 083011 (2017)
- [169] V. Volokitin, A. Linirov, I. Meyerov, M. Hartmann, M. Ivanchenko, P. H anggi, S. Denisov, "Computation of the asymptotic states of modulated open quantum systems with a numerically exact realization of the quantum trajectory method", *Phys. Rev. E* **96**, 053313 (2017)

Acknowledgements

First of all, I would like to express my gratitude to Peter Hänggi with whom I originally started my Ph.D. Without his understanding and support, I would have not been able to write this thesis.

I want to thank my advisor Gert-Ludwig Ingold for his excellent supervision and his constant support. I learned and profited a lot from our discussions, his suggestions, and his experience. Also, I am very grateful that he made it possible for me to go to Rio de Janeiro – even at a time when I haven't even been his PhD student. My visits were crucial for this thesis, for example, the idea of the symmetrization of the round-trip operator was born during my first stay in Rio.

I also want to thank Paulo Maia Neto. Our discussions, his knowledge and expertise in semiclassicals and Casimir physics were of much help to me. Also, I want to thank him for making my trips to Rio so enjoyable. Thanks to him, I visited the opera in Rio, watched the paralympics, and had dinner at some excellent restaurants. In addition, I want to thank him and his wife very much for their help and support after I got mugged.

I'd like to mention the Ph.D. students of our small Casimir group, namely Benjamin Spreng, Vinicius Henning, and at the beginning Stefan Umrath. I have enjoyed working with them very much and learned a lot during our discussions. In addition, I want to thank Benjamin Spreng for his careful proofreading of my thesis.

I want to thank Ricardo Decca. I have learned a lot about Casimir experiments during our discussions. Also, I want to thank him for sharing his experimental data that allowed me to compare my numerical results with Casimir measurements.

For the numerical computations, I heavily used our local computer cluster. I want to thank Ralf Utermann for all the work he spends maintaining the cluster, and his help when I had questions or one of my jobs needed a bit more time than expected.

For the pleasant work environment, the coffee breaks, and all the fun I had during our "coffee seminars"¹, I want to thank Sebastian Tölle, Patrick Seiler, Andreas Prinz-Zwick, and Christian Schiegg.

¹<https://kaffeeseminar.speicherleck.de>

I want to thank Jörg Lehmann for advice, motivation, and his help with PyX², which has been used to create all figures in this thesis.

Last, but not least, I want to thank my girlfriend Kuhu and my parents for their constant support.

²<https://pyx-project.org/>